Tailoring Magnetic Properties of Co-Fe Thin Films by Topographical Modifications Using Thermal Annealing and Swift Heavy Ion Irradiation and Fabrication of Magnetoelectric Multilayers for Device Applications

Thesis submitted to
Cochin University of Science and Technology
in partial fulfilment of the requirements for the award of the degree of

Doctor of Philosophy

Geetha P

Department of Physics
Cochin University of Science and Technology
Cochin- 682022
India

October 2014

Tailoring Magnetic Properties of Co-Fe Thin Films by Topographical Modifications Using Thermal Annealing and Swift Heavy Ion Irradiation and Fabrication of Magnetoelectric Multilayers for Device Applications

Ph.D Thesis

Author:

Geetha P
Pookat House
Mangottuvayal Road
P.O.Kottooli
Kozhikode- 673016
Kerala. India
E-Mail: geethapookat@gmail.com

Supervising Guide:

Prof. (Dr.) M. R. Anantharaman
Professor, Department of Physics
Cochin University of Science and Technology
Cochin - 682 022
Kerala. India.

October 2014

Cover page illustration:

Front: MFM images of as prepared and irradiated (fluence $1x10^{11}$ions/cm^2) amorphous CoFe thin films

Back: TEM image of BTO-CoFe-BTO multilayer (Top view)

Department of Physics
Cochin University of Science and Technology
Cochin – 682022

Certificate

Certified that the present Ph.D. thesis work entitled **"Tailoring Magnetic Properties of Co-Fe Thin Films by Topographical Modifications Using Thermal Annealing and Swift Heavy Ion Irradiation and Fabrication of Magnetoelectric Multilayers for Device Applications"**, submitted by **Mrs. Geetha P** is an authentic record of research work carried out by her under my supervision in the Department of Physics in partial fulfillment of the requirements for the Degree of Doctor of Philosophy of Cochin University of Science and Technology, and has not been included in any other thesis submitted previously for the award of any degree.

.

October 2014

Cochin -22

Prof. M. R. Anantharaman

Supervising Guide
Department of Physics
CUSAT

DECLARATION

I hereby declare that the Ph.D. thesis work entitled, **"Tailoring Magnetic Properties of Co-Fe Thin Films by Topographical Modifications Using Thermal Annealing and Swift Heavy Ion Irradiation and Fabrication of Magnetoelectric Multilayers for Device Applications"** is based on the original work carried out by me under the guidance of **Prof. M R Anantharaman,** in the Department of Physics, Cochin University of Science and Technology, Cochin-22 and has not been included in any other thesis submitted previously for the award of any degree.

Geetha P

Cochin – 22
October 2014

Department of Physics
Cochin University of Science and Technology
Cochin – 682022

Certificate

Certified that all the relevant corrections and modifications suggested by the audience during the Pre-synopsis seminar and recommended by the Doctoral Committee of the candidate has been incorporated in the thesis.

Cochin -22
October 2014

Prof. M. R. Anantharaman

Supervising Guide
Department of Physics
CUSAT

The whole of science is nothing more than a refinement of everyday thinking

– Albert Einstein

Dedicated to my Parents and Brother.....

Acknowledgement

It is with immense pleasure and a sense of satisfaction that I note down the following few words of gratitude, that spring up from the bottom of my heart, to all those associated with my research career. Of them of course, the first and the foremost is none other than Prof. Dr. M.R Anantharaman, my philosopher and guide. A giant by intelligence, an authority on his subject, he stands out with international acclaim among his class. Naturally, as with any busy body he has too much demand on his time. Despite all that and other preoccupations he managed to find time to help me and of course others as well, with his invaluable suggestions, guidance and support throughout my tenure as his research student. I am sure that but for his sincere efforts, care and contribution perhaps this would not have been a reality, for which I am highly indebted to him and his family. The path to success shown by him should be a guiding force throughout my life ahead and in all my future endeavours.

Further my sincere thanks are due to Prof. Ramesh Babu Thayyullathil for his valuable contribution, direction, guidance and assistance in my Doctoral studies, which of course was a true trigger of motivation too. I am also thankful in no less measure to Prof. B Pradeep, Head of Department of Physics, Cochin University of Science and Technology, who rendered all the help and assistance, I was in need of. I really cherished memories of my close association with them. Let me also express my heart full thanks to other teachers and the members on the staff of the department, the labs and so on. I also recollect with thanks and gratitude the help and cooperation extended to me by the teaching and non-teaching staff of the department of physics and administrative staffs of Cochin university.

I will be failing in my duty if I don't, in this context express my thankfulness for the help and support received from the different research institutes in India and abroad. My sincere thanks are due to Dr. Swapna S Nair, Asst. Professor,

Department of Physics, Central University of Kerala, who counts among my best friends for helping me by giving me necessary assistance, advice and guidance in this regard. I cherished her loving care and encouragement which I must say was like providential. I carry the memories thereof with me.

Also I recollect with a sense of gratification the following eminent scientists for extending their help for carrying out different measurements and scrutinising and vetting my papers and putting them up in journals, thus being instrumental in my success. Of them Dr. D Sakthikumar (Bio Nano Electronics Research Centre, Toyo University Japan), Dr. Raju V Ramanujan (School of Materials Science and Engineering, Nanyang Technological University, Singapore), Dr. Salim Al-Harthi and Dr. Imad Al-Omari (Sultan Qaboos University, Muscat), Dr. V Ganesan, (IUC, Indore, India) merit special mention.

Further I am again thankful to Dr. D. K. Avasthi of IUAC, New Delhi for making available to me the laboratory facilities for swift heavy ion irradiation required by me. In addition, the technical assistance and services rendered by research scholars and engineers around there also to be appreciated.

The financial support provided by the UGC, which merits special mention, was of great help and actually a boon to me for which I should be grateful to Dr. Radhakrishan, former Director of International School of Photonics, who assisted me in a big way to get it sanctioned to me in time.

Talking about my teachers or my preceptors, I am reminded of my childhood days when I was initiated into learning and when I started my schooling. It gives me a nostalgic kind of experience especially when my memories of my teachers, to whom I am very much obliged, flash through my mind. Of course they were to a large extent responsible for moulding my career. No words would suffice to give

expression to my indebtedness to them, especially to Kumudabhai teacher, Sundereswari teacher and Vijayan sir.

A true friend never fails you. I was fortunate enough to have had very sincere and helpful friends among my colleagues, teachers and hostel mates etc. to mention a few names they are Anila, Anisha, Bhavya, Poornima, Varsha, Mangala, Sinichechi, Premitha, Jabir, Midu, Shobin, Deepak, Reethamma mam.... They were quite helpful, lovable and affectionate. Their suggestions, encouragements and support always took me to good stead. I am largely thankful to them. The memories of the good times spend with them will never fade away but will stay on green in my mind. To muse on those sweet memories will definitely have a toning up effect in testing times; I am sure.

It is worthwhile enough to mention here all the help, assistance, care and love extended to me by my senior labmates, especially Dr.Vijutha Sunny, Dr. Reena Mary, Dr. Veena Sreejith, Dr.Smitha Ajith, Dr. Malini Jayaram, Dr. T N Narayanan and Dr. Senoy Thomas. Words are insufficient to express my sincere thanks to other ex-members of the lab including Dr. Asha Mary John, Dr.Sajeev U S, Dr. Abdul Jamal, Dr. Sagar S, Dr. Hysen Thomas, Dr. Mathew George, Dr. Prema K H, Mr. Sanoj, Mr. Ram Kumar, Mr. Tom Thomas Mr. Neeraj , Mr. Navaneet, Mr. Abhilash and Mr. Sreeraj for their affection and timely help. I would always cherish the memories with the present members of Magnetics laboratory for creating a warm environment and help for the completion of my work. Sweet moments with Ms. Lisha Raghavan, Mrs. Lija K Joy, Mr. Vasudevan Nampoothiri, Mr. Sudeep P M, Mr. Sivaraj S, Mr. Aravind P, Ms. Vinayasree S, Mrs. Sethulakshmi N, Ms. Beenamol, Ms. Archana and Mr. Thoufeeq were really memorable. My special thanks are due to my dear friends in other labs of the physics department for extending a warm friendship to me. I am at a loss for suitable words to tell my thankfulness to all of them.

Above all, I am duty bound to extend, my thanks and gratitude to my kith and kin like my grandparents, my siblings, my in-laws and others closely related to me. Needless to say I am greatly indebted to them for their love, affection, caring and incessant support and encouragement all of them have given me. I must specially mention here in this context about my brother and my husband who extended all the encouragement, motivation, help and support I needed. Their role in my success has never been no less important. But more importantly the part played by the tiny tot, my son, a recent addition in our family has also been invaluable. He filled me with zest, enthusiasm and energy to put myself forward daring all odds towards achieving my target. Any amount of words won't be sufficient to express my gratitude. Actually I am short of words to tell my thanks to them. Truly, as the saying has it "Words are few when the heart is full". Actually had it not been for their help, support and encouragement I would not have accomplished this. I entirely owe all my gains to my loving parents and all those related to me and my family.

Last but not the least, my thanks are due to the God Almighty for his kind and generous blessings which made my achievements happen. I am aware and believe that it is not on our merits, but on His Grace things do happen. He ordains it. I pray to him and wish let us all be showered with his blessings at all times.

With prayers, I dedicate this humble work of mine to all who contributed to making it a reality, like my teachers, parents and relatives, colleagues, friends and all other well wishers and benefactors.

Geetha P

CONTENTS

Preface

Magnetism and magnetic materials have been playing a lead role in improving the quality of life. They are increasingly being used in a wide variety of applications ranging from compasses to modern technological devices. Metallic glasses occupy an important position among magnetic materials. They assume importance both from a scientific and an application point of view since they represent an amorphous form of condensed matter with significant deviation from thermodynamic equilibrium. Metallic glasses having good soft magnetic properties are widely used in tape recorder heads, cores of high-power transformers and metallic shields. Superconducting metallic glasses are being used to produce high magnetic fields and magnetic levitation effect. Upon heat treatment, they undergo structural relaxation leading to subtle rearrangements of constituent atoms. This leads to densification of amorphous phase and subsequent nanocrystallisation. The short-range structural relaxation phenomenon gives rise to significant variations in physical, mechanical and magnetic properties. Magnetic amorphous alloys of Co-Fe exhibit excellent soft magnetic properties which make them promising candidates for applications as transformer cores, sensors, and actuators.

With the advent of microminiaturization and nanotechnology, thin film forms of these alloys are sought after for soft under layers for perpendicular recording media. The thin film forms of these alloys can also be used for fabrication of magnetic micro electro mechanical systems (magnetic MEMS). In bulk, they are drawn in the form of ribbons, often by melt spinning. The main constituents of these alloys are Co, Fe, Ni, Si, Mo and B. Mo acts as the grain growth inhibitor and Si and B facilitate the amorphous nature in the alloy structure. The ferromagnetic phases

such as Co-Fe and Fe-Ni in the alloy composition determine the soft magnetic properties. The grain correlation length, a measure of the grain size, often determines the soft magnetic properties of these alloys.

Amorphous alloys could be restructured in to their nanocrystalline counterparts by different techniques. The structure of nanocrystalline material consists of nanosized ferromagnetic crystallites embedded in an amorphous matrix. When the amorphous phase is ferromagnetic, they facilitate exchange coupling between nanocrystallites. This exchange coupling results in the vanishing of magnetocrystalline anisotropy which improves the soft magnetic properties. From a fundamental perspective, exchange correlation length and grain size are the deciding factors that determine the magnetic properties of these nanocrystalline materials. In thin films, surfaces and interfaces predominantly decides the bulk property and hence tailoring the surface roughness and morphology of the film could result in modified magnetic properties.

Surface modifications can be achieved by thermal annealing at various temperatures. Ion irradiation is an alternative tool to modify the surface/structural properties. The surface evolution of a thin film under swift heavy ion (SHI) irradiation is an outcome of different competing mechanism. It could be sputtering induced by SHI followed by surface roughening process and the material transport induced smoothening process. The impingement of ions with different fluence on the alloy is bound to produce systematic microstructural changes and this could effectively be used for tailoring magnetic parameters namely coercivity, saturation magnetization, magnetic permeability and remanence of these materials. Swift heavy ion irradiation is a novel and an ingenious tool for surface modification which eventually will lead to changes in the bulk as well as surface magnetic property. SHI has been widely used as a method for the creation of latent tracks in thin films. The

bombardment of SHI modifies the surfaces or interfaces or creates defects, which induces strain in the film. These changes will have profound influence on the magnetic anisotropy and the magnetisation of the specimen. Thus inducing structural and morphological changes by thermal annealing and swift heavy ion irradiation, which in turn induce changes in the magnetic properties of these alloys, is one of the motivation of this study.

Multiferroic and magneto-electrics is a class of functional materials with wide application potential and are of great interest to material scientists and engineers. Magnetoelectric materials combine both magnetic as well as ferroelectric properties in a single specimen. The dielectric properties of such materials can be controlled by the application of an external magnetic field and the magnetic properties by an electric field. Composites with magnetic and piezo/ferroelectric individual phases are found to have strong magnetoelectric (ME) response at room temperature and hence are preferred to single phasic multiferroic materials. Currently research in this class of materials is towards optimization of the ME coupling by tailoring the piezoelectric and magnetostrictive properties of the two individual components of ME composites. The magnetoelectric coupling constant (MECC) (α_{ME}) is the parameter that decides the extent of interdependence of magnetic and electric response of the composite structure. Extensive investigates have been carried out in bulk composites possessing on giant ME coupling. These materials are fabricated by either gluing the individual components to each other or mixing the magnetic material to a piezoelectric matrix. The most extensively investigated material combinations are Lead Zirconate Titanate (PZT) or Lead Magnesium Niobate-Lead Titanate (PMN-PT) as the piezoelectric, and Terfenol-D as the magnetostrictive phase and the

coupling is measured in different configurations like transverse, longitudinal and in-plane longitudinal.

Fabrication of a lead free multiferroic composite with a strong ME response is the need of the hour from a device application point of view. The multilayer structure is expected to be far superior to bulk composites in terms of ME coupling since the piezoelectric (PE) layer can easily be poled electrically to enhance the piezoelectricity and hence the ME effect. The giant magnetostriction reported in the Co-Fe thin films makes it an ideal candidate for the ferromagnetic component and $BaTiO_3$ which is a well known ferroelectric material with improved piezoelectric properties as the ferroelectric component. The multilayer structure of $BaTiO_3$- CoFe-$BaTiO_3$ is an ideal system to understand the underlying fundamental physics behind the ME coupling mechanism. Giant magnetoelectric coupling coefficient is anticipated for these multilayer structures of $BaTiO_3$-CoFe-$BaTiO_3$. This makes it an ideal candidate for cantilever applications in magnetic MEMS/NEMS devices.

$SrTiO_3$ is an incipient ferroelectric material which is paraelectric up to 0K in its pure unstressed form. Recently few studies showed that ferroelectricity can be induced by application of stress or by chemical / isotopic substitution. The search for room temperature magnetoelectric coupling in $SrTiO_3$-CoFe-$SrTiO_3$ multilayer structures is of fundamental interest. Yet another motivation of the present work is to fabricate multilayer structures consisting of CoFe/ $BaTiO_3$ and CoFe/ $SrTiO_3$ for possible giant ME coupling coefficient (MECC) values. These are lead free and hence promising candidates for MEMS applications. The elucidation of mechanism for the giant MECC also will be the part of the objective of this investigation.

Thus the main objectives of present investigation can be listed as follows:

i. Fabrication of Co-Fe amorphous thin films.

ii. Evaluation of structural and morphological modification of Co-Fe thin films by thermal annealing and its effect on interrelationship with the magnetic properties.
iii. Study the effect of swift heavy ion irradiation on the magnetic and topographical properties of amorphous alloy Co-Fe thin films and its influence on its magnetic properties.
iv. Fabrication of $BaTiO_3$-CoFe-$BaTiO_3$ multilayer structure and study the magnetoelectric coupling of the prepared multilayer structure.
v. Fabrication of $SrTiO_3$-CoFe-$SrTiO_3$ multilayer structure and to probe room temperature magnetoelectric coupling in these multilayer structures.
vi. Propose a mechanism for giant magnetoelectric coupling in multilayer films
vii. Correlation of results.

The proposed thesis is entitled "Tailoring Magnetic Properties of Co-Fe Thin Films by Topographical Modifications Using Thermal Annealing and Swift Heavy Ion Irradiation and Fabrication of Magnetoelectric Multilayers for Device Applications" and consists of seven chapters.

Chapter 1 gives an introduction to basic properties of ferromagnetic and ferroelectric materials, amorphous and nanocrystalline thin films. An introduction to magnetoelectric coupling mechanism in magnetoelectric multilayers is also discussed.

Chapter 2 sheds light on the theory of magnetism of metallic alloys and thin films. A detailed account on the influence of swift heavy ion irradiation in altering the morphological properties and in turn the impact of these changes on the magnetic properties is also dealt with in this chapter. A review on the mechanism of

coupling of ferromagnetic and ferroelectric multilayers is also provided in this chapter.

Chapter 3 briefly discusses the experimental details of fabrication techniques employed for the growth of thin films and multilayer structures. The various characterization tools utilized for evaluating the structure, morphology, composition, magnetic, electric and magnetoelectric properties are also discussed. A concise description of swift heavy ion irradiation technique used for the current study has is also given in this chapter.

In chapter 4, thermal annealing and irradiation effects on the microstructural, topographical and magnetic properties of Co-Fe amorphous thin films are presented. The inference from this set of studies is that upon thermal annealing, crystallization together with surface smoothening influences the magnetic properties of thin films. The variation in coercivity with SHI fluence is successfully explained based on the microstructural changes occurred in the film morphology during irradiation.

Multilayers of $BaTiO_3$-CoFe- $BaTiO_3$ have been fabricated employing a simple technique of sol gel spin coating and thermal evaporation. The magnetoelectric coupling studies carried out on these multilayer structures are presented in Chapter 5. The MECC obtained in this multilayer structure is the highest ever reported value to the best of our knowledge.

Chapter 6 is on the investigations of room temperature magnetoelectric coupling observed in $SrTiO_3$-CoFe- $SrTiO_3$ multilayer structure. The stress resulted from the giant magnetostriction of CoFe layer explains the ferroelectricity and room temperature magnetoelectric coupling observed in this multilayer structure.

In Chapter 7, the salient observations and the inferences drawn out of these investigations are presented. Possible fabrication of micro cantilevers using $BaTiO_3$-CoFe- $BaTiO_3$ multilayers in MEMS/NEMS applications is included as scope for future work in this concluding chapter.

The following publications have resulted during the course of these investigations.

Peer Reviewed Journal Publications

1 **G.Pookat**, T.Hysen, S.H.Al-Harthi, I.A.Al-Omari, R.Lisha, D.K.Avasthi, M.R. Anantharaman; Nuclear Instruments and Methods in Physics Research B 310 (2013) 81-86

2 **G. Pookat**, H. Thomas, S. Thomas, S.H. Al-Harthi, L.Raghavan, I.A. Al-Omari, D. Sakthikumar, R.V. Ramanujan, M.R. Anantharaman; Surface & Coatings Technology 236 (2013) 246–251

3 Swapna S. Nair, **Geetha Pookat**, Venkata Saravanan, and M. R. Anantharaman; Journal of Applied Physics 114, 064309 (2013)

4 S Thomas, **G Pookat**, S S Nair, M Daniel, B Dymerska, A Liebig, S H Al-Harthi, R V Ramanujan, M R Anantharaman, J Fidler and M Albrecht; J. Phys.:Condens. Matter 24 (2012) 256004 (8pp)

5 T. Hysen, Salim Al-Harthi, I. A. Al-Omari, **P. Geetha**, R. Lisha, R. V. Ramanujan, D. Sakthikumar and M. R. Anantharaman; Journal of Magnetism and Magnetic Materials 341 (2013) 165–172

6 R Lisha, T Hysen, **P Geetha**, D K Avasthi, R V Ramanujan, M R Anantharaman; Mater. Res. Express 1 (2014) 015707

7 T. Hysen, **P. Geetha**, Salim Al-Harthi, I. A. Al-Omari, R. Lisha, R. V. Ramanujan, D. Sakthikumar, D. K. Avasthi and M. R. Anantharaman; Journal of Magnetism and Magnetic Materials 372 (2014) 224–232

8 Lisha Raghavan, Hysen Thomas**, Geetha Pookat**, Sunil Ojha, D K Avasthi, M R Anantharaman; (Under revision in Journal of Magnetism and Magnetic Materials)

9 Swapna S. Nair, **Geetha P**, K Sudheendran,K. Venkata Saravanan, M. R. Anantharaman; (Submitted to Euro Physics Letters)

Conference Proceedings

1. Transparent Magnetic Nanocomposites Based On Iron Oxide And SiO_2; **Geetha P**, Thomas S, Sakthikumar D, Yoshida Y and Anantharaman M R; National Conference on New horizons in theoretical and experimental physics, NHTEP 2007, Cochin University of Science and Technology, Cochin, India, Oct 8-10, 2007
2. Synthesis and Characterization of Transparent Magnetic Nanocomposites Based on Iron Oxide and SiO_2 ; **Geetha P**, Thomas S, Sakthikumar D, Yoshida Y and Anantharaman M R; International Conference On Nano Science And Technology-ICONSAT, IIT Bombay, Mumbai, India, February 17-20, 2010
3. Giant magnetoelectric coupling in BTO-METGLAS-BTO nanophasic multilayered thin films; **Geetha P**, Swapna S. Nair, Nikolai A. Sobolev, Andrei L. Kholkin, M. R. Anantharaman; International Conference on Materials for Advanced Technologies IUMRS- ICYRAM, Singapore-July 1-6 2012, Singapore
4. Investigations on Co-Fe thin films for possible MEMS applications; Hysen Thomas, Anantharaman M R, **Geetha Pookat**, Salim Al Harthi, Imad Al Omari; International Conference of Young Researchers on Advanced Materials-ICYRAM-2012; 1-6th July 2012; Singapore
5. Cooling field dependent exchange bias effects in naturally oxidised Fe- Ni based metallic glass nanostructures; S.Thomas, **G. Pookat**, S.S. Nair, M. Daniel, R.V.

Ramanujan, M. R. Anantharaman and M. Albrecht; Third international conference on frontiers in nanosccience and technology, COCHIN NANO-2011, Aug 14-17,2011, Cochin University of Science and Technology, Cochin, India

6. Exchange bias effects in naturally oxidised Fe-Ni-B based amorphous nanostructure; Senoy Thomas, **G. Pookat**, M. Daniel, M. R. Anantharaman, M. Albrecht; Magnetic Fields in the Universe III, Aug 21-27, 2011, Zakopane, Poland
7. Fabrication of Nano crystalline thin film based on Iron Nickel for MEMS applications-An initial study; Lisha Raghavan, Hysen Thomas, **Geetha Pookat** and M R Anantharaman, India Israel Meeting on Material science and Nanoscience - IIMNN 2013, Jan 31-Feb 1, 2013, Kottayam, India
8. Depth profiling in Zinc Ferrite - Metglas bilayer films using Rutherford Backscattering Spectrometry; Lisha Raghavan, Hysen Thomas, **Geetha Pookat**, Sunil Ojha, M R Anantharaman, International Conference on Nanostructuring by Ion Beams-ICNIB-2013, Oct 23-25, 2013, Jaipur, India
9. Evolution of topographical and magnetic properties of zinc ferrite thin films with annealing; Lisha Raghavan, Hysen Thomas, **Geetha Pookat**, Devesh Kumar Avasthi, M R Anantharaman, International conference on Magnetic Materials and applications-MagMA 2013, Dec 5-7, 2013, Guwahati, India
10. Tailoring topographical and magnetic properties of zinc ferrite thin films by 100 MeV Ag7+ ion irradiation; Lisha R, Hysen T, **Geetha P**, Shareef M, Shamlath A, Sunil Ojjha, Indra Sulaniya, D K Avasthi, M R Anantharaman, International conference on Magnetic Materials and applications, ICMagMA 2014, September 15-17, Pondichery, India

11. Ion Irradiation induced modification of materials; Lisha Raghavan, Hysen Thomas, **Geetha P**, M R Anantharaman, National Seminar on Frontiers of Nanotechnology 2014, March 6-7, 2014, Cochin, India
12. Ion Irradiation: A versatile tool for material modification; Lisha Raghavan, Hysen Thomas, **Geetha P**, M R Anantharaman, National seminar on Current trends in material science 2014, August 13-14, 2014, Cochin, India
13. Effect of substrate temperature on the structural, topographical and magnetic properties of zinc ferrite thin films; Lisha Raghavan, Hysen Thomas, **Geetha P**, M R Anantharaman, ISAS National conference on Advanced Technologies for Material Processing and Diagnostics, September 18-20, 2014, Cochin, India

CHAPTER 1

INTRODUCTION

Magnetism has its roots in the history of natural science as one of the oldest phenomena. It is said that a shepherd in Asia Minor, in the Magnesia district of Macedonia or in the city of Magnesia in Ionia picked up a stone which was stuck to the iron tip of his stick. The word 'Magnetism' is supposed to be originated from these names of cities. If these stones are properly suspended, they will always align themselves in the north- south direction. These natural magnets are known as 'lodestones' or 'loadstones', having a word meaning 'direction' and are a natural oxide of iron magnetized by a bolt of lightning, found to attract pieces of iron and other lodestones. The first systematic study of magnetism was carried out by William Gilbert (1540-1603) in the sixteenth century. He discovered that earth is a magnetic entity. German scientist Carl Friedrich Gauss (1777-1855) carried out theoretical investigations about the nature of earth's magnetism. Later, in the eighteenth century Frenchman Charles Coulomb (1736-1806) established the inverse square law of force, which states that the attractive force between two magnetized objects is directly proportional to the product of their individual fields and inversely proportional to the square of the distance between them. Danish physicist Hans Christian Oersted (1777-1851) proposed a link between electricity and magnetism. Andre Marie Ampere (1775-1836) and Michael Faraday (1791-1869) conducted experiments involving the effects of magnetic and electric fields on one another. Later, James Clerk Maxwell (1831-1879) laid the theoretical foundation to the physics of electromagnetism in the nineteenth century by stating that electricity and magnetism represent different aspects of the same fundamental force field.

During the nineteenth and twentieth centuries, the area of magnetism cherished the contributions originated from the works of Pierre Curie (1859-1906), Madame Marie Curie (1867-1934) and Pierre Weiss (1865-1940). Weiss proposed molecular field theory which explained magnetism on the basis of an internal molecular field proportional to the average magnetization that spontaneously align the electronic micromagnets in magnetic matter. The latest explanations of magnetism are based on quantum electrodynamics which deals with the theory of the motion and interactions of electrons in atoms. This theoretical model was proposed by Ernest Ising and Werner Heisenberg (1901-1976). In 1988, German and French physicists discovered the giant magnetoresistance (GMR) effect which marked the beginning of spintronics or spin-based electronics.

Another class of materials that has made big differences in our daily life is ferroelectric materials, which are the electrical counterparts of ferro/ferrimagnetic materials. The generation of spontaneous polarization even after the removal of an applied electric field is termed as ferroelectricity. The physical laws governing ferroelectricity and ferro/ferrimagnetism are almost similar. All ferroelectric materials are necessarily both pyroelectric and piezoelectric. Ferroelectric materials with switching property are employed in matrix addressed memories; shift registers and switches known as transchargers or transpolarizers. Memories, oscillators and filters are combined devices based on switched ferroelectric and piezoelectric properties, while the analogous use of electro-optic properties results in light switches, displays and memories. A variety of display devices, in which light can be stored and emitted in a controlled manner make use of circuits

containing both ferroelectric and electroluminescent components. This is also possible using photoconductor and ferroelectric components, which also permit direct x-ray to light conversion displays.

Magnetic and ferroelectric materials pervade every aspect of modern science and technology. For example, ferromagnetic materials with switchable spontaneous magnetization M controlled by an external magnetic field H have been widely used in data-storage technologies. The discovery of giant magnetoresistance effect appreciably promoted magnetic memory technology and incorporated it into the eras of magnetoelectronics or spintronics. Materials which exhibit both magnetic and electrical ordering are scarce, but research interest in magnetoelectric phenomena has led to the development of novel materials with an enhanced ME coupling. Multiferroic materials are special types of materials in which two or three ferroic-order parameters (ferroelectric, ferromagnetic, ferroelastic) occur. The coexistence of several order parameters will bring out novel physical phenomena and offers possibilities for new device applications. The coupling between these ordered phases is often weak, and the mechanisms for the ME coupling in multiferroics are highly dependent on the electronic structure and lattice properties.

1.1 Magnetism- Fundamentals

The fundamental quantity that decides the magnetic property of a material is magnetic dipole moment and the atomic origin of magnetism lies in the orbital and spin motions of electrons. Different types of magnetism are defined on the basis of materials response to magnetic fields. Although all matter is magnetic, non magnetic material arises because of the absence of collective interaction of

atomic magnetic moments in such materials. In magnetic materials, there is a very strong interaction between magnetic moments. Based on this interaction the materials can be classified in to different groups. They are

1. Diamagnetism

Diamagnetic substances have completely filled orbital shells with no unpaired electrons and hence no net magnetisation. When exposed to a magnetic field, a negative magnetisation is produced and hence possess small and negative magnetic susceptibility ($\chi \approx -10^{-5}$). In diamagnetic materials, susceptibility is temperature independent. Quartz (SiO_2), calcite ($CaCO_3$), water etc. are well known examples of diamagnetic substances.

2. Paramagnetism

Some of the atoms or ions in this class of material have a net magnetic moment due to the unpaired electrons in partially filled orbitals. But these individual magnetic moments do not interact magnetically and hence the net magnetisation is zero when the applied field is removed. In an applied magnetic field such materials show a net magnetisation due to the partial alignment of the atomic magnetic moments in the direction of applied filed. This results in a net positive magnetisation and positive susceptibility ($\chi \approx 10^{-5}$). An increase in temperature will randomize the alignment of magnetic moments thereby resulting in a temperature dependent susceptibility known as Curie law. Aluminum, platinum and manganese are well known paramagnets.

3. Ferromagnetism

Ferromagnetic materials possess a large net magnetisation due to the parallel alignment of moments even in the absence of an external magnetic field.

These materials have high magnetic susceptibility coming in the range 50 to 10,000. A strong interaction exists between the magnetic moments of nearby atoms to align them parallel resulting in a net magnetisation. These interactions are produced by exchange forces which result in parallel or antiparallel arrangement of atomic moments. Ferromagnetic materials exhibit two characteristic phenomena namely (1) spontaneous magnetisation and (2) the existence of magnetic ordering temperature.

The net magnetisation that exists inside a uniformly magnetized volume even in the absence of an applied field is known as spontaneous magnetisation and the maximum magnetisation that can be induced by the application of a magnetic field is termed as saturation magnetisation. At 0K, the value of spontaneous magnetisation depends on the spin magnetic moments of electrons. Saturation magnetisation is an intrinsic property. It is a temperature dependent parameter. Above a temperature called Curie temperature T_C, thermal energy overcomes the exchange forces and randomizes the moments of a ferromagnetic material to make it paramagnet.

4. Antiferromagnetism

Nearest neighbour moments is aligned antiparallel in antiferromagnetic materials with negative nearest neighbour interactions. We can divide the material into two sublattices A and B with the moments on one sublattice interacting with the moments on the other sublattice with a negative coupling coefficient but a positive coupling coefficient on their own sublattice. Hence the magnetic moments on the two sublattices point in different directions. If A and B sublattice moments are exactly equal and opposite, the net moment is zero. This type of

magnetic ordering is called antiferromagnetism. Antiferromagnets have weak but positive susceptibility. When an external field is applied, the energy decrease by moments that aligns in the field direction in one sub lattice is counter balanced by the energy increase in the other. The net moment is nonzero below a transition temperature, known as Neel temperature, T_N above which the moments turn paramagnetic behavior. The magnetic susceptibility is given by the Curie Weiss law with a negative value of θ.

5. Ferrimagnetism

Ferrimagnetic order was first suggested by Neel in 1948 [1]. In ferrimagnets, the magnetic moments of the A and B sublattices are not equal and result in a net magnetic moment. They possess a spontaneous magnetization below the Curie temperature and are organized into domains. Since the magnetization of each sublattice is different and has different temperature dependence, the Curie Weiss law is not obeyed. Magnetite is a well known ferrimagnetic material.

The ordering of magnetic dipole moments in different class of magnetic materials are shown in figure 1.

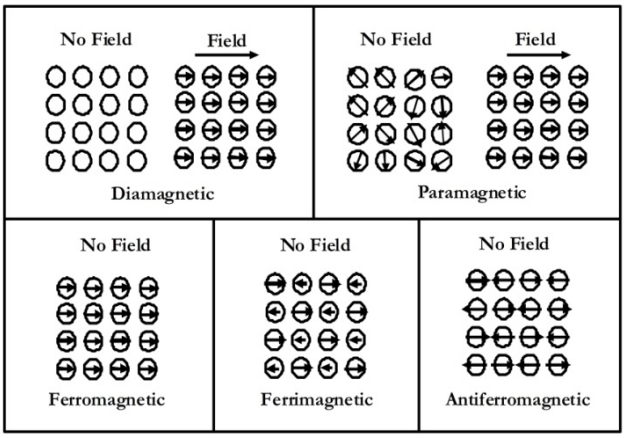

Fig. 1.1 Ordering of magnetic dipoles in magnetic materials

In general, magnetic materials can be classified as soft and hard magnetic materials [2]. In soft magnetic materials the domain wall motion is easy, resulting in very low coercivity and such materials are easy to magnetize and demagnetize. Large magnetic susceptibility and permeability are two specific characteristics of these soft magnetic materials. Hard magnetic materials possess large remanence and coercivity and hence are difficult to demagnetize and are conventionally used for making permanent magnets.

Magnetic materials can be again classified based on the crystallinity of the samples viz., crystalline and amorphous magnetic materials. In earlier days, the study of amorphous magnetic materials was not given serious consideration due to the belief that magnetic ordering and structural disorder are incompatible with each other. Later on amorphous materials also assumed importance as they exhibited magnetic properties. Owing to the soft magnetic properties, the magnetic amorphous alloys have excelled in applications ranging from low to high frequencies. Another class of materials that offer much more outstanding soft

magnetic properties than their amorphous counterparts are nanocrystalline materials. Generally such materials possess a biphasic structure with soft magnetic nanocrystalline grains embedded in a magnetic/non-magnetic phase [3-6]. Nanocrystalline alloys can be synthesized from amorphous alloy precursors by various methods viz., melt quenching, splat cooling, laser glazing, electro-deposition, ion implantation, sand blasting, swift heavy ion irradiation, thermal annealing and vapour quenching [7].

1.2 Amorphous magnetic alloys

Amorphous magnetic alloys are alloys of magnetic metals like cobalt and iron which have been melted and cooled rapidly. This rapid cooling process results in the random arrangement of atoms with no preferred crystalline directions. It is an interesting fact that both single crystals and completely amorphous materials have equal importance in technological/ engineering applications as the magnetic properties of materials are structure sensitive. The presence of grain boundaries affect the domain wall motion and thus affect the magnetic properties of these class of materials. Certain amorphous materials are mechanically strong and isotropic and may be produced by relatively simple manufacturing methods. This makes them ideal candidates for soft magnetic applications compared to their crystalline counterparts. For example, ferromagnetic amorphous alloys containing Fe or Co generally show excellent soft magnetic properties when compared to conventional crystalline soft magnetic materials. In amorphous magnetic materials, magnetism is determined by exchange interactions and randomly oriented local magnetic anisotropies. The atomic magnetic moments in amorphous magnets usually get arranged either in

ferromagnetic order, ferrimagnetic order or in canted ferrimagnetic order. The existence of ferromagnetism in amorphous alloys was theoretically predicted by Gubanov in 1960 [8]. According to Gubanov, amorphous solids would be ferromagnetic as the electronic band structure of crystalline solids does not change in any fundamental way upon transition to amorphous state. This implies that the band structure is basically controlled by short range order.

1.3 Nanocrystalline magnetic alloys

Nanocrystalline materials are obtained by crystallizing amorphous precursors using various techniques. Techniques like vapour deposition, mechanical alloying, plasma processing or rapid solidification from the liquid state can be employed for synthesizing such nanocrystalline alloys [9]. These class of nanocrystalline magnetic alloys consists of small (few nanometer sizes) ferromagnetic grains embedded in an amorphous matrix. Such nanocrystalline materials exhibit excellent soft magnetic properties like low coercivity, high permeability, low energy losses etc. In 1988, Yoshizawa, Oguma, and Yamauchi at Hitachi Metals, Ltd., developed the first nanocrystalline soft ferromagnetic alloy, called Finemet^{TM} with compositions corresponding to $Fe_{73.5}Si_{13.5}Nb_3B_9Cu_1$ [10]. Later, Suzuki et al. developed the Nanoperm^{TM} ($Fe_{88}Zr_7B_4Cu_1$) with a higher concentration of ferromagnetic transition metal [11]. Both these alloys have two phase microstructures in which the amorphous phase provides a high resistance path to eddy current formation and hence increase the possible operation frequency range over the existing large grain metallic alloys. Shortly after the discovery of excellent soft magnetic properties of these alloys, Herzer put forward a theory for their behaviour. This random anisotropy model [12] was a

modified version of the Alben, Becker, Chi model for the evolution of magnetic properties of nanocrystalline materials [13]. Random anisotropy model explains the soft magnetic property of the nanocrystalline material on account of the random orientation of nanocrystallites and grain sizes smaller than the exchange correlation length. This model suggests that the nanocrystallites should remain exchange coupled to maintain the reduced coercivity. Above Curie temperature this exchange coupling of ferromagnet becomes negligible. Typically the Curie temperature of the amorphous phase is smaller than that of the crystalline phase. Hence above Curie temperature, Herzer model is no longer valid and the coercivity of the nanocrystalline alloy increases. The composition of nanocrystalline alloys for high temperature applications are constrained to Co-based or Co-Fe based alloys due to high Curie temperature of these materials. By varying the Co/Fe ratio the magnetization and magnetocrystalline anisotropy can be controlled.

1.4 Swift heavy ion irradiation

Swift heavy ion bombardment induced effect and structural modification of solids have been studied for decades. First nuclear particle accelerator was assembled in 1930's to probe into the nucleus. Since then, particle accelerators have been playing an important role in material science. Nowadays, accelerators which can deliver particles with an energy ranging from few keV to several hundreds of GeV are available. Particles or ion beams accelerated using these accelerators are classified into two according to the energy imparted in the materials through which it passes. They are the low-energy and high energy heavy ion beams. Low energy ion beams have an energy ranging from few keV to few

hundreds of keV, which losses energy to the material (up to 10 keV/ amu) through elastic collisions with the nucleus or atoms of the material. This type of energy loss is called 'nuclear energy loss' $(dE/dx)_n$. High energy heavy ions known as "swift heavy ions (SHI)" have energy ranging from few tens of MeV to few GeV and losses energy to the target (≥ 1 MeV/amu) predominantly via inelastic collisions with the target material. These projectile ions impart energy to the electron cloud and these electrons transfer energy to the lattice via electron-phonon interactions. This type of energy loss is called 'electronic energy loss' $(dE/dx)_e$ [14]. Different models were proposed to explain the effect of SHI in materials, coulomb explosion [15-16] and thermal spike model [17-19]. This kind of intense electronic energy deposition can be effectively used to modify material properties.

1.5 Piezoelectricity and Ferroelectricity

Piezoelectric and ferroelectric materials are extensively used in many technological and scientific applications. Ferroelectric materials are a special class of piezoelectrics, which exhibit, a large piezoelectric response. From an application point of view, sensors based on the piezoelectric effect transform mechanical energy into electrical energy and are used as accelerometers, and also for measurement of pressure and vibration. Other than these piezoelectric applications, optical, thermal and electrical properties of ferroelectrics are exploited in a large number of devices and components [20-22], including capacitors and nonvolatile memories where electrical voltage is used to displace electrical charge.

Ferroelectric effect was first discovered by Valasek in 1920, who obtained hysteresis curves for Rochelle salt. Later in 1935, Busch and Scherrer discovered ferroelectricity in KH_2PO_4. The anomalous dielectric properties of $BaTiO_3$ were discovered independently by Wainer and Solomon in 1942 in USA, by Ogawa in 1944 in Japan, and by Wul and Goldman in 1946 in Russia. Since then, research activity on ferroelectric materials has been rapidly increasing and resulted in the discovery of many new ferroelectric materials. The progress in integrated Si devices and thin film processing techniques in the late 1960's and early 1970's triggered the application potential of ferroelectric thin films for non-volatile memories [23-25]. In 1987, ferroelectric memory integrated with silicon complementary metal-oxide semiconductor (CMOS) was invented [26]. At the same time initial work on the integration of microsensors with microelectronics and the area of micro electro mechanical systems (MEMS) materialized. Nowadays, ferroelectric films found applications in a number of commercial, wide spread products that include memories, microwave electronic components, and micro devices with pyroelectric and piezoelectric microsensors/actuators.

Perovskite-structure oxides ABO_3 are the most widely studied and widely used ferroelectrics today, which have the prototypical cubic structure shown in figure 1.2. The cubic perovskite structure consists of a small cation, B, at the center of an octahedron of oxygen anions, with large cations, A, at the unit cell corners. There is a structural distortion to a lower-symmetry phase accompanied by the shift off-center of the small cation below the Curie temperature. The spontaneous polarization develops largely from the electric dipole moment created by this shift. The comparatively simple perovskite structure and the small number

of atoms per unit cell have made detailed theoretical studies of perovskite ferroelectrics possible and resulted in a good understanding of the fundamentals of ferroelectricity.

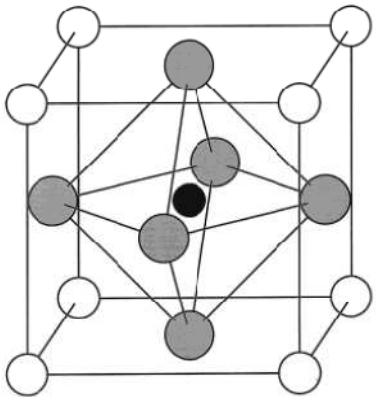

Fig. 1.2 Cubic perovskite structure. The small B cation (in black) is at the center of an octahedron of oxygen anions (in gray). The large A cations (white) occupy the unit cell corners [27]

1.6 Multiferroic and Magnetoelectric materials – A Review

Wilhelm Conrad Röntgen, in 1888 discovered that a moving dielectric turns to be magnetically active when placed in an electric field and in the reverse mechanism; a moving dielectric in a magnetic field gets polarized [28]. 17 years later in 1894, Pierre Curie pointed out the possibility for a material to be both ferromagnetic and ferroelectric [29]. Curie pointed out that the magnetoelectric effect is based on symmetry considerations. The materials in which both the ferromagnetism and ferroelectricity coexist are known as multiferroic materials. They are potential candidates for new spintronic materials which may enable the magnetic control of electrical properties. Magnetoelectric (ME) effect is the induction of magnetisation (or polarization) by an external electric (or magnetic)

field. The term magnetoelectric was first used by Debye in 1926. The first report on ME effect was by Schmid on nickel –iodine boracite $Ni_3B_7O_{13}I$, in 1966 [30]. In 1972, van Suchetelene originally proposed the concept of product ME property and this led to the development of first magnetic field sensor based on ME effect [31]. Here the composite material employed was a combination of $CoFeO_4$-$BaTiO_3$. Soon after, scientists from Philips Laboratory experimentally found that a large ME effect could be produced in eutectic compositions in the quinary Fe-Co-Ti-Ba-O system [32-35]. After long 20 years Newnham's group [36] and Russian scientists [37-39] prepared particulate ceramic composites of ferrites and $BaTiO_3$ or $Pb(ZrTiO_3)$ (PZT) by conventional sintering process. Even though the fabrication of these ceramic composites was easier and cost effective, they had lower ME coefficients than prior eutectic composites in Philips. This work inspired research on theoretical models like Green's function approach [40-41] and various micromechanical approaches [42-60] for understanding the coupling mechanism between the ferroic phases. In the early 2000s an upsurge is seen in the ME composite research. Among them the milestone work, both theoretical [61] and experimental [62-63] was on the bulk ME composites containing the giant magnetostrictive rare earth alloy Terfenol-D ($Tb_{1-x}Dy_xFe_2$). The giant ME response, with a ME voltage coefficient of larger than $1 Vcm^{-1}Oe^{-1}$, exhibited by such composites makes them ideal for many technological applications [60]. Later Dong and coworkers [64-80] have reported several combinations of laminate composites of Terfenol-D/piezoelectric ceramics and prototype ME devices based on these composites. In order to overcome the brittleness and high eddy current loss of the Terfenol-D disks used in two- phase composites, three- phase ME

composites with various connectivity schemes (including 0-3 type particulate composites, 2-2 type laminate composites, and 1-3 type fiber/rod composites) have been developed [81-90]. Later, nanostructured composite thin films of magnetic and ferroelectric oxides with 1-3 or 2-2 connectivity schemes have been developed [91-106]. In the last few years a number of experimental and theoretical [107-113] works have been conducted on such multiferroic ME nanostructures for exploring their potential in microelectronic devices.

1.7 Challenge of coupling magnetism and ferroelectricity

For a material to be a magnetoelectric multiferroic, it must be simultaneously ferromagnetic and ferroelectric. Hence it's allowed physical, structural and electronic properties are restricted to those that occur both in ferromagnetic and in ferroelectric materials. The limiting factors that restrict the simultaneous existence of ferromagnetism and ferroelectricity are:

1. Symmetry

From the fundamental point of view, the primary requirement for the existence of ferroelectricity is structural distortion from the symmetry structure that removes the center of symmetry and allows electric polarization. Among the different point groups, 31 point groups allow a spontaneous electric polarization, **P,** and 31 allow spontaneous magnetic polarization, **M** [114]**.** Out of these 13 point groups (1, 2, 2', m, m', 3, 3m', 4, 4m'm', m'm2', m'm'2', 6 and 6m'm') are common in both sets, allowing both properties to exist in the same phase. As this is not a small number; it is probably unlikely that symmetry plays an important role for the scarcity of magnetoelectric multiferroic materials.

2. Electrical properties

By definition, a ferroelectric material must be an insulator where as it is not a constraint for a ferromagnetic material. Electronically speaking, for most ferromagnets, the conductivity is due to high density of states at the Fermi level; but this is not true for ferroelectrics and insulators. There are only a few magnetic oxides such as half metallic magnets and ferrimagnetic oxides which exhibit reasonable spontaneous magnetism while being semiconducting or insulating.

3. Chemistry: d^0-ness

Common perovskite oxide ferroelectric materials require ions whose shells are filled and d^0 type electron configuration. Whereas, ferromagnetic systems require d- orbitals to be partially occupied for magnetic ordering to occur. Ions with fully filled shells are nonmagnetic as the spins of the electrons add to zero and hence do not participate in magnetic ordering. Long- range magnetic ordering within the material take place as a result of exchange interactions (virtual hopping of electrons) between the partially filled d shells of different ions. Most of the ferroelectric materials are transition metal oxides containing transition metal ions with empty d electron shells. Usually such materials become ferroelectric when the positively charged metal ions form covalent bonds with neighbouring negatively charged oxygen ions through the virtual hopping of electrons from the filled oxygen shells to the empty d shells. Hence an electric polarisation is induced within these materials as a result of a relative displacement of cations and anions within the periodic crystal. Even though magnetism and ferroelectricity share the same mechanism of electron exchange, it is the contrast of empty and

partially filled d or f electron shells that make the properties mutually exclusive [115].

1.8 Motivation of the present work

Co-Fe based alloy thin films represent an ideal template for studying magnetism at the alloy level and are widely sought after worldwide by scientists and engineers. Magnetic amorphous alloys of Co and Fe exhibit excellent soft magnetic properties and they are in great demand for various applications namely transformer cores, sensors, and actuators. With the advent of microminiaturization and nanotechnology, thin film forms of these alloys will be appropriate to be used as sensors, actuators and soft under layers for perpendicular recording media. The thin film forms of these alloys can also serve as magnetic micro electro mechanical systems (mag MEMS) or nano electro mechanical systems (NEMS) and hence thin film forms of these materials are also assume significance. Alloys of Co and Fe are excellent soft magnetic materials and grain size plays a very crucial role in deciding the magnetic properties of these materials. The grain correlation length often determines the soft magnetic properties of these alloys. The nanocrystalline counterparts of these materials have good soft magnetic properties compared to their crystalline or amorphous counterparts. The microstructure of nanocrystalline material consists of nanosized ferromagnetic crystallites embedded in an amorphous phase matrix. The ferromagnetic amorphous phase facilitate exchange coupling between nanocrystallites and this exchange coupling results in the vanishing of magnetocrystalline anisotropy which further improves the soft magnetic properties of nanocrystalline magnetic alloys. From a fundamental prospective, exchange correlation length and grain

size are the deciding factors which determine the magnetic properties of these alloys. In the thin film form, these alloys are coated on suitable substrates like silicon, glass or NaCl crystals. Surface property almost decides the bulk property of these films and hence modification of surface roughness and morphology of the film are very crucial. This can be achieved by thermal annealing at various temperatures and hence such an investigation is worthwhile.

Ion irradiation has been considered as an alternative tool to modify surface properties. The surface evolution of a thin film under swift heavy ion (SHI) irradiation will be an outcome of a competition between sputtering induced surface roughening process and the material transport induced smoothening process. It was thought that SHI would modify the surface structure of Co-Fe thin films and will eventually lead to modification of magnetic properties. The impingement of ions with different fluences on the alloy is bound to produce systematic microstructural changes and if these changes produce a pattern, this could effectively be used for tailoring the coercivity of these materials. The in situ method of tailoring coercivity using swift heavy ion is novel and is an ingenious tool in creating surface modification which will eventually lead to changes in the bulk property. SHI has been used as a means for the creation of latent tracks, phase transitions, amorphisation, damage creation, annealing effects, dimensional changes, and formation of nanostructures. From a fundamental point of view, most of the phenomenon taking place in the film due to the bombardment of SHI is in the boundary or in the interface or by the creation of defects, which induces strain. These changes will have profound influence in the magnetic anisotropy that will change the magnetisation substantially.

Multiferroics and magnetoelectrics are a class of functional materials in which magnetic order and electric fields can be coupled, are of fundamental interests to material scientists and engineers. The dielectric/magnetic properties of such materials can be controlled by the application of a magnetic/electric field. Currently research in this class of materials is towards optimization of the ME coupling by tailoring the piezoelectric and magnetostrictive properties of the two individual components of ME composites. The interdependence of magnetic and electric response of composite structure is determined by a parameter namely the magnetoelectric coupling constant (MECC) (α_{ME}). The most extensively investigated material combinations are terfenol-D as the magnetostrictive and lead zirconate titanate (PZT) or lead magnesium niobate-lead titanate (PMN-PT) as the piezoelectric phase. Magnetoelectric coupling of such heterostructures are measured in different configurations like transverse, longitudinal and in-plane longitudinal. The toxicity of the lead element makes such composites less attractive. Hence lead free components like $BaTiO_3$ or $SrTiO_3$ as ferroelectric phase is preferred in such ME composite structures. The giant magnetostriction reported in the Co-Fe thin films makes it an ideal candidate for the ferromagnetic component. Giant magnetoelectric coupling coefficient is anticipated for these multilayer structures of $BaTiO_3$-CoFe-$BaTiO_3$. Such a multilayer structure is an ideal system to understand the fundamental physics underlying the ME coupling mechanism. Also it is an ideal candidate for cantilever applications in MEMS/NEMS devices.

$SrTiO_3$ is an incipient ferroelectric material which is paraelectric up to 0K in its pure unstressed form. Recently few studies showed that ferroelectricity can

be induced by application of stress or by chemical / isotopic substitution. The search for room temperature ME coupling in $SrTiO_3$-CoFe-$SrTiO_3$ multilayer structures is of fundamental interest. These are lead free and hence promising candidates for MEMS applications. The elucidation of mechanism for the giant MECC is also another objective of this investigation.

1.9 Objectives

The main objectives of the present investigation are as follows.

- Fabrication of Co-Fe amorphous thin films
- Evaluation of structural and morphological modification of Co-Fe thin films by thermal annealing and establishing the interrelationship with its magnetic properties
- Study the effect of swift heavy ion irradiation on the magnetic and topographical properties of Co-Fe thin films and its influence on magnetic properties
- Fabrication of $BaTiO_3$-CoFe-$BaTiO_3$ multilayer structures and estimate the magnetoelectric coupling in these multilayer structures
- Fabrication of $SrTiO_3$-CoFe-$SrTiO_3$ multilayer structure and to evaluate the room temperature magnetoelectric coupling in these multilayer structures
- Propose a mechanism for the magnetoelectric coupling in these multilayers and correlation of results

References:

1. Neel, L. *Annales de Phys*., 3, (1948) 137
2. S. Chikazumi, S. H. Charap, *Physics of Magnetism*, Krieger Pub Co, New York, (1978)
3. Z. Bian, G. L. Chen, G. He, X. D. Hui, *Mater. Sci. Eng. A* 316, (2001) 135
4. L. Liu, C. L. Qiu, H. Zou, K. C. Chan, *J. Alloy Compd*. 399, (2005) 144
5. W. Chen, Y. Wang, J. Qian, G. C. Dong, *Acta Mater.,* 51, (2003) 1899
6. F. M. Alamgir, H. Jain, R.B. Schwarz, O. Jin, D. B. Williams, *Journal of Non-Crystalline Solids* 274 (2000) 289
7. Z. A. Chaudhury, C. Suryanarayana, *Metallography* 17 (1984) 231
8. A.I. Gubanov, *Sov. Phys. Sol. State*, 2, (1960) 468
9. McHenry, M. E.; Willard, M. A.; David, *E., Prog. Mater. Sci*. 44, (1999) 291
10. Y. Yoshizawa, S. Oguma, and K. Yamauchi, *J. Appl. Phys*. 64, (1988) 6044
11. K. Suzuki, M. Kikuchi, A. Makino, A. Inoue, and T. Masumoto, *Mat. Trans. JIM* 32, (1991) 961
12. G. Herzer, *IEEE Trans. Mag.* 26(5), (1990) 1397
13. R. Alben, J.J. Becker, M.C. Chi. *J. Appl. Phys*. 49 (1978) 1653
14. D.K. Avasthi, *Curr. Sci.* 78 (2002) 1297
15. G. Schiwietz, E. Luderee, G. Xiao, P. L. Grande, *Nucl. Instrum. Meth. B* 175 (2001) 1-11
16. R. L. Fleisher, P. B. Price, R. M. Walker, *Nuclear Tracks in Solids*, University of California Press, (1975)

17. Wolfgang Bolse, *Surf. Coat. Tech.* (2002) 1,158-159
18. F. Seitz, J. S. Koehler, *Solid State Phys*. 2 (1956) 305
19. Z. G. Wang, Ch. Dufour, E. Paumier, M. Toulemonde, *J. Phys.: Condens. Matter* 6 (1994) 6733
20. M. E. Lines, A. M. Glass, *Principles and Applications of Ferroelectrics and Related Materials*, Clarendon, Oxford (1979)
21. J. M. Herbert, *Ferroelectric Transducers and Sensors*, Gordon and Breach, New York (1982)
22. J. M. Herbert, *Ceramic Dielectrics and Capacitors,* Gordon and Breach, New York (1985)
23. D. W. Chapman, *J. Appl. Phys*. 40, (1969) 2381
24. M. H. Francombe, *Thin Solid Films* 13, (1972) 243
25. B. S. Sharma, S. F. Vogel, P. I. Prentky, *Ferroelectrics* 5, (1973) 69
26. S. S. Eaton, D. B. Butler, M. Parris, D. Wilson, H. McNeillie, *Dig. Tech. Pap.-IEEE Int. Solid-State Circuits Conf.* 130, (1988) 329
27. Nicola A. Hill, *J. Phys. Chem*. B 104, (2000) 6694
28. Rontgen W C, *Ann. Phys.* 35, (1888) 264
29. Curie P, *J. Physique* 3 (1894) 393
30. E.Ascher, H.Rieder, H.Schmid, H.Stossel, *J.Appl.Phys*. 37 (1966) 1404
31. V.Suchetelene, *Philips Res. Rep*. 27 (1972) 28
32. J. Boomgard, D. R. Terrell, R. A. J. Born, H. F. J. I. Giller, *J. Mater. Sci.* 9, (1974) 1705
33. A. M. J. G. Run, D. R. Terrell, J. H. Scholing, *J. Mater. Sci*.9, (1974) 1710
34. J. Boomgard, A. M. J. G. Run, V. Suchtelen, *Ferroelectrics* 10, (1976) 295

35. J. Boomgard, R. A. J. Born, *J. Mater. Sci.*13, (1978) 1538
36. G. Harshe, J. P. Dougherty, R. E. Newnham, *Int. J. Appl. Electromagn. Mater*. 4, (1993) 145
37. S. Lopatin, I. Lopatin, I. Lisnevskaya, *Ferroelectrics* 162, (1994) 63
38. T. G. Lupeiko, I. V. Lisnevskaya, M. D. Chkheidze, B. I. Zvyagintsev, *Inorg. Mater.* 31, (1995) 1245
39. M. I. Bichurin, I. A. Kornev, V. M. Petrov, I. Lisnevskaya, *Ferroelectrics* 204, (1997) 289
40. C. W. Nan, *Phys. Rev. B* 50, (1994) 6082
41. C. W. Nan and D. R. Clarke, *J. Am. Ceram. Soc*. 80, (1997) 1333
42. Y. Benveniste, *Phys. Rev. B* 51, (1995) 16424
43. I. Getman, *Ferroelectrics* 162, (1994) 45
44. T. Y. Chen*, J. Mech. Phys. Solids* 45, (1997) 385
45. T. Y. Chen, S. C. Chiang, *Acta Mech*. 121, (1997) 79
46. J. S. Lee, J. G. Boyd, D. C. Lagoudas*, Int. J. Eng. Sci.* 43, (2005) 790
47. J. Y. Li, M. L. Dunn, *Philos. Mag. A* 77, (1998) 1341
48. J. Y. Li, *Int. J. Eng. Sci.* 38, (2000) 1993
49. Q. J. Mech. *Appl. Math.* 56, (2003) 35
50. S. Srinivas, J. Y. Li, *Acta Mater*. 53, (2005) 4135
51. S. Srinivas, J. Y. Li, Y. C. Zhou, *J. Appl. Phys.* 99, (2006) 043905
52. L. J. Li , J. Y. Li, *Phys. Rev. B* 73, (2006) 184416
53. J. H. Huang, W. S. Kuo, *J. Appl. Phys.* 81, (1997) 1378
54. J. H. Huang, *Phys. Rev. B* 58, (1998) 12
55. T. L. Wu, J. H. Huang, *Int. J. Solids Struct.* 37, (2000) 2981

56. E. Pan, Z. Angew. *Math. Phys*. 53, (2002) 815
57. D. A. Filippov, *Tech. Phys. Lett*. 30, (2004) 351
58. H. T. Huang, L. M. Zhou, *J. Phys. D* 37, (2004) 3361
59. M. I. Bichurin, V. M. Petrov, O. V. Ryabkov, S. V. Averkin, G. Srinivasan, *Phys. Rev. B* 72, (2005) 060408
60. Y. Zhou, F. G. Shin, *J. Appl. Phys*. 100, (2006) 043910
61. C. W. Nan , M. Li , J. H. Huang , *Phys. Rev. B* 63, (2001) 144415
62. J. H. Ryu , S. Priya , A. V. Carazo , K. Uchino , H. E. Kim , *J. Am. Ceram. Soc*. 84 , (2001) 2905
63. S. X. Dong, J. R. Cheng , J. F. Li , D. Viehland , *Appl. Phys. Lett*. 83 , (2003) 4812
64. S. X. Dong, J. F. Li, D. Viehland, *Appl. Phys. Lett*. 83, (2003) 2265
65. S. X. Dong, J. F. Li, D. Viehland, *IEEE Trans. Ultrason. Ferroelectr. Freq. Control* 50, (2003) 1236
66. S. X. Dong, J. F. Li, D. Viehland, *J. Appl. Phys.* 95, (2004) 2625
67. S. X. Dong, J. F. Li, D. Viehland, *Appl. Phys. Lett*. 85, (2004) 2307
68. S. X. Dong, J. F. Li, D. Viehland, *J. Appl. Phys.* 96, (2004) 3382
69. S. X. Dong, J. F. Li, D. Viehland, *Appl. Phys. Lett*. 85, (2004) 2307
70. S. X. Dong, J. F. Li, D. Viehland, *Appl. Phys. Lett*. 85, (2004) 3534
71. S. X. Dong, J. F. Li, D. Viehland, *Appl. Phys. Lett.* 84, (2004) 4188
72. S. X. Dong, J. Y. Zhai, Z. P. Xing, J. F. Li, D. Viehland, *Appl. Phys. Lett*. 86, (2005) 102901
73. S. X. Dong, J. G. Bai, J. Y. Zhai, J. F. Li, G. Q. Lu, D. Viehland, S. J.Zhang, T. R. Shrout, *Appl. Phys. Lett*. 86, (2005) 182506

74. S. X. Dong, J. Y. Zhai, F. M. Bai, J. F. Li, D. Viehland, T. A.Lograsso, *J. Appl. Phys*. 97, (2005) 103902

75. S. X. Dong, J. Y. Zhai, N. G. Wang, F. M. Bai, J. F. Li, D. Viehland, T. A. Lograsso, *Appl. Phys. Lett.* 87, (2005) 222504

76. S. X. Dong, J. Zhai, J.F. Li, D. Viehland, *Appl. Phys. Lett.* 88, (2006) 082907

77. S. X. Dong, J. Y. Zhai, J. F. Li, D. Viehland, *Appl. Phys. Lett.* 89, (2006) 252904

78. S. X. Dong, J. Y. Zhai, J. F. Li, D. Viehland, *Appl. Phys. Lett*. 89, (2006) 122903

79. S. X. Dong, J. F. Li, D. Viehland, *J. Appl. Phys.* 100, (2006) 124108

80. S. X. Dong, J. Y. Zhai, J. F. Li, D. Viehland, M. I. Bichurin, *Appl. Phys. Lett*. 89, (2006) 243512

81. C. W. Nan, L. Liu, N. Cai, J. Zhai, Y. Ye, Y. H. Lin, L. J. Dong, C. X.Xiong, *Appl. Phys. Lett.* 81, (2002) 3831

82. J. G. Wan, J.-M. Liu, H. L. W. Chand, C. L. Choy, G. H. Wang, C. W.Nan, *J. Appl. Phys*. 93, (2003) 9916

83. C. W. Nan, N. Cai, L. Liu, J. Zhai, Y. Ye, Y. H. Lin, *J. Appl. Phys*. 94, (2003) 5930

84. N. Cai, J. Zhai, C. W. Nan, Y. H. Lin, Z. Shi, *Phys. Rev. B* 68, (2003) 224103

85. N. Cai, C. W. Nan, J. Y. Zhai, Y. H. Lin, *Appl. Phys. Lett*. 84, (2004) 3516

86. Y. H. Lin, N. Cai, J. Y. Zhai, G. Liu, C. W. Nan, *Phys. Rev. B* 72, (2005) 012405

87. C. W. Nan, N. Cai, Z. Shi, J. Zhai, G. Liu, Y. H. Lin, *Phys. Rev. B* 71, (2005) 014102

88. Z. Shi, C. W. Nan, J. Zhang, N. Cai, J. F. Li, *Appl. Phys. Lett*. 87, (2005) 012503

89. Z. Shi, C. W. Nan, J. Zhang, J. Ma, J. F. Li, J. *Appl. Phys*. 99, (2006) 124108

90. Z. Shi, J. Ma, Y. H. Lin, C. W. Nan, *J. Appl. Phys*. 101, (2007) 043902

91. H. Zheng, J. Wang, S. E. Lofland, Z. Ma, L. Mohaddes-Ardabili, T. Zhao, L. Salamanca-Riba, S. R. Shinde, S. B. Ogale, F. Bai, D. Viehland, Y. Jia, D. G. Schlom, M. Wuttig, A. Roytburd, R. Ramesh, *Science* 303, (2004) 661

92. H. Zheng, J. Wang, L. Mohaddes-Ardabili, M. Wuttig, L. Salamanca-Riba, D. G. Schlom, R. Ramesh, *Appl. Phys. Lett.* 85, (2004) 2035

93. F. Zavaliche, H. Zheng, L. Mohaddes-Ardabili, S. Y. Yang, Q. Zhan, P.Shafer, E. Reilly, R. Chopdekar, Y. Jia, P. Wright, D. G. Schlom, Y. Suzuki, R. Ramesh, *Nano Lett*. 5, (2005) 1793

94. J. G. Wan, X. W. Wang, Y. J. Wu, M. Zeng, Y. Wang, H. Jiang, W. Q. Zhou, G. H. Wang, J. M. Liu, *Appl. Phys. Lett*. 86, (2005) 122501

95. P. Murugavel, P. Padhan, W. Prellier, *Appl. Phys. Lett*. 85, (2004) 4992

96. P. Murugavel, D. Saurel, W. Prellier, C. Simon, B. Raveau, *ibid.* 85, (2004) 4424

97. M. P. Singh, W. Prellier, L. Mechin, C. Simon, B. Raveau*, J. Appl. Phys*. 99, (2006) 024105

98. J. P. Zhou, H. C. He, Z. Shi, C. W. Nan, *Appl. Phys. Lett*. 88, (2006) 013111

99. H. C. He, J. P. Zhou, J. Wang, C. W. Nan, *Appl. Phys. Lett.* 89, (2006) 052904

100. I. Levin, J. Li, J. Slutsker, A. L. Roytburd, *Adv. Mater*. (Weinheim,Ger.) 18, (2006) 2044

101. H. Zheng, F. Straub, Q. Zhan, P. L. Yang, W. K. Hsieh, F. Zavaliche, Y. H.Chu, U. Dahmen, R. Ramesh, *Adv. Mater*. (Weinheim, Ger.) 18, (2006) 2747

102. T. Wu, M. A. Zurbuchen, S. Saha, J. Mitchellm,S. K. Streiffer, *Phys. Rev. B* 73, (2006) 134416

103. N. Ortega, P. Bhattacharya, R. S. Katiyar, *J. Appl. Phys*. 100, (2006) 126105

104. W. Eerenstein, M. Wiora, J. L. Prieto, J. F. Scott, N. D. Mathur, *Nat.Mater.* 6, (2007) 348

105. Y. G. Ma, W. N. Cheng, M. Ning, and C. K. Ong, *Appl. Phys. Lett*. 90, (2007) 152911

106. H. C. He, J. P. Zhou, J. Wang, C. W. Nan, *Adv. Funct. Mater.* 17, (2007) 1333

107. C. W. Nan, G. Liu, Y. H. Lin, H. Chen, *Phys. Rev. Lett*. 94, (2005) 197203

108. G. Liu, C. W. Nan, J. Sun, *Acta Mater*. 54, (2006) 917

109. G. Liu, C.W.Nan, Z. K. Xu, H. Chen, *J. Phys. D* 38, (2005) 2321

110. C. G. Duan, S. S. Jaswal, E. Y. Tsymbal, *Phys. Rev. Lett*. 97, (2006) 047201

111. J. X. Zhang, Y. L. Li, D. G. Schlom, L. Q. Chen, F. Zavaliche, R.Ramesh, Q. X. Jia, *Appl. Phys. Lett*. 90, (2007) 052909

112. X. Lu, B. Wang, Y. Zheng, E. Ryba, *Appl. Phys. Lett*. 90, (2007) 133124

113. X Y Lu, B Wang, Y Zheng , E Ryba, *J. Phys. D* 40, (2007) 1614

114. Schmid, H. *Ferroelectrics,* 162, (1994) 317

115. S.W.Cheong, M. Mostovoy, *Nature Mater*. 6, (2007) 13

CHAPTER 2

THEORETICAL CONCEPTS

Experiment without theory is meaningless. A proper understanding of the underlying physics of various phenomena dealt in this thesis is necessary for a first reader of the thesis and also for ensuring continuity. This chapter briefly discusses various theoretical concepts associated with magnetism, modification of material properties with swift heavy ion, magnetoelectric coupling and other related phenomena.

2.1 Magnetism of metallic alloys

Amorphous metals and alloys are characterized by structural disorders or short range ordering which breaks the Bravais lattice. Even though their structure is thermodynamically metastable, they have well defined magnetic properties. Slater-Pauling curve which describes the ground state magnetisation vs. atomic number of the 3d transition metal alloys is shown in figure 2.1. Slater-Pauling curve can be used as a reference in deciding the alloy composition for a particular application. Here the curves consist of the line with a slope of -45^{O} from Cu to Fe and include Ni-Cu, Ni-Co, Co-Fe and Fe-Ni alloys. The 45^{O} line from Fe to Cr includes Fe-V and Fe-Cr and other alloys showing a rapid decrease of magnetisation.

From the Slater- Pauling curve it is evident that Co-Fe alloys exhibit the largest magnetisation values compared to other transition metal alloys. These Co-Fe alloys possess higher Curie temperature also, which makes them ideal for use in high temperature applications. The ferromagnetic transition elements Fe (Z=26), Co (Z=27) and Ni (Z=28) have partially filled $3d^6$, $3d^7$ and $3d^8$ respectively as the electrons will occupy singly before filling up in pairs.

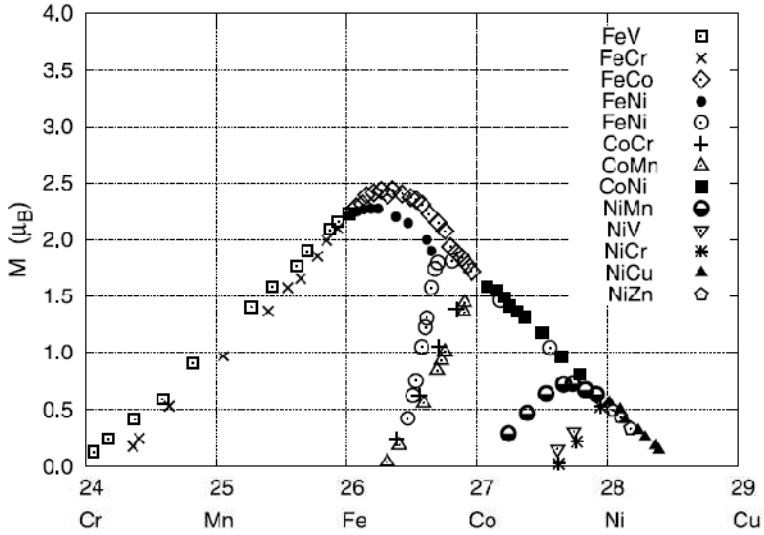

Fig.2.1 Slater–Pauling curves in transition metal alloys as a function of atomic number [1]

Even though we expect spin magnetic moments of 4, 3 and 2 Bohr magnetons (μ_B) for Fe, Co and Ni, these elements actually exhibit saturation magnetic moments of only 2.2, 1.7 and 0.6μ_B per atom respectively at 0K. From the Slater- Pauling curve it is clear that there is a decrease in saturation magnetisation by the addition of impurity atoms like Mn, Cr, V or Ti. These impurity atoms are coupled anti-ferromagnetically with the ferromagnetic material which in turn reduces the average magnetic moment [2].

2.2 Magnetic anisotropies

The term magnetic anisotropy refers to the influence of the crystal structure and shape of grains on the direction of magnetisation. The dependence of magnetic properties on a preferred direction is called the magnetic anisotropy. Magnetic anisotropy strongly affects the magnetic properties of a material such as hysteresis loops, coercivity and remanence. A ferromagnetic single crystal

exhibits 'easy' and 'hard' directions of magnetisation; *i.e*., the energy required to magnetize a crystal depends on the direction of applied magnetic field relative to the crystal axes. The mechanism by which these are preferentially oriented in a thin film structure is different with respect to a bulk.

Basically there are two main sources of magnetic anisotropy. They are dipolar interaction and spin-orbit interaction. The long range character of dipolar interaction results in its contribution to the anisotropy, which strongly depends on the shape of the sample. If spin-orbit and dipolar interaction are absent, the direction of magnetisation does not affect the total energy of electron-spin system. An applied field will try to rearrange the direction of the electron spin which is coupled with the orbit via spin-orbit interaction. However the orbit is strongly coupled with crystal lattice. Hence any attempt to rotate the spin axis is resisted and this is known as magnetocrystalline contribution to the anisotropy. Spin–orbit interaction is also responsible for the magneto-elastic or magnetostrictive anisotropy induced in a strained system and is due to the lattice mismatch between the adjacent layers in a multilayer system.

2.2.1 Magnetic dipolar anisotropy (Shape anisotropy)

The magnetic dipolar anisotropy or shape anisotropy is mediated by dipolar interaction. The contribution of this long range interaction is dependent upon the shape of the sample. Hence shape anisotropy becomes important in thin films and often produces in plane alignment of moments. Suppose a magnetic field is applied on a non-spherical specimen from right to left, and this result in a north pole at the left end and a south pole at the right end. In such a case the field induced inside the sample points from left to right *i.e*., in the opposite direction to

the applied external field. This internal field tends to demagnetize the specimen and hence is called the demagnetizing field $\mathbf{H_d}$. This demagnetizing field can be expressed as

$$\mathbf{H}_\mathrm{d} = -\mathrm{N}_\mathrm{d}\mathbf{M} \tag{2.1}$$

where N_d is the shape dependent demagnetizing factor and M is the magnetization vector.

In a thin film considered as a magnetic continuum, the dipolar anisotropy energy per unit volume is given by

$$E = \frac{1}{2}\mu_0 M_s^2 \cos^2\theta \tag{2.2}$$

where M_s is the saturation magnetisation and is assumed to be uniform throughout the film. θ is the angle subtended by magnetisation with the film normal. Hence the dipolar anisotropy energy is minimized for an angle 90^O *i.e.*, moments lying in the plane of the film [3].

2.2.2 Magnetocrystalline anisotropy

The microscopic origin of magnetocrystalline anisotropy is the spin- orbit interaction [4]. The exchange interaction and the dipolar interaction could also contribute to the magnetocrystalline anisotropy. Magnetocrystalline anisotropy is the energy needed to deflect the magnetic moment in a single crystal from the 'easy' to the 'hard' direction. The easy and hard directions arise from the interaction of the spin magnetic moment with the crystal lattice (spin-orbit coupling).

Even though the magneto crystalline energy is small compared to the exchange energy, direction of the magnetization is determined by the anisotropy

only as the exchange interaction just tries to align the magnetic moments parallel, no matter in which direction.

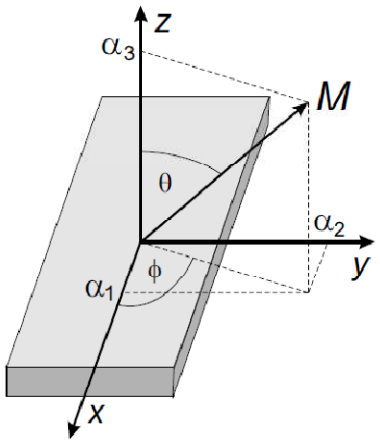

Fig. 2.2 Representation of the direction cosine [5]

The magnetization direction ($m = M/|M|$) relative to the coordinate axes are given by the direction cosine α_i as $\mathbf{m} = (\alpha_1, \alpha_2, \alpha_3)$ (figure 2.2) with

$$\alpha_1 = \sin\theta\cos\phi \tag{2.3}$$

$$\alpha_2 = \sin\theta\sin\phi \tag{2.4}$$

$$\alpha_3 = \cos\theta \tag{2.5}$$

These relations fulfill the condition

$$\alpha_1^2 + \alpha_2^2 + \alpha_3^2 = 1 \tag{2.6}$$

For a cubic system, the magnetocrystalline anisotropy energy is given as

$$E = K_1\left(\alpha_1^2\alpha_2^2 + \alpha_2^2\alpha_3^2 + \alpha_3^2\alpha_1^2\right) + K_2\left(\alpha_1^2\alpha_2^2\alpha_3^2\right) + \ldots \tag{2.7}$$

Where K_1, K_2 etc. are known as anisotropy constants.

For a hexagonal system this anisotropy energy can be expressed as

$$E = K_1 \sin^2\theta + K_2 \sin^4\theta + ... \tag{2.8}$$

In all materials anisotropy energy decreases with increase in temperature and there is no preferred orientation for domain magnetisation near Curie temperature.

2.2.3 Magneto-elastic anisotropy

The magneto-elastic effect again arises from the spin-orbit interaction. The spin moments are coupled to the lattice via the orbital electrons. If the lattice is altered by strain, the distance between the magnetic atoms are changed and hence the interaction energy also changes. This produces magneto-elastic anisotropy. By the application of a magnetic field, a previously demagnetized crystal experiences a strain that can be measured as a function of applied field along the principal crystallographic axes. There will be a change in the dimension of the material when it is magnetized.

If λ_{hkl} represent magnetostriction constants for various crystal directions, the magneto elastic energy per unit volume for an elastically isotropic medium with isotropic magnetostriction is defined as [6]

$$E = -\frac{3}{2}\lambda\sigma \cos^2\theta \tag{2.9}$$

where σ is the stress and θ is the angle between the magnetisation and stress directions.

2.3 Magnetic domains and domain wall structures

Any ferromagnetic or ferrimagnetic material is composed of small regions of atomic magnetic moments that are oriented in different directions. These

regions of the material that are magnetized in different directions are termed as magnetic domains and each one is magnetized to its saturation magnetisation. The boundaries between different domains are termed as domain walls. In 1919, Barkhausen found the first evidence for domain structure while monitoring the magnetisation of samples by converting changes in the magnetisation to audio signals. The first direct images of domain structures were shown by Francis Bitter in 1931. In the Bitter method, a colloidal solution of fine magnetic particles of magnetite, (Fe_3O_4) was used to cover the surface of the sample. The particles got deposited as a band along the regions of high field gradient that is along the domain boundaries. The patterns thus formed spurred further research in to domain theory. Advanced theories on domains were proposed by Landau and Lifshitz (1935), which shed light on the mechanism behind domain formation.

Weiss has shown that the alignment of magnetic moments within a ferromagnet occurs due to the interaction field between the atomic moments. Later Landau and Lifschitz showed that the existence of domains is a consequence of energy minimization. The domain formation minimizes the total magnetic energy of a ferromagnetic material. The main contributors to the magnetic energy are magnetostatic, magnetocrystalline and magnetostrictive energies. Magnetostatic energy is the principal driving force for domain formation and the magnetocrystalline and magnetostrictive energies influence the shape and size of domains.

Large magnetostatic energy is associated with a single domain structure, whereas the breakup of the magnetisation into smaller domains/ regions reduces this magnetostatic energy by providing flux closure at the ends of the specimen. A

ferromagnetic material with single domain has a macroscopic magnetisation which makes it to behave as a magnet with a magnetic field around it.

The energy per unit volume of a dipole of magnetisation M in a magnetic field H is given by

$$\boldsymbol{E} = -\mu_o \int \boldsymbol{H}.d\boldsymbol{M} \tag{2.10}$$

The magnetic field H may be substituted with the demagnetizing force, $\mathbf{H_d}$ generated by **M** which is given as

$$\mathbf{H}_\mathrm{d} = -\mathrm{N}_\mathrm{d}\mathbf{M} \tag{2.11}$$

where N_d is the demagnetizing factor. Hence the energy expression becomes

$$E = -\mu_o N_d \int \boldsymbol{M}.d\boldsymbol{M}$$

$$E = \frac{\mu_0}{2} N_d \boldsymbol{M}^2 \tag{2.12}$$

This expression represents the self energy of a single domain particle which depends on the demagnetizing field as well as magnetisation. This magnetostatic energy of the domains allows the ferromagnet to do work even against gravity such as lifting another ferromagnet. By dividing the single domain to several smaller regions/domains the magnetostatic energy can be minimized as the demagnetizing field depends mainly on the shape of the sample. Figure 2.3 shows the formation of domain walls to reduce the magnetostatic energy stored in domains. Here the magnetic moments at the boundary between the two domains are not able to align parallel thereby increasing the exchange energy of the ferromagnet. By the formation of closure domains during the magnetisation process, magnetostatic energy reduces to minimum.

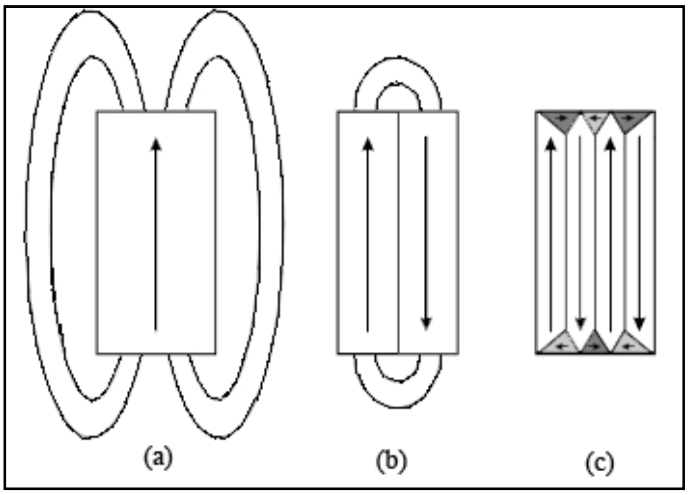

Fig. 2.3 Reduction of magnetostatic energy by domain formation

During the magnetisation process in a ferromagnetic crystal, magnetic moments tends to orient along certain preferred crystallographic directions namely 'easy axes' to achieve saturation magnetisation. These crystals can also achieve saturation magnetisation in other crystallographic directions known as 'hard axes' in a higher applied field and they will be in a higher energy state compared to those magnetized along easy directions. This phenomenon that causes the moments to align along the easy axes is known as magnetocrystalline anisotropy and the energy difference between samples magnetized along easy and hard directions is called the magnetocrystalline anisotropy energy. Reduction in magnetocrystalline energy can be achieved by domain formation. Figure 2.3 (c) shows the formation of closure domains which tends to align magnetic moments along easy directions thereby reducing magnetocrystalline energy.

When a magnetic field is applied on a ferromagnetic material, it undergoes elongation or contraction in the direction of magnetic field and this phenomenon is known as magnetostriction. Even though these length changes comes in the order of few tens of parts per million, they do influence the domain structure.

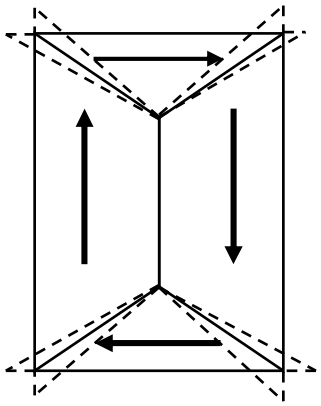

Fig. 2.4 Magnetostriction in closure domains

Figure 2.4 shows the magnetostrictive changes that occur in closure domains on the application of magnetic field. As the horizontal and vertical domains can't elongate at the same time, an elastic strain energy term is added to the total energy. This elastic energy is proportional to the volume of the domains of closure and the size reduction of closure domains by the formation of smaller domains reduces this energy contribution. Additional domain walls are introduced with formation of smaller domains and thereby increases the exchange and magnetostatic energy contribution. Thus the closure domain configuration shown in figure 2.3 (c) helps to reduce the total energy to a minimum value.

Magnetic changes in a ferromagnetic material occur at the boundary between the domains *i.e*., the direction change of magnetic moments at the domain walls decides the magnetic properties. If the domain wall is of infinitesimal in width, then the nearest neighbour moments belongs either to one domain or the other. Another possibility is a transition region between two domains where magnetic moment realignment takes place. This was first suggested by Bloch and these domain walls are commonly referred to as Bloch walls. Domain walls can be classified on the basis of the angle of magnetisation between two neighbored domains. They are,

- 180^{O} wall- The boundary between two domains having opposite magnetisation which is shown in figure 2.5 (a)
- 90^{O} wall- The boundary between two domains with perpendicular magnetisation and is shown in figure 2.5 (b)

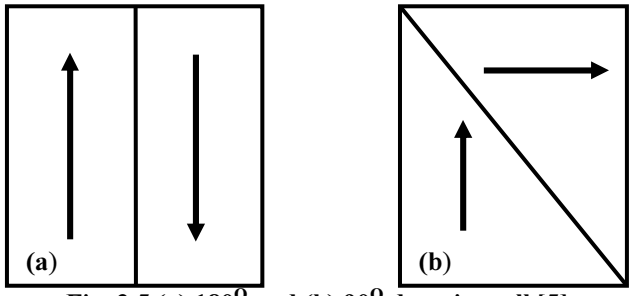

Fig. 2.5 (a) 180^{O} and (b) 90^{O} domain wall [5]

Depending on the crystallographic arrangement of the ferromagnet, different kinds of domain walls arises. A uniaxial ferromagnet like Co exhibit only 180^{O} domain wall. Bcc-Fe, which is a triaxial ferromagnet possesses 180^{O} as

well as 90^{O} domain walls. 180^{O} domain wall can be divided in to two classes. (a) Bloch wall and (b) Neel wall.

- Bloch wall

  The rotation of the magnetization occurs in a plane being parallel to the plane of the domain wall.

- Neel wall

  The rotation of the magnetization vector takes place in a plane which is perpendicular to the plane of the domain wall

Figure 2.6 (a) and (b) depicts the rotation of the magnetization in a Bloch wall and Neel wall respectively.

A vanishing stray field is assured by the Bloch wall. Typically, Neel wall is often observed in ferromagnetic thin film systems with an in-plane magnetization. In such a case, the magnetization remains within the film plane which is energetically favorable compared to the situation that the magnetization vector has to be perpendicular to the film plane which in turn reduce the magnetic stray fields and hence the magnetostatic energy.

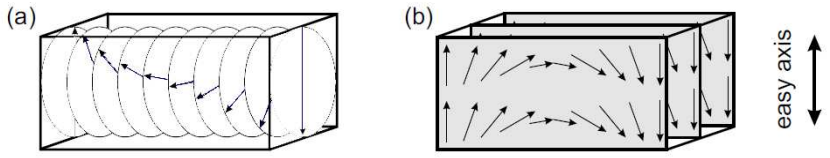

Fig. 2.6 Rotation of the magnetization in a (a) Bloch wall and (b) Neel wall [5]

According to domain theory, in a ferromagnet, atomic magnetic moments are in an ordered manner even in a demagnetized state. The difference between the demagnetized and magnetized state in such a material has its origin in

configuration of the domains. When a magnetic field is applied, the domains change shape and size by the movement of domain boundaries. Schematic of the domain rearrangement in magnetisation curve is shown in figure 2.7.

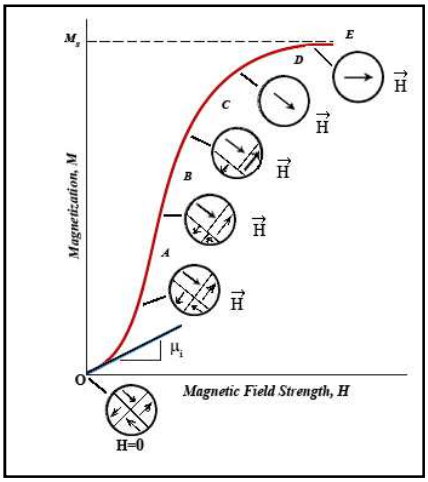

Fig. 2.7 Domain configurations for a ferro/ferrimagnetic material during different stages of magnetisation [4]

In the initial demagnetized state, the domain arrangement is in such a way that the magnetisation averages to zero (labeled O). When an external field is applied, domains that are aligned in the directions of the applied field grow at the expense of those that are unfavorably oriented (insets A through C). With increasing field strength, gradually it becomes a single domain (inset D), which is nearly aligned with the field. At the saturation point this domain gets aligned with the field (inset E). Grain growth occurs by domain wall motion. Actually on the application of a field, the moments within the domain walls are getting rotated. This is due to the fact that the resulting directions of the moments within the walls are a fine balance between the exchange and anisotropy energies. Hence a change

in field energy alters this balance resulting in the moments to rotate. Within the domain, the moments are locked in to a particular direction by the exchange interaction so that an external field cannot immediately alter the balance of the energy in another direction. If a weak field is applied in the 'down' direction the moments within the 'up' domain will not change as they are in a low energy state caused by their mutual interactions through the exchange field. Hence the net effect is that the moments within the wall rotate slightly in the field direction as the field is increased. It therefore appears as the domain wall motion. There is no translational motion at all [7].

2.4 Magnetostriction

In 1842, Joule discovered that the length of an iron rod increases when it is magnetized lengthwise by a weak field. This phenomenon of dimension change under the influence of a magnetic field is called magnetostriction. The deformation $\delta l/l$ caused by the magnetically induced strain is represented by λ.

$$\lambda = \delta l/l \tag{2.13}$$

The value of magnetostriction at magnetic saturation is known as saturation magnetisation λ_S. The value of λ can be positive, negative or zero in some alloys at room temperature. Usually, the magnitude of magnetostriction for a ferromagnetic material comes in the range 10^{-5} to 10^{-6}. Even though this deformation is small, magnetostriction is an important parameter in deciding the domain structure and technical magnetization. Figure 2.8 shows the dependence of λ on the extent of magnetization and hence on the applied field for a substance with positive magnetostriction.

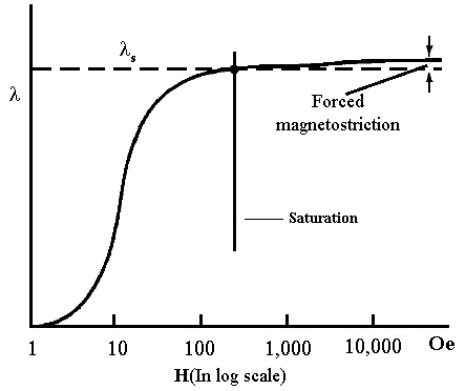

Fig. 2.8 Magnetostrictive elongation as a function of magnetic field [8]

The strain due to magnetostriction changes accordingly with increasing magnetic field and reaches a saturation. For understanding the dependence of strain on the direction of magnetization, consider a ferromagnetic sphere, which is having a radius of 1 when it is nonmagnetic, and gets elongated when it is magnetized to saturation. Let this elongation be $\delta l/l = e$ in the direction of magnetization or along the x-axis.

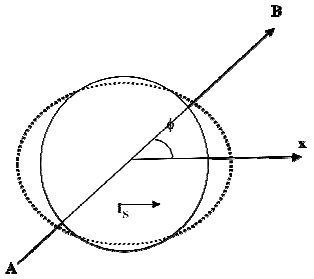

Fig. 2.9 Elongation of the radius of a sphere with unit radius in the direction of magnetization making an angle ϕ with the axis of spontaneous strain [9]

The strain along AB is given as

$$\left(\frac{\delta l}{l}\right)_{AB} = e.cos^2\phi \tag{2.14}$$

For random domain, (in demagnetized state)

$$\left(\frac{\delta l}{l}\right)_{demag} = \overline{e.cos^2\phi} = \int_0^{\frac{\pi}{2}} e\, cos^2\phi \sin\phi\, d\phi = \frac{e}{3} \tag{2.15}$$

In the saturated state, (*i.e* magnetized state)

$$\left(\frac{\delta l}{l}\right)_{sat} = e \tag{2.16}$$

Hence the saturation magnetostriction is given by,

$$\lambda_s = \left(\frac{\delta l}{l}\right)_{sat} - \left(\frac{\delta l}{l}\right)_{demag} = \frac{2}{3}e \tag{2.17}$$

Thus the spontaneous strain in the domain can be expressed in terms of magnetostriction as

$$e = \frac{3}{2}\lambda_S \tag{2.18}$$

Here the spontaneous strain is constant irrespective of the crystallographic direction of the spontaneous magnetization. This quantity is termed as isotropic magnetostriction.

2.5 Swift Heavy Ion Irradiation: Theory

Swift heavy ions are particle radiations accelerated to very high energies, typically in the MeV or GeV range having sufficient mass and energy to penetrate solids. These energetic ion beams play a crucial role in the field of material science research. The ion beam interacts with both electrons and nuclei of the target material. Ion energy, ion species and fluence decides the ion beam effect on the materials.

2.5.1 Energy loss

Ion penetration to the target material causes energy loss in the solid mainly due to collision with target electrons or target nuclei. Different mechanisms by which ion can lose energy in the target are (i) inelastic collisions leading to ionization or excitation of the electrons in the target (electronic energy loss), (ii) elastic collisions with the nuclei of target atoms (nuclear energy loss) and (iii) radiation loss such as Bremsstrahlung and Cerenkov radiation which is very small and can be neglected.

2.5.2 Nuclear and electronic stopping power

Stopping power of a medium for a particle is defined as the average ion energy loss per unit path length (a dragging force slowing down the ion) due to interactions with the atoms in the medium.

$$S = \frac{dE}{dx} \tag{2.19}$$

where E is the kinetic energy of the particle and x distance along the particle trajectory in the medium.

Stopping power of a target for an ion depends on different factors like ion energy and atomic number, and target element atomic number and density etc. Depending on ion energy/velocity, total stopping power can be categorized in to three independent parts.

$$S_{Total} = S_{Electronic} + S_{Nuclear} + S_{Radiative} \tag{2.20}$$

At low primary ion velocities, incoming ions interacts with screened nuclei of the target (nuclear stopping), and at high velocities, interaction will be with the target

electrons (electronic stopping). At ion beam energies well below the speed of light, $S_{radiative}$ can be neglected.

2.5.3 SHI induced modification

The basic difference of materials modification by ion implantation (low energy ions) and swift heavy ion (high energy) irradiation is that in ion implantation the incident low energy ions get embedded in the material whereas in swift heavy ion irradiation the impinging ions do not get embedded in the materials due to their larger range. For a swift heavy ion moving at a velocity comparable to Bohr velocity of electron, the dominant mechanism for energy transfer to the material is inelastic collisions between the projectile and atoms of the matter. By this collision, excitation and ionization of surrounding electrons takes place. The electronic energy loss value in each collision varies from a few eV/Å to a few keV/Å. While traversing through the material, SHI having an energy of 1 MeV/nucleon or more transfers its energy to the atoms in a solid, predominantly through inelastic scattering producing a trail of excited/ionized atoms. Cylinders containing highly charged ions and electrons are formed during the passage of SHI through the materials. After the passage of the SHI, the solid returns to its equilibrium state leaving behind bulk and surface modifications. Effect of SHI irradiation is different for different materials. The nature of material modification depends mainly on the thermal, electrical and structural properties of the target material. It also depends on the mass of the projectile ion and irradiation parameters. Thermal spike model and Coulomb explosion model were proposed to explain the effect of SHI irradiation in materials.

2.5.4 Thermal spike model

According to thermal spike model [10- 12], the energy transfer between the electrons of target material and SHI takes place in the form of kinetic energy via inelastic collision. Electron-phonon interactions transmit this kinetic energy to the lattice resulting in the increase of lattice temperature above the melting point of the material, followed by rapid quenching. This leads to the formation of 'amorphous track' along the trajectory of the projectile ion.

2.5.5 Coulomb explosion model

According to Coulomb explosion model [13-15], a cylinder of ionized atoms is formed and excited electrons are ejected by coulomb repulsion, just after the passage of the ion through matter. Schematic of the Coulomb explosion process is shown in figure 2.10.

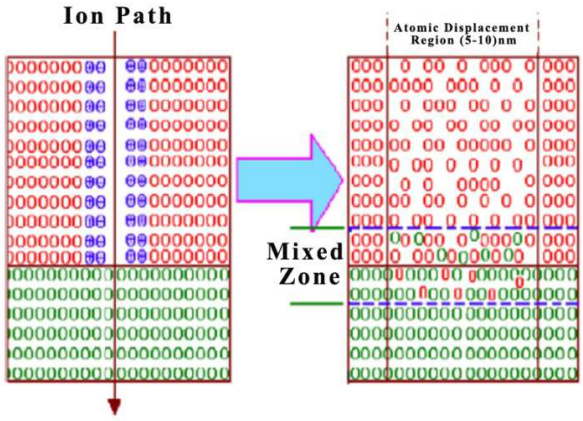

Fig. 2.10 Schematic of Coulomb explosion process [16]

This model seems to be well suited for insulating materials and in such a case the electron excitation energy is rapidly shared with other electrons via electron–electron interaction leading to the formation of latent tracks [17-19]. For

materials having large electronic mean free paths (for example metals), the free electrons carry away the excitation energy so efficiently that the sample warms up as a whole without considerable atomic motion.

2.6 Ferroelectrics- An introduction

Ferroelectrics are a special class of polar materials that display an electric polarization in the absence of an external electric field. Any macroscopic collection of matter is electrically neutral with nearly equal number of positive and negative charges. But it is not necessary that these charges are distributed within the volume of matter in a homogenous manner. If there is a disproportion between the number of positive and negative charges, then the material is said to have an electric dipole moment. The net dipole moment per unit volume is known as the spontaneous polarization [20].

In such a material, the direction of the spontaneous polarization vector may be switched between those orientations by an electric field. Different types of polarizations present in ferroelectric materials are

- Electronic polarization- A displacement of the electronic cloud with respect to the nucleus
- Ionic polarization- Separation of positive and negative ions in the crystal
- Orientational polarization- Alignment of permanent dipoles
- Space- charge polarization- Free electrons present in the system are prevented from moving by barriers such as grain boundaries

On the basis of crystal symmetry considerations, all ferroelectric materials must be pyroelectric and all pyroelectric materials must be piezoelectric. Eventhough spontaneous polarization is a fundamental property of pyroelectric

materials; it is reversible in ferroelectric materials only. A ferroelectric crystal consists of regions of homogenous polarization namely ferromagnetic domains. The direction of polarization is different in different domains. The region between two adjacent domains is called domain wall and the spontaneous polarization changes its direction in this region.

Ferroelectric properties of a ferroelectric material vanishes above a critical temperature namely Curie temperature (T_c). Most ferroelectric materials undergo a structural phase transition from a high-temperature non-ferroelectric (or paraelectric) phase into a low temperature ferroelectric phase. Some materials like barium titanate, $BaTiO_3$, undergo several phase transitions into successive ferroelectric phases. The transition into a ferroelectric phase usually leads to strong anomalies in the thermal, elastic, dielectric and other properties of the material [21-23]. This is accompanied by changes in the dimensions of the crystal unit cell and the associated strain is known as spontaneous strain. Polycrystalline ferroelectric materials may be polarized by the application of a strong electric field (10-100 kV/cm), usually at high temperatures. This process of creating net polarization in a material by applying sufficiently high electric field is called poling. The microscopic ferroelectric domains align themselves on the application of high electric field in a ferro/piezoelectric material. As the electric field is increased, more domains get oriented and, at a high electric field, almost all the domains are in the same direction resulting in a single large domain. In this stage the material achieves maximum polarization. If the material is kept at a high temperature (close to T_c but less than T_c) while the electric field is applied, the orientation of the domains is more smoother.

Polarization reversal mechanism of ferroelectric materials makes them ideal for switching applications. High values of dielectric constant and other properties near T_c may be exploited in non-switching applications. Switched ferroelectrics are employed in matrix addressed memories, shift registers and switches known as transchargers or transpolarizers. A variety of display devices make use of circuits containing both ferroelectric and electroluminescent components in which light can be stored and emitted in a controlled manner. Non-switching uses of ferroelectric materials includes capacitors, thermistors etc.

2.7 Magnetoelectric effect

The induction of magnetization by an electric field or of polarisation by a magnetic field is made possible by the coupling between magnetic and electric degrees of freedom in a composite material. ME effect in composite materials is a product tensor property [24, 25]. Thus the ME effect can be expressed as a result of the product of the magnetostrictive effect (magnetic/mechanical effect) in the magnetic phase and the piezoelectric effect (mechanical/electrical effect) in the piezoelectric phase [26]. The main mechanism behind the electrical and magnetic coupling is elastic interaction between the layers. For example, when a magnetic field is applied to a ME composite, the magnetic phase changes its shape magnetostrictively. The strain generated induces electric polarization in the piezoelectric phase. Hence the ME effect in such composite structures is an extrinsic property depending on the microstructure of composite and coupling interaction across magnetic-piezoelectric interfaces. For single phasic ME materials *i.e*., for multiferroic materials it is an intrinsic property.

The magnetoelectric effect in a single phasic material can be described in Landau theory by writing the free energy F of the system in terms of applied magnetic field (H) and electric field (E). By Einstein summation convention F can be represented as

$$F(E,H) = F_0 - P_i^s E_i - M_i^s H_i - \frac{1}{2}\varepsilon_0 \varepsilon_{ij} E_i E_j - \frac{1}{2}\mu_0 \mu_{ij} H_i H_j - \alpha_{ij} E_i H_j - \frac{\beta_{ijk}}{2} E_i H_j H_k - \frac{\gamma_{ijk}}{2} H_i E_j E_k - .... \quad (2.21)$$

Here ε and μ are the dielectric permittivity and magnetic permeability respectively. P_i^s and M_i^s are the time dependent electrical polarization and magnetization. Fourth and fifth terms represent the effect of electric and magnetic field on the electrical and magnetic behaviour respectively. The terms with the α_{ij} coefficients describe the linear magnetoelectric effect and the higher order magnetoelectric terms are given by β_{ijk} and γ_{ijk}. Differentiation of above equation with respect to electric and magnetic fields respectively leads to polarization and magnetization.

$$P(E,H) = -\frac{\partial F}{\partial E_i} = P_i^s + \varepsilon_0 \varepsilon_{ij} E_j + \alpha_{ij} H_j + \frac{1}{2}\beta_{ijk} H_j H_k + \gamma_{ijk} H_j E_k + ... \quad (2.22)$$

$$M(E,H) = -\frac{\partial F}{\partial H_i} = M_i^s + \mu_0 \mu_{ij} H_j + \alpha_{ij} E_j + \beta_{ijk} E_j H_k + \frac{1}{2}\gamma_{ijk} E_j E_k + ... \quad (2.23)$$

As the magnetoelectric effect is dominated to first order, only the linear term is considered.

$$M_i = \alpha_{ij} E_j \tag{2.24}$$

From the definitions of the electric and magnetic susceptibilities,

$$P_i = \chi_{e,ij} E_j \tag{2.25}$$

$$M_i = \chi_{m,ij} H_j \tag{2.26}$$

where χ_e and χ_m are the electric and magnetic susceptibilities.

By substituting the susceptibility terms in equation (2.24), we get

$$\alpha_{ij}^2 \leq \chi_{e,ii} \chi_{m,ii} \tag{2.27}$$

Hence, the magnetoelectric effect is expected to be large in composites of ferroelectric and ferromagnetic materials [27]. Large magnetoelectric effects were observed in composites derived from a system consisting of a ferroelectric piezoelectric and ferromagnetic magnetostrictive metal. These magnetoelectric materials play an important role in wide range of device applications like field sensing [28], current sensing [29-31], transformers [32, 33], amplifiers and gyrators [34, 35], tunable microwave devices [36, 37], spin wave signal processing [38] and antennas [39].

2.8 Heterostructure Geometry Considerations

By employing the concept of phase connectivity introduced by Newnham et al.,[25] the structures of a two-phase composite can be described using the notations 0-3, 2-2, 1-3, etc. Each number represents the connectivity of the respective phase. Here 0-3 type particulate composite means one-phase particles

(denoted by 0) embedded in the matrix of another phase (denoted by 3). So far, 0-3, 3-3, 2-2, and 1-3 type structured multiferroic ME composites of ferroelectric and magnetic phases have been developed by various groups.

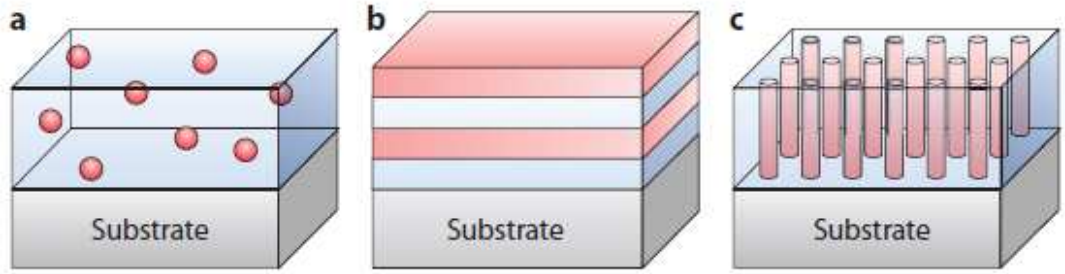

Fig.2.11 Schematic illustration of three kinds of ME composite nanostructures with common connectivity schemes: (a) 0-3 particulate nanocomposite films with magnetic particles (0) embedded in a ferroelectric film matrix (3); (b) 2-2 horizontal heterostructure with alternating ferroelectric (2) and magnetic (2) layers, or simply a ferroelectric (or magnetic) thin film grown on a magnetic (or ferroelectric) substrate; and (c) 1-3 vertical heterostructure with one-phase nanopillars (1) embedded in a matrix of another phase (3) [40]

2.8.1 Particulate nanocomposites

Particulate nanocomposites (quasi 0-3 type) consist of a magnetic phase which is generally distributed in a ferroelectric matrix (shown in figure 2.11(a)) [40]. These 3-phase composites can be easily fabricated by a conventional low temperature processing and can be molded to different forms such as thin sheets and shapes. One of the advantages of such structures is that they exhibit greatly improved mechanical properties [39]. For example, Wan et al. [41] obtained 0-3 polycrystalline composite films with CFO nanoparticles dispersed in PZT by employing sol-gel method.

2.8.2 Horizontal multilayer heterostructures

Horizontal multilayer heterostructures consist of alternative ferroelectric perovskite and magnetic spinel structures as shown in figure 2.11(b). These quasi 2-2 type laminate composites exhibit higher the ME effect in comparison with the quasi 0-3 type particulate composites. Also these nanostructures are easy to fabricate and the resistive ferroelectric layers in the structure block the current flow and hence prevents the possibility for leakage current [40]. One of the major drawbacks of such horizontal structures is the large in- plane constraint from the substrate clamping. This can be overcome by employing a buffer layer as the bottom electrode. The ease of processing and integration in to devices makes these 2-2 heterostructures as the most widely investigated nanocomposites [42-50].

2.8.3 Vertical nanostructures

In addition to 0-3 and 2-2 heterostructures another important configuration is 1-3 vertical nanostructure. In such a nanostructure, one of the ferroic (ferroelectric/ferromagnetic) phases is developed as nanopillars in the other ferroic matrix (ferromagnetic/ ferroelectric). Such 1-3 vertical heterostructures can be prepared by a dice and fill process. For example, a PZT bulk is diced according to the designed volume fraction of PZT rods to get PZT rod array, and then the gap of the PZT rod array is filled with a mixture of Terfenol-D particles and epoxy. As the epoxy hardens, the pseudo-1-3-type multiferroic composite is obtained [39].

2.9 Electric field control of magnetism in magnetoelectric thin films

Other than the magnetic field control of electric polarization, the converse ME effect (the electric field control of magnetization) is of equal importance. A

main challenge faced in the fields of spintronics and multiferroics is controlling magnetic anisotropy or the magnetization direction in a ferromagnetic material directly by applying an electric field rather than current. Converse ME effect can be realized in multiferroic ME composite systems by ME coupling either through a strain-induced ME effect across the interface [51-56], exchange bias [57-59], or a charge-driven ME effect [60-63].

2.9.1 Strain mediated ME effect

In the converse piezoelectric effect an external electric field results in a change in the shape of the ferroelectric phase in multiferroic ME composite nanostructures as shown in figure 2.12.

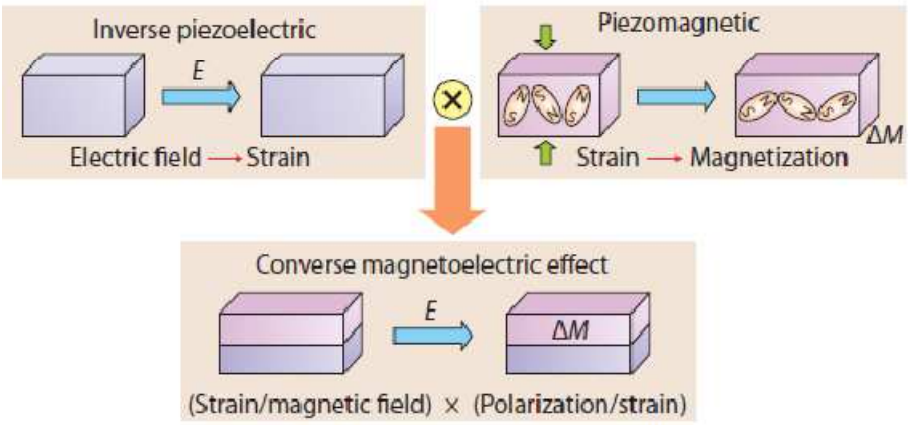

Fig. 2.12 Schematic illustration of strain-mediated ME effect in a composite system consisting of a magnetic layer (purple) and ferroelectric layer (pink). An out-of-plane electric field (E) induces strain in the ferroelectric component due to the inverse piezoelectric effect, which is mechanically transferred to the magnetic component, inducing a magnetization change (ΔM) or domain reorientation through the piezomagnetic effect [40]

The strain induced in the ferroelectric phase passes on to the magnetic phase which in turn alters the magnetic anisotropy of the magnetic phase via

magnetostriction. Thus strain-mediated ME coupling can be employed to achieve electric-field control of the magnetic behavior of magnetic nanostructures [52-56, 64].

2.9.2 Exchange bias mediated ME effect

Electric field control of the magnetic properties in the ferromagnetic films can be achieved by employing the exchange bias resulting from the exchange coupling between the uncompensated interfacial spins of the antiferromagnet and the spins of the ferromagnetic layer [65, 66]. Wu et al. in 2010 observed a reversible electric-voltage control of exchange bias in a multiferroic BFO/LSMO epitaxial heterostructure by switching the ferroelectric polarization of BFO [67]. The induced interface magnetism in a few nanometers of the BFO layer as a consequence of an electronic orbital reconstruction occurring at the BFO/LSMO interface induces the exchange bias effect in such a structure [68].

2.9.3 Charge mediated ME effect

The spin dependent screening of the electric field may result in the accumulation of charge (e.g. spin-polarized electrons or holes) at the interface, which in turn produces a change in the interface magnetization in horizontal heterostructures containing ultrathin ferromagnetic films [40]. The electric field induced modification of magnetocrystalline anisotropy can be attributed to a change in the number of unpaired *d* electrons under the applied electric field. The charge-mediated magnetoelectric coupling in multiferroic nanostructures takes advantage of the sensitivity of a strongly correlated ultrathin magnetic film to competing electronic ground states.

2.10 Applications

ME composites are promising materials for technological applications such as magnetic field sensors, memory devices, spintronic devices, and electrically tunable microwave devices. As the input magnetic field has two components, a dc bias and an ac probe, either of the two can be detected by applying the other component. Hence the ME composite can be used as a tool for detecting ac or dc fields. At the resonance frequency bulk/nanostructured ME composite can be used as a transducer that converts the microwave magnetic field into a microwave electric field. The shift in the resonance frequency in a static magnetic or electric bias field makes the composite materials an ideal component for electrically tunable microwave applications such as filters, oscillators, and phase shifters. The hysteretic nature of the ME effect of such composites can be utilized in applications like memory devices.

2.10.1 Magnetic memories

Commercial magnetic medium storage devices like floppy disk and hard disk uses a magnetic field to write the data with the two magnetization states ± M of magnetic recording media, and a MR read head to sense the spatial variations of these magnetization states [69]. Hard magnetic materials with high coercivity were used for data storage in magnetic memories to maintain the magnetization states. But the high coercivity results in a high writing magnetic field for the magnetization reversal process. Thus the high writing magnetic field driven by currents require high power consumption associated with low writing speed restricted by the writing head movement. Hence the improvements of the read-write speeds [70] and information security [71] are highly desirable in data

storage technology. Converse ME effect can be used to achieve this goal in an easier way as electrically assisted magnetization reversal is possible in such ME nanostructures.

2.10.2 Magnetic sensors

The working principle of magnetic sensing in the ME composites is magnetoelectric coupling. In the presence of a magnetic field, the magnetic phase in the composite strains which in turn produce a proportional change in the piezoelectric phase. Thus ME composites with high ME coefficients can be employed using highly sensitive magnetic field sensors. Also they can be used as a magnetic probe for detection of both ac and dc fields.

2.10.3 Electrically tunable microwave devices

ME composites represents a promising class of materials in microwave devices. Magnetic bias fields have been used for the tuning of magnetization for microwave magnetic devices. The possibility of electric field control of magnetization (converse magnetoelectric effect) has resulted in novel, electrostatically tunable microwave magnetic devices such as filters, resonators and phase shifters based on the ME composite films.

References:

1. R.M. Bozorth, *Ferromagnetism* Van Nostrand, Princeton, (1968)
2. J. Friedel, *Nuovo Cimento* 7, (1958) 287
3. M.T. Johnson, P J H Bloemen, F J A den Broeder, J J de Vries, *Rep. Prog. Phys*. 59, (1996) 1409
4. Nicola A. Spaldin, *Magnetic materials: fundamentals and device applications*, Cambridge University Press (2003)
5. Mathias Getzlaff*, Fundamentals of Magnetism*, Springer, (2008)
6. B.D. Cullity, *Introduction to Magnetic Materials*, Addison-Wesley, Massachusetts (1972)
7. David Jiles, *Introduction to Magnetism and Magnetic Materials*, Chapman and Hall, (1991)
8. B. D. Cullity, C. D. Graham, *Introduction to magnetic materials*, John Wiley & Sons (2009)
9. Chikazumi S, *Physics of Ferromagnetism*, Oxford Science Publications (1997)
10. Wolfgang Bolse, *Surf. and Coat. Tech*. 158 (2002) 1
11. F. Seitz, J. S. Koehler, *Solid State Phys*. 2 (1956) 305
12. Z. G. Wang, Ch. Dufour, E. Paumier, M. Toulemonde, *J. Phys.: Condens. Matter* 6 (1994) 6733
13. G. Schiwietz, E. Luderee, G. Xiao, P. L. Grande, *Nucl. Instrum. Meth. B* 175 (2001) 1
14. R. L. Fleisher, P. B. Price, R. M. Walker, *Nuclear Tracks in Solids*, University of California Press, (1975)

15. A. Akkermann, J. Levinson, D. Ilberg, Y. Lifshitz, Editor - R. Baragiola, *Ionisation of Solids by Heavy Particles, NATO Advanced Study Institutes Series* 306, Plenum Press, New York, (1992)
16. I.P. Jain, Garima Agarwal, *Surf. Sci. Rep*. 66 (2011) 77
17. S.O. Kucheyev, H. Timmers, J. Zou, J.S. Williams, C. Jagadish, *J. Appl. Phys*. 95 (2004) 5360
18. E.M. Bringa, R.E. Johnson, *Phys. Rev. Lett*. 88 (2002) 165501
19. A. Donlop, G. Jaskierowicz, G. Rizza, M. Kopcewicz, *Phys. Rev. Lett*. 90 (2003) 15503
20. G D Raj, *Solid State Physics*, Amrnol Publication, New Delhi (1995)
21. M. E. Lines, A. M. Glass, *Principles and Applications of Ferroelectrics and Related Materials*, Clarendon, Oxford (1979)
22. F. Jona, G. Shirane, *Ferroelectric Crystals*, Pergamon, New York (1962)
23. B A Strukov, A. P. Levanyuk, *Ferroelectric Phenomena in Crystals: Physical Foundations,* Springer, Berlin (1998)
24. J. van Suchtelen, *Philips Res. Rep*. 27, (1972) 28
25. R. E. Newnham, D. P. Skinner, L. E. Cross, *Mater. Res. Bull*. 13, (1978) 525
26. C. W. Nan, *Phys. Rev. B* 50, (1994) 6082
27. Nicola A. Spaldin, R. Ramesh, *MRS Bull.,* 33(11), (2008) 1047
28. J.Y. Zhai, Z.P. Xing, S.X. Dong, J.F. Li, D.Viehland, *Appl. Phys. Lett*., 88(6), (2006)
29. S.X. Dong, J.F. Li, D. Viehland, *Appl. Phys. Lett*., 85(12), (2004) 2307
30. S.X.Dong, J.F.Li, D. Viehland, *J. Appl. Phys*., 96(6), (2004) 3382

31. S.X. Dong, J.G. Bai, J.Y. Zhai, J.F. Li, G.Q. Lu, D. Viehland, S.J. Zhang, T.R Shrout, *Appl. Phys. Lett*., 86(18), (2005)
32. S X Dong, J.F. Li, D. Viehland, J Cheng, L.E. Cross, *Appl. Phys. Lett*. 85(16), (2004) 3534
33. S X Dong, J.F. Li, D. Viehland, *Appl. Phys. Lett*., 84(21), (2004) 4188
34. S X Dong, J.Y Zhai, J. F. Li, D. Viehland, M. I. Bichurin, *Appl. Phys. Lett*., 89 (2006) 24
35. J.Y Zhai, J.F Li, S.X Dong, D. Viehland, M. I. Bichurin, *J. Appl. Phys*. 100(12), (2006)
36. Z. Huang, *J. Appl. Phys.,* 100(11), (2006)
37. M.I. Bichurin, I.A. Kornev, V.M Petrov, A.S Tatarenko, Y.V Kiliba, G Srinivasan, *Phys. Rev. B,* 64(9), (2001)
38. R.R.Birss, Shrubsal.R.G, *Philosophical Magazine*, 15(136), (1967) 687
39. C.W Nan, M. I. Bichurin, S.X Dong, D. Viehland, G. Srinivasan, *J. Appl. Phys*. 103(3), (2008)
40. Y Wang, J Hu, Y Lin, C-W Nan, *NPG Asia mater*., Vol. 2 April 2010
41. J. G. Wan, X. W. Wang, Y. J. Wu, M. Zeng, Y. Wang, H. Jiang, W. Q. Zhou, G. H. Wang, J.-M. Liu, *Appl. Phys. Lett*. 86, (2005) 122501
42. C. Deng, Y. Zhang, J. Ma, Y. Lin, C.-W. Nan, *Acta Mater*. 56, (2008) 405
43. Y. Zhang, C. Deng, J. Ma, Y. Lin, C.-W. Nan, *Appl. Phys. Lett*. 92, (2008) 062911
44. S T Zhang, Y Zhang, Z L Luo, M H Lu, Z B Gu, Y F Chen, *Appl. Surf. Sci*. 255, (2009) 5092
45. Z. Li, Y. Wang, Y. Lin, C.-W. Nan, *Phys. Rev. B* 79, (2009) 180406R

46. S. Ryu, J. H. Park, H. M. Jang, *Appl. Phys. Lett*. 91, (2007) 142910
47. M. Ziese, A. Bollero, I. Panagiotopoulos, N. Moutis, *Appl. Phys. Lett*. 88, (2006) 212502
48. W. Eerenstein, M. Wiora, J. L. Prieto, J. F. Scott, N. D. Mathur, *Nature Mater*. 6, (2007) 48
49. C. Thiele, K. Dörr, O. Bilani, J. Rödel, L. Schultz, *Phys. Rev. B* 75, (2007) 054408
50. J. Wang, Y. Zhang, J. Ma, Y. Lin, C.-W. Nan, *J. Appl. Phys*. 104, (2008) 014101
51. W. Eerenstein, M. Wiora, J. L. Prieto, J. F. Scott, N. D. Mathur, *Nature Mater*. 6, (2007) 348
52. F. Zavaliche, H. Zheng, L. Mohaddes-Ardabili, S. Y. Yang, Q. Zhan, P. Shafer, E. Reilly, R. Chopdekar, Y. Jia, P. Wright, D. G. Schlom, Y. Suzuki, and R. Ramesh, *Nano Lett*. 5, (2005) 1793
53. H Zheng, Q Zhan, F Zavaliche, M Sherburne, F Straub, M P. Cruz, L-Q Chen, U Dahmen, R. Ramesh, *Nano Lett*. 6, (2006) 1401
54. M Liu, O Obi, J Lou, Y Chen, Z Cai, S Stoute, M Espanol, M Lew, X Situ, K S. Ziemer, V G. Harris, N X Sun, *Adv. Func. Mater*. 19, (2009) 1826
55. J. J. Yang, Y. G. Zhao, H. F. Tian, L. B. Luo, H. Y. Zhang, Y. J. He and H. S. Luo, *Appl. Phys. Lett*. 94, (2009) 212504
56. S Sahoo, S Polisetty, C G Duan, S S. Jaswal, E Y. Tsymbal, C Binek, *Phys. Rev. B* 76, (2007) 092108

57. Y H Chu, L W. Martin, M Holcomb, M Gajek, S J Han, Q He, N Balke, C H Yang, D Lee, W Hu, Q Zhan, P L Yang, A F Rodríguez, A Scholl, S X. Wang, R. Ramesh, *Nature Mater.* 7, (2008) 478
58. H. Béa, M. Bibes, M. Sirena, G. Herranz, K. Bouzehouane, E. Jacquet, S. Fusil, P. Paruch, M. Dawber, J.-P. Contour, A. Barthélémy, *Appl. Phys. Lett*. 88, (2006) 062502
59. H. Béa, M. Bibes, F. Ott, B. Dupé, X.-H. Zhu, S. Petit, S. Fusil, C. Deranlot, K. Bouzehouane, A. Barthélémy, *Phys. Rev. Lett*. 100, (2008) 017204
60. M Weisheit, S Fähler, A Marty, Y Souche, C Poinsignon, D Givord, *Science* 315, (2007) 349
61. T. Maruyama, Y. Shiota, T. Nozaki, K. Ohta, N. Toda, M. Mizuguchi, A. A. Tulapurkar, T. Shinjo, M. Shiraishi, S. Mizukami, Y. Ando, Y. Suzuki, *Nature Nanotech*. 4, (2009) 158
62. G. A. Prinz, *Science* 282, (1998) 1660
63. C. Chappert, A. Fert, F. N. Van Dau, *Nat. Mater*. 6, (2007) 813
64. H J. A. Molegraaf, J Hoffman, C A. F. Vaz, S Gariglio, D van der Marel, C H. Ahn, J M Triscone, *Adv. Mater*. 21, (2009) 3470
65. A. Brandlmaier, S. Geprägs, M. Weiler, A. Boger, M. Opel, H. Huebl, C. Bihler, M. S. Brandt, B. Botters, D. Grundler, R. Gross, and S. T. B. Goennenwein, *Phys. Rev. B* 77, (2008) 104445
66. N. Mathur, *Nature* 454, (2008) 591
67. J Ma, J Hu, Z Li, C W Nan, *Adv. Mater*. 23, (2011) 1062
68. S. M. Wu, S. A. Cybart, P. Yu, M. D. Rossell, J. X. Zhang, R. Ramesh, R. C. Dynes, *Nat. Mater*. 9, (2010) 756

69. P. Yu, J. S. Lee, S. Okamoto, M. D. Rossell, M. Huijben, C. H. Yang, Q. He, J. X. Zhang, S. Y. Yang, M. J. Lee, Q. M. Ramasse, R. Erni, Y. H. Chu, D. A. Arena, C. C. Kao, L. W. Martin, R. Ramesh, *Phys. Rev. Lett*. 105, (2010) 027201
70. S. Parkin, X. Jiang, C. Kaiser, A. Panchula, K. Roche, M. Samant, *Proc. of IEEE* 91, (2003) 661
71. D. A. Thompson, J. S. Best, *IBM J. Res. Dev*. 44, (2000) 311

CHAPTER 3

EXPERIMENTAL TECHNIQUES

This chapter discusses the experimental techniques employed for sample preparation and it also deals with the different characterization tools employed at various stages. A brief description about the methods utilized to fabricate thin film structures is also provided. Since swift heavy ions are used to modify the material properties, this chapter also looks at the experiment conducted using swift heavy ions. Experiments involving electron microscopy and atomic force microscopy are also discussed briefly in this chapter. Different characterization tools used for characterizing ferromagnetic and ferroelectric properties are also dealt with. Since magnetoelectric coupling form a part of the major theme of this thesis, a brief description about the evaluation of magnetoelectric coupling is provided in this chapter.

3.1 Deposition Techniques

a. Physical Vapour Deposition

Physical Vapor Deposition (PVD) is a collective set of processes used to deposit thin films typically in the range of few nanometers to several micrometers. Here films are formed by atoms which are directly transported from source to the substrate through gas phase [1]. PVD techniques can be divided into two categories namely evaporation (thermal evaporation & E-beam evaporation) and sputtering (DC, DC magnetron &RF sputtering). These PVD processes are environment friendly vacuum deposition techniques and consist of three steps.

- Vaporization of the material from a solid source assisted by high temperature vacuum or gaseous plasma.
- Transportation of the vapor in vacuum or partial vacuum to the substrate surface.

- Condensation onto the substrate to generate thin films.

Among different PVD techniques thermal evaporation is a simple and inexpensive method for obtaining good quality thin films of materials with low and moderate melting point. This technique relies on vaporizing a source material using appropriate methods in vacuum. The starting compound is vaporized and the material is deposited onto a desired substrate through a condensation mechanism [2]. A typical vacuum coating system consists of two parts-vacuum pumping and the deposition set-up as shown in figure 3.1. Resistive evaporation is a commonly used vacuum deposition technique in which electrical energy is used to heat a filament which in turn heats a deposition material to the point of evaporation. The evaporation is done in high vacuum to eliminate contamination in the deposited film. An oil diffusion pump along with a rotary pump can produce a typical vapor pressure of 10^{-5} mbar inside the chamber. A boat or helical coil containing the starting material acts as a resistive element between two electrodes for the passage of a large d.c current. High melting point metals, like molybdenum or tungsten are used as boat/filament materials. The process of deposition starts, by creating vacuum in the deposition chamber, usually of the order of 10^{-5} mbar or less.

The thermal evaporation deposition technique consists in heating the resistive element until evaporation of the material to be deposited starts. The material vapor finally condenses in the form of thin film on the cold substrate surface and on the vacuum chamber walls. Because of the low pressure inside the vacuum chamber, the mean free path of vapor atoms is the same order of vacuum chamber dimensions, and hence these particles travel in straight lines from the

evaporation source towards the substrate. This originates 'shadowing' phenomena, especially in those regions not directly accessible from the evaporation source.

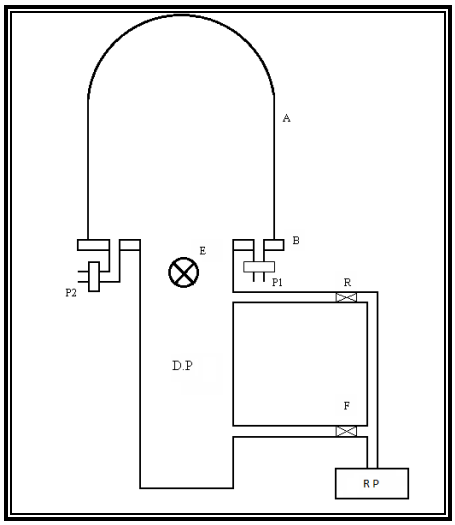

A- VACUUM CHAMBER P1- PIRANI GAUGE HEAD
B- BASE PLATE P2- PENNING GAUGE HEAD
E- BAFFLE VALVE RP- ROTARY PUMP
R- ROUGHING VALVE DP- DIFFUSION PUMP
F- BACKING VALVE

Fig. 3.1 Schematic of a typical vacuum coating unit

b. Spin Coating

Spin coating is a simple technique used to deposit uniform thin films on flat substrates. The substrates to be coated is held by a rotatable fixture (often vacuum is used) and a small amount of coating material is dispensed on the center of the substrate, which is either spinning at low speed or not spinning at all. The substrate is then rotated at high speed in order to spread the coating material by centrifugal force.

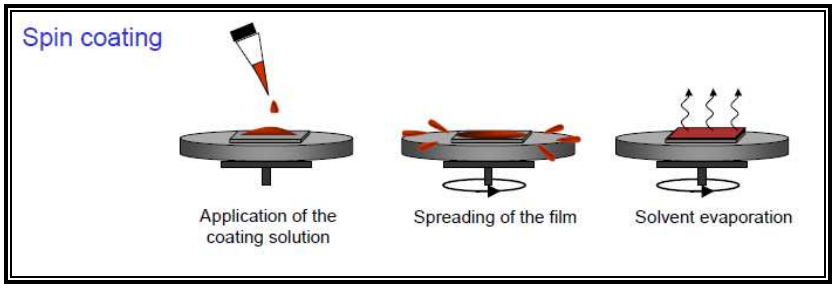

Fig. 3.2 Different steps involved in spin coating technique

Here the rotational accelerations are exactly balanced by the viscous drag felt within the solution. Factors such as rotational speed and acceleration contribute to the properties of coated films. A machine used for spin coating is called a spin coater [3]. Different processes involved in spin coating technique are shown in figure 3.2.

- Deposition of the coating fluid onto the substrate by pouring the coating solution or by spraying it onto the surface
- Acceleration of the substrate to its final required rotation speed
- Spinning of the substrate at a constant rate - fluid viscous forces dominate the fluid thinning behavior
- Spinning of the substrate at a constant rate - solvent evaporation dominates the coating thinning behavior

Spin coating technique is widely used in semiconductor industry and photolithography.

3.2 Swift Heavy Ion Irradiation by a Pelletron Accelerator

Swift heavy ion (SHI) irradiation is a versatile technique for the modification of the properties of films, foils and bulk solids. Swift heavy ions penetrate deep in to the materials and produces disordered zones along its trajectory. The changes produced in the material while irradiation processes can

be understood by analyzing the resultant damage such as size, shape and structure of defects. We have made use of the SHI from 15 UD Pelletron accelerator facility at the Inter University Accelerator Centre (IUAC), New Delhi, India for the ion irradiation studies carried out in the present study.

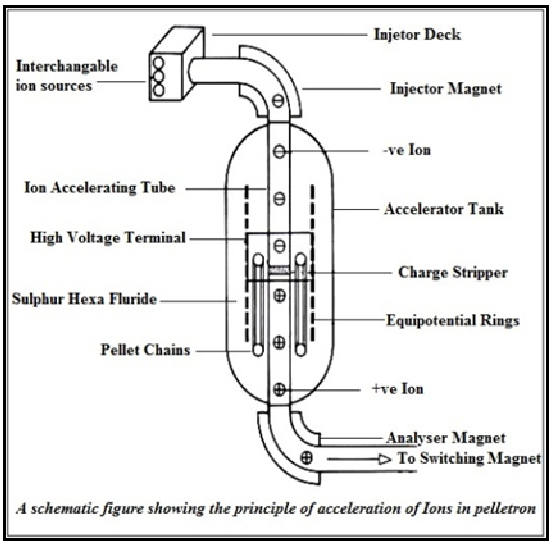

Fig. 3.3 Schematic representation of Pelletron unit (Adapted from IUAC website www.iuac.res.in)

A schematic representation of the 15UD Pelletron accelerator is shown in figure 3.3. This Pelletron is a heavy ion tandem type of electrostatic accelerator. Negative ions are produced and pre-accelerated to ~300KeV in an ion source - SNICS (Source of Negative Ions by Cesium Sputtering)- and are injected in to strong electric field inside an accelerator tank filled with SF_6 insulating gas. At the centre of the tank there is a terminal shell, which is maintained at a high voltage (~15 MV).The negative ions on traversing through the accelerating tubes from the column top of the tank to the positive terminal gets accelerated. On reaching the terminal, they pass through a stripper, which removes some electrons from the

negative ions, thus transforming the negative ions into positive ions. These positive ions are then repelled away from the positively charged terminal and are accelerated to ground potential to the bottom of the tank. Here, same terminal potential is used twice to accelerate the ions. The analyzing magnet bends the ions into horizontal plane which also select a particular beam of ion. The switching magnet diverts the high energy ion beams into various beam lines for the different experimental areas of the beam hall. The entire machine is computer controlled and is operated from the control room. These accelerated ions are fed into the materials science beam hall, where the samples are loaded in the sample holder, made of thick block of copper. The pressure in the chamber is maintained at $1x10^{-6}$ Torr during irradiation.

3.3 Thickness Profiler

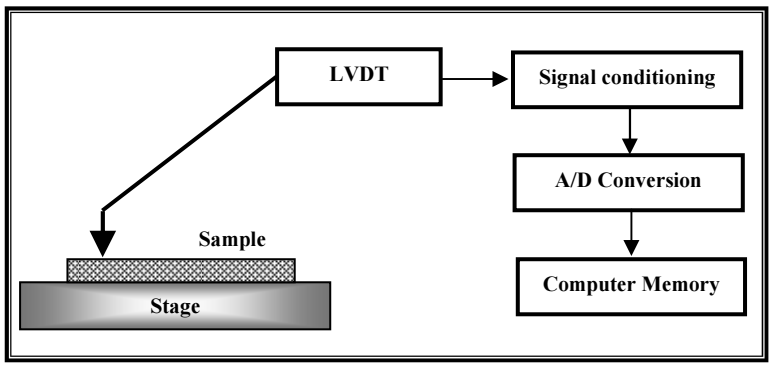

Fig. 3.4 Schematic representation of thickness profiler set up

The film thickness is measured using Dektak 6M Stylus Profiler. The block diagram of the instrument is shown in figure 3.4. Stylus profilers are versatile measurement tools for analyzing the surface topography. Primarily they can be used to measure film thickness by scanning step heights and trench depths. Surface roughness as well as surface planarity also can be measured using this set

up. This is a surface contact measurement technique where a very low force stylus is dragged across a surface.

A diamond stylus is moved vertically into in contact with the sample and then moved laterally across the sample for a specified distance and specified contact force. This stylus is mounted on an arm coupled to a linear variable differential transformer (LVDT). The output voltage changes from plus to minus as a function of core displacement corresponding to the mechanical changes that occur while the stylus moves up or down over the surface. The varying signal is then digitized and recorded to represent the surface profile of the sample.

3.4 Structural characterization techniques

3.4.1 Powder X-Ray Diffraction

X-ray diffraction (XRD) technique is a fundamental tool for material characterization. In general, a crystal diffracts an X-ray beam passing through it depending on the X-ray wavelength, the crystal orientation and structure of the crystal. Powder X-ray diffraction generally employs the conventional θ–2θ (or Bragg- Brentano) reflection geometry in which the incidence angle equals the angle of the diffracted beam with respect to the sample surface (shown in figure 3.5) [4].

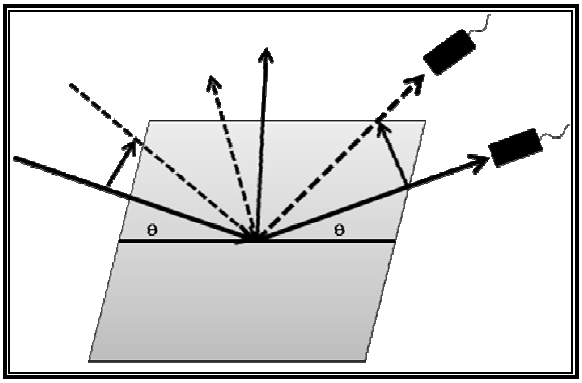

Fig. 3.5 Schematic of symmetric θ–2θ geometry

Here, a certain wavelength of radiation will constructively interfere when partially reflected between atomic planes. This will produce a path difference equal to an integral number of wavelengths. According to Bragg law,

$$2d\sin\theta = n\lambda \tag{3.1}$$

where n is an integer, λ is the wavelength of the radiation, d is the spacing between atomic planes and θ is the diffraction angle. Lattice parameter can be computed by employing the relation,

$$d_{hkl} = \frac{1}{\sqrt{\frac{h^2}{a^2} + \frac{k^2}{b^2} + \frac{l^2}{c^2}}} \tag{3.2}$$

Where a,b,c are the lattice parameters.

For cubic symmetry, a=b=c

$$d_{hkl} = \frac{a}{\sqrt{h^2 + k^2 + l^2}} \tag{3.3}$$

Sample identification can be easily done by comparing the experimental pattern to that in the International Centre for Diffraction Data (ICDD) file. The random orientation of crystals in the polycrystalline samples and thin films cause

broadening of the diffraction patterns. This effect becomes more pronounced when the crystallite size is of the order of nanometers.

In the case of nanoscale structures crystallite size can be calculated using the Scherrer formula given by

$$D = \frac{0.9\lambda}{\beta \cos\theta} \tag{3.4}$$

where D is the crystallite size, λ is the wavelength of the X-ray beam, β is the angular width (in radians) which is equal to the FWHM (Full Width at Half Maximum).

3.4.2 Glancing Angle X-Ray Diffraction

X-rays with large incident angle will go through a few to several hundred micrometers inside the sample under investigation depending on its radiation density. When it comes to thin film analysis, the beam penetration depth may be much greater than the sample thickness. Hence conventional XRD is not suitable for a detailed study of thin film specimens. Glancing/grazing angle configurations have been developed to overcome such limitations. In glancing angle X-ray diffraction (GAXRD) technique, the Bragg-Brentano geometry is modified to an asymmetric configuration which allows access to small depths in the sample by varying the incident angle. Here a parallel monochromatic X-ray beam incident on the sample surface at a fixed, low glancing angle, γ (typically 1^{O} to 3^{O}) and the diffraction profile is recorded by detector-scan only. Due to the para-focusing and large diffracting volume, this method provides good sensitivity for thin films. As X-ray path length in the film is proportional to [1/ sin (γ)], smaller the glancing angle, greater the path length in the film. Hence increase in the path length of the

incident X-ray beam through the film increases the intensity from the film and decreases the diffracted intensity from the substrate.

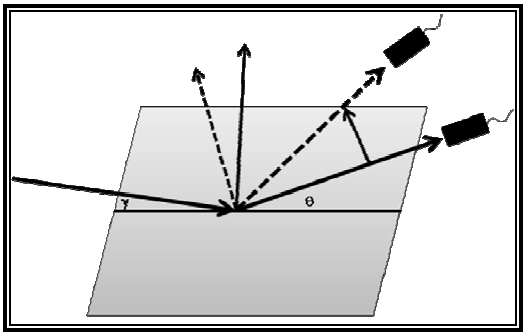

Fig. 3.6 Schematic diagram of asymmtric glancing angle XRD geometry

GAXRD technique can be used to obtain valuable information regarding the thickness and phase crystallography of the sample [5-7], the change of its composition with depth [8], and its microstructure (stress, preferred orientation, etc.)[9].

3.4.3 Scanning Electron Microscopy

The scanning electron microscopy (SEM) is one of the most versatile techniques available for the examination and analysis of the chemical composition characterizations and microstructure morphology. The naked eye can distinguish objects subtending about 1/60° visual angle, corresponding to a resolution of ~0.1 mm (at the optimal viewing distance of 25 cm) whereas optical microscopy has the limit of resolution of ~2,000 Å by enlarging the visual angle through optical lens. Since the discovery that electrons can be deflected by the magnetic field [10], electron microscopy has been developed by replacing the light source with high energy electron beam. The minimum distances by which two structures can be separated and still appear as two distinct objects and is defined as the limit of

resolution. Ernst Abbe [*10*] demonstrated that the limit of resolution depends on the wavelength of the illumination source. At a particular wavelength, when resolution goes above this limit, the magnified image blurs.

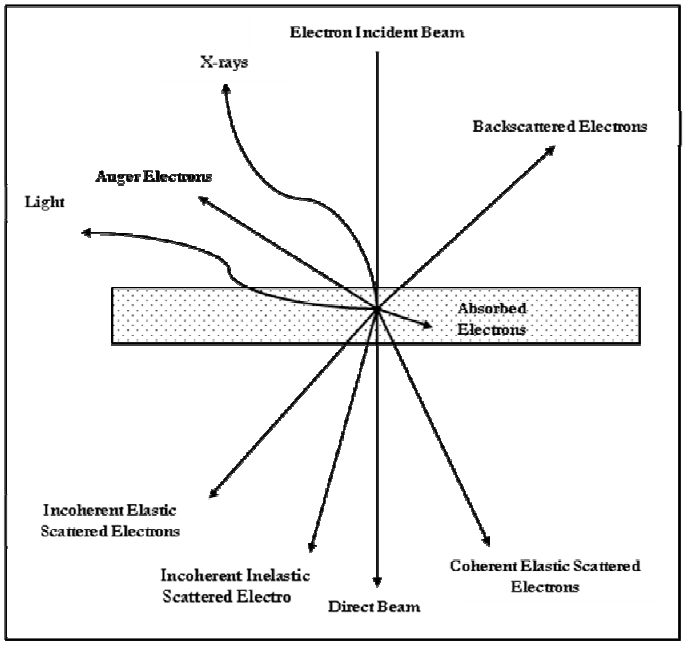

Fig. 3.7 Interactions between electrons and matter

When electrons are accelerated to high energy levels and focused on to a material, they scatter or backscatter elastically or inelastically in different directions. These inelastic interactions between matter and electron produce different types of signals namely secondary electrons, Auger electrons, X-rays, light and lattice vibrations (figure 3.7).

In a typical SEM (schematic shown in figure 3.8), an electron beam is thermionically emitted from an electron gun which acts as the source. The electron energy beam has an energy ranging from 0.2keV to 40keV. This electron beam is focused by one or two condenser lenses and is passed through pair of

scanning coils or deflection plates in the electron column. Scanning coils are used to deflect the electron beam so that it can raster scan on the sample surface along x- or y-axis.

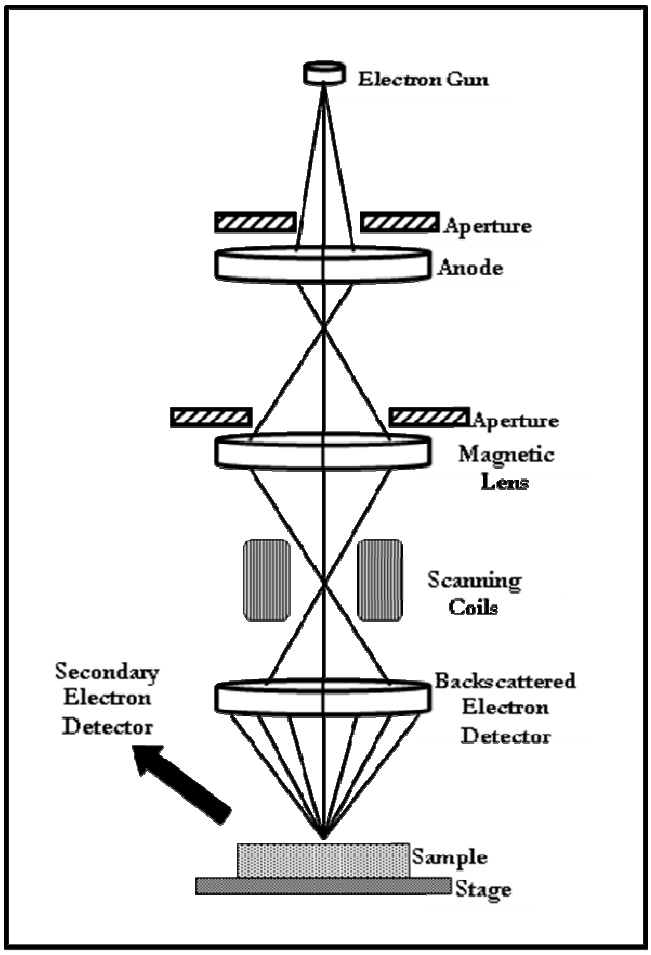

Fig. 3.8 Schematic of scanning electron microscope

When the primary electron beam interacts with the sample, it loses energy by repeated random scattering and absorption. The energy exchange between the

incident electron and sample takes place which in turn results in the reflection of high energy electrons by elastic scattering and emission of secondary electrons by inelastic scattering. Specialized detectors may be used for the detection of such signals. As the secondary electrons have low energy (typically around 3-5eV), they can only escape from a region within a few nanometers of the sample surface. Hence the secondary electrons precisely mark the position of the beam and give surface texture and roughness with a better resolution. A secondary electron beam can resolve the surface features down to the order of around 10nm. The detection of backscattered electrons shed light onto the sample composition. One or more apertures are employed in the SEM designs to exclude scattered electrons and are used to control the spherical aberrations in the final lens [11].

3.4.4 Transmission Electron Microscopy

Transmission electron microscopy (TEM) is a unique technique which can provide a real space image on the atomic distribution in the nanomaterial and on its surface. Nowadays TEM is a versatile tool that gives not only atomic resolution lattice images but also chemical information at a spatial resolution of 1nm or better thereby allowing direct identification of the structure and chemistry of nanomaterials.

One of the greatest advantages of TEM is its excellent horizontal resolution and it depends on the wavelength of the radiation employed, i.e., the smaller the wavelength, the greater the resolution. In TEM, the incident radiation is a beam of electrons that has a wavelength of the form

$$\lambda(nm) \cong \sqrt{\frac{1.5}{V}} \qquad (3.5)$$

where V is the acceleration voltage (in volts) applied to incident electrons. A simplified scheme of TEM is shown in figure 3.9.

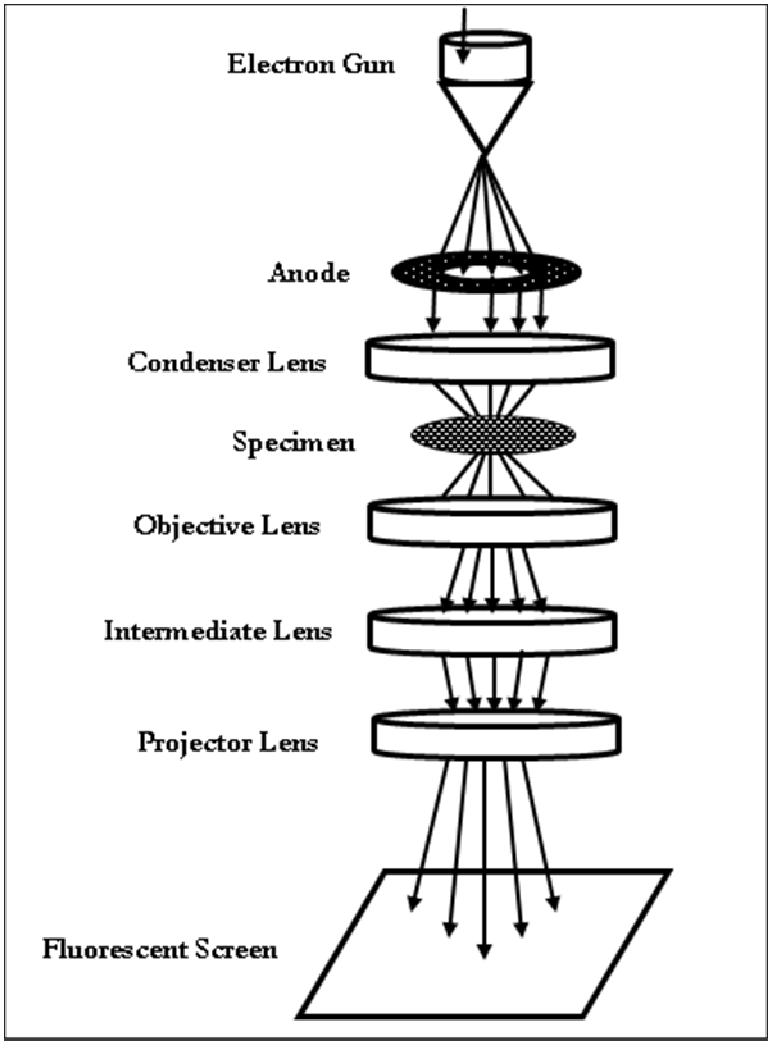

Fig.3.9 Schematic of transmission electron microscope

The basic TEM instrument consists of an electron gun which may be a tungsten filament or a lanthanum hexaboride (LaB_6) source [12] and is connected

to a high voltage source (typically~ 100-300kV). The focused electron beam is incident on a thin sample. A series of magnetic lenses are used for focusing the electron beam at and below the sample position. The condenser lenses of the TEM allow for the formation of the electron beam to the desired size and location for later interaction with the sample [13]. Here the use of magnetic fields allows the formation of a magnetic lens of variable focusing power. The projector lenses are used to expand the electron beam onto the fluorescent screen or other imaging devices. The objective lens decides the limit of image resolution. The intermediate lenses and projection lenses constitute the magnification system and it gives a magnification up to 1.5 million. A charge coupled device (CCD) can be used as the digital data recording system.

One of the major advantages of TEM is that it offers high magnification ranging from 50 to 10^6 and another is its ability to provide both image (in real space) and diffraction (reciprocal space) information from a single sample.

The magnification or resolution of TEM is given by the equation

$$L = \frac{h}{\sqrt{2mqV}} \tag{3.6}$$

where m and q are the electron mass and charge, h is the Planck's constant and V is the potential difference through which the electrons are accelerated.

High Resolution Transmission Electron Microscopy (HRTEM) is an important tool for high-magnification studies of nanomaterials. High resolution makes it suitable for imaging nanomaterials on the atomic scale. Structural information at better than 0.2 nm spatial resolution can be obtained using HRTEM [14]. In HRTEM measurements, specimens need to be relatively beam insensitive as high magnification imaging requires a high electron energy. HRTEM uses a

large diameter objective lens that admits not only the transmitted beam, but at least one diffraction beam as well. These beams passed by the objective aperture are then made to recombine in the image forming process in such a way that their amplitudes and phases are preserved. Here at high magnification, it is possible to see contrast in the image in the form of periodic fringes and these fringes represent direct resolution of Bragg diffracting planes.

3.5 Composition Analysis

3.5.1 X-Ray Photoelectron Spectroscopy

X-Ray photoelectron spectroscopy (XPS) also known as Electron Spectroscopy for Chemical Analysis (ESCA) is a chemical surface analysis method. XPS is a quantitative spectroscopic technique that measures the elemental composition, empirical formula, chemical state and electronic state of the elements that exist on the surface of the specimen (up to 10nm). The basic principle behind X-Ray photoelectron spectroscopy is the photoelectric effect. In XPS, X-rays bombard a sample creating ionized atoms and ejecting free electrons. These ejected free electrons have a kinetic energy (E_K) given by

$$E_K = h\nu - E_B - \phi \tag{3.7}$$

where E_B is the binding energy of core level and ϕ is the work function.

By analyzing the kinetic energy of these photoelectrons one can determine the corresponding binding energies of the photoelectrons and the energies of the electronic orbitals.

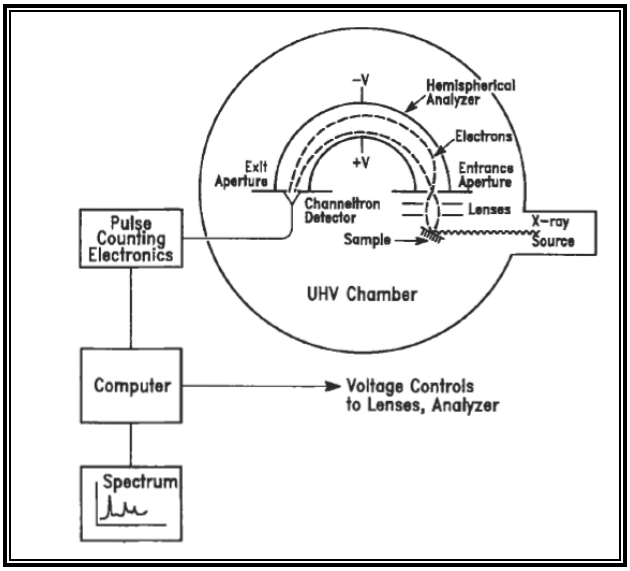

Fig. 3.10 Schematic of a XPS instrument [15]

A basic structure of XPS instrument is shown in figure 3.10. X-rays having a specific energy are used to excite the electronic states of atoms on the surface of the sample. The emitted electrons are energy filtered via a hemispherical analyzer (HSA) before the intensity for a defined energy is recorded by a detector. As the core level electrons are quantized, the resulting energy spectra show resonance peak characteristics of the electronic structure for atoms at the sample surface. An electron energy analyzer determines the binding energy of the photoelectrons and from the bonding energy and intensity of the photoelectric peak, the elemental identity, chemical state and quantity of element can be determined. Although the X-rays may penetrate deep into the sample, the escape depth of the ejected electrons is limited. Such electrons undergo an energy loss event and hence contribute to the background signal rather than well defined primary photoelectric peaks. Changes in the chemical environment or oxidation

state of an atom can cause corresponding changes in the energies of the electrons that are ejected and analyzed. By measuring these shifts, it is possible to accurately assign the chemical environment of a given element.

3.5.2 Energy Dispersive X-Ray Spectroscopy

Energy dispersive X-ray spectroscopy (EDAX) is an analytical technique used for the elemental analysis or chemical characterization of a material under TEM/SEM. The X-rays produced as a result of the electron beam interactions with the sample is detected in this method. As the energy of the X-rays is characteristic of the difference in energy between the two shells, and of the atomic structure of the element from which they were emitted, this allows the elemental composition of the specimen to be identified [16]. By comparing the intensities of the peaks with that of a standard sample we can obtain the relative amount of the atomic species present in the sample and hence the accurate composition of the sample can be determined [17, 18].

3.5.3 Secondary Ion Mass Spectroscopy

Secondary ion mass spectroscopy (SIMS) is one of the most sensitive surface analytical techniques capable of detecting impurity elements present in a surface layer at < 1ppm concentration. This is because of the inherent high sensitivity associated with mass spectrometric based techniques. There are a number of different variants of the technique.

Static SIMS: Used for sub-monolayer elemental analysis

Dynamic SIMS: Used for obtaining compositional information as depth profiling

Imaging SIMS: Used for spatially resolved elemental analysis

SIMS is based on the principle that charged particles (secondary ions) are ejected from a material surface when bombarded by a primary beam of heavy particles (shown in figure 3.11).

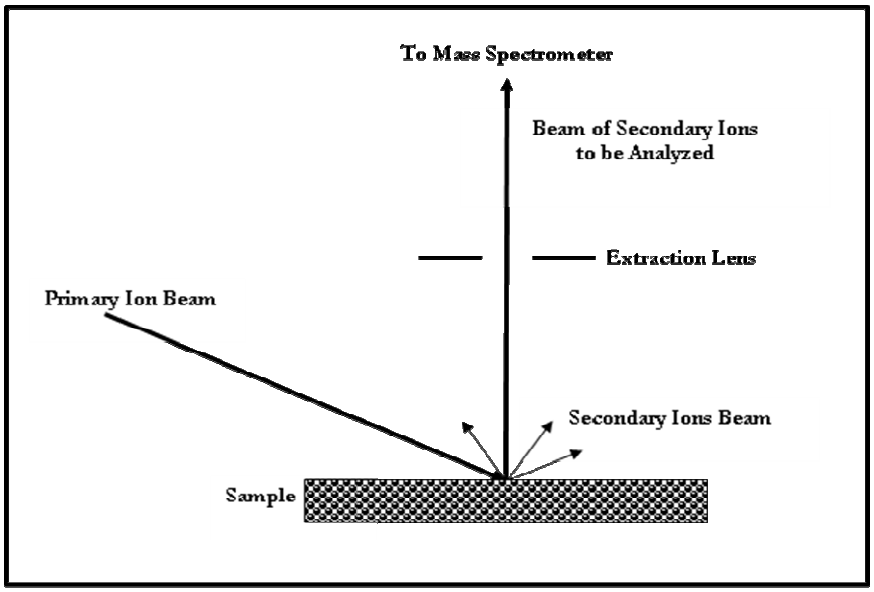

Fig. 3.11 Schematic representation of secondary ion sputtering

A basic SIMS instrument consist of (1) a primary ion beam source (generally O_2^+, O^-, Cs^+, Ar^+ or neutrals) to supply the bombarding species, (2) a target or specimen which should be solid and must be stable in vacuum, (3) an extraction electrode, (4) a mass analyzer to isolate the ion of interest and (5) an ion detection system to record the magnitude of the secondary ion signal (usually a Faraday cup or an electron multiplier or a CCD camera).

In SIMS, a solid specimen is bombarded with a narrow beam of primary ions. A mass spectrometer separates the ejected secondary electrons according to their mass to charge (m/e) ratio and counts them. This recorded value of m/e is

used to determine the element or compound based on the atomic or molecular weight, and the counts give information about the concentration. As the sputtering process inherently erodes the sample, dynamic SIMS (DSIMS) provides useful depth profiling data during the analysis.

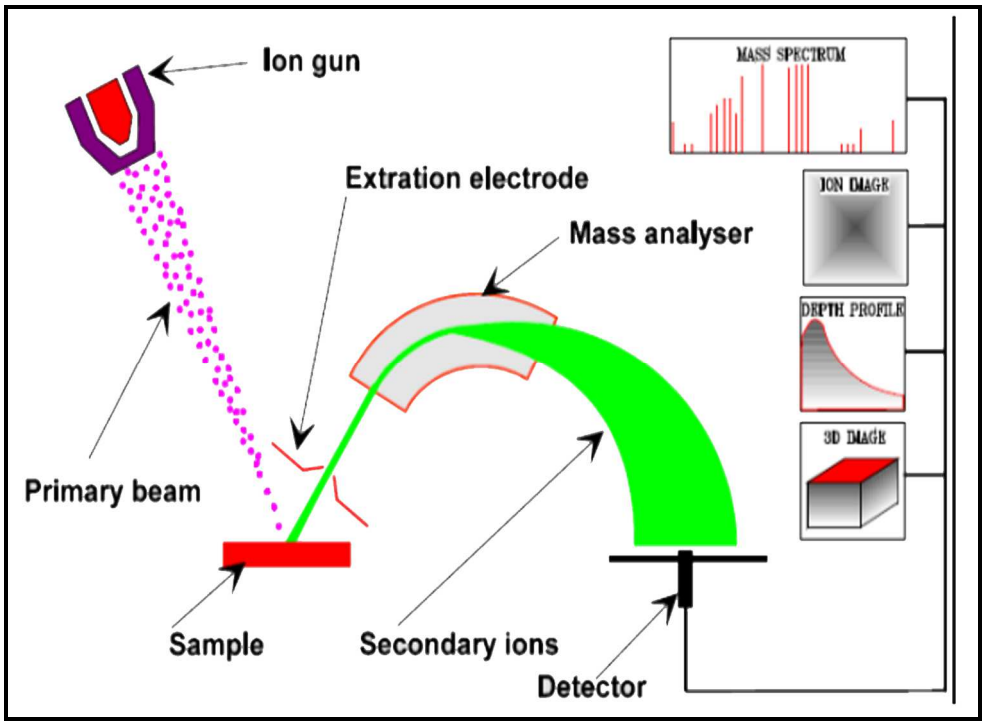

Fig. 3.12 Components of SIMS

SIMS Analysis can detect every element in the periodic table with detection limits well below the ppm range. The main drawback of this experimental technique is that it's a destructive technique.

3.6 Topographical Characterization

3.6.1 Atomic Force Microscopy

The atomic force microscope (AFM) is another member of general scanning probe microscopes (SPM) and was designed by G. Binnig in 1986 [19]. AFM is a technique to obtain images and other information or local properties such as height, friction, magnetism etc. at extremely high (nanometer) resolutions.

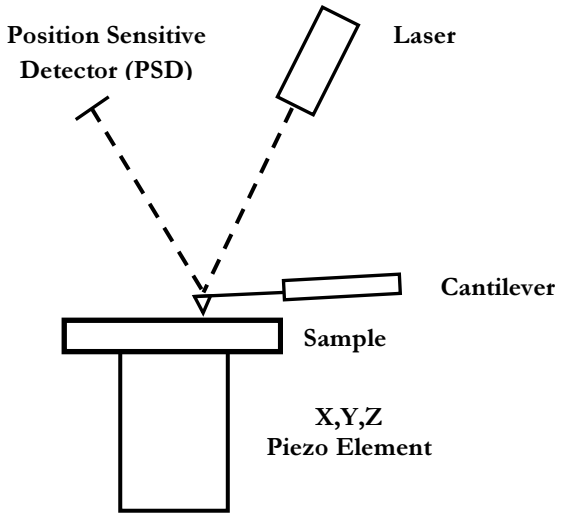

Fig. 3.13 AFM apparatus principle

AFM can operate on conducting and non-conducting solid surfaces. Here the force of interaction between a sharp tip and the surface is measured. As this force of interaction does not depend on electrically conducting samples or tips, AFM can be applied to insulators as well. For measuring these forces, a tip is mounted on a cantilever type spring. This force of interaction between tip and sample causes the cantilever to deflect according to Hooke's law;

$$F = c.\Delta z \tag{3.8}$$

where c is the spring constant of the tip and Δz is the deflection.

Deflection of the cantilever can be sensed by different means. Most common one is laser deflection technique which is an optical detection method and is shown in figure 3.13. Here the cantilever displacement is measured by detecting the deflection of the laser beam which is reflected from the rear side of the cantilever. A position sensitive photodiode array is used as the detector. Such a configuration measures the deflection of cantilever due to bending and torsion forces separately. The detection of bending forces allows the imaging of surface topography whereas the torsion force reports on friction forces. As the sample is scanned under the tip, the x, y and z position of the sample surface with respect to the tip is determined by a piezoelectric tube scanner. The movement of the sample in the z-direction, that is needed to keep the deflection at its constant set point level, is registered during x-y scanning, and a three dimensional map is constructed which is closely related to the topography of the surface.

According to Hooke's law, the raster scanned cantilever exhibits a locally varying deflection which directly represents the corrugation of the sample surface. Here the distance regimes are shown in figure 3.14. The cantilever is kept less than a few angstroms from the sample surface in the contact regime and an attractive force exists between the cantilever and the sample.

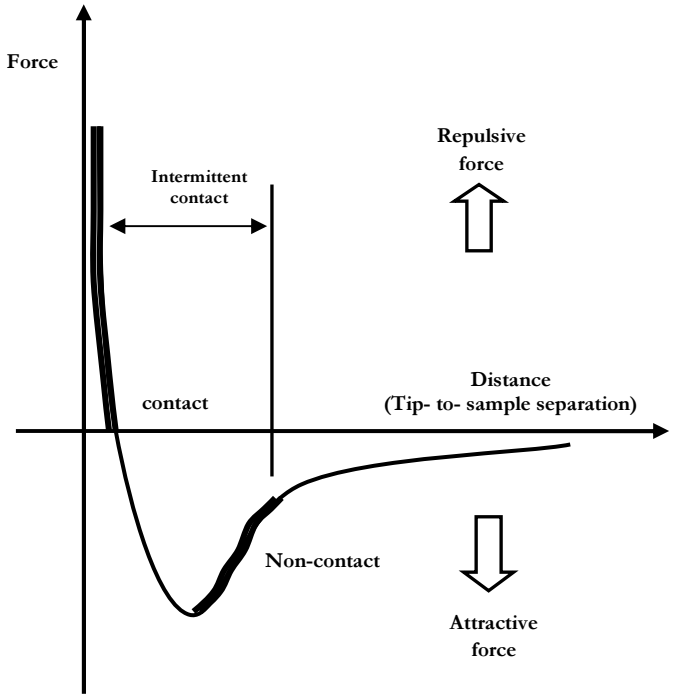

Fig. 3.14 Force experienced by the tip in the approach to the sample

Contact mode AFM

In contact mode, an AFM tip is brought in soft physical contact with the surface at a certain value of the force. This force is kept constant with a feedback system that retracts the tip when the measured force is above the set value and approaches it when the force falls below the set value. When the feedback system is responding fast to small changes in the applied force, then the z position of the tip is adjusted to keep the force constant. In such a case, the voltage applied to the piezoelectric carries accurate topographic information and this imaging mode is known as 'topographic mode/constant force/constant deflection mode'. If the response of the feedback system is slow, only the average force will be a constant

and the features of the surface will cause variations on the force about its set value. Here force is displayed directly and this mode of operation is known as 'variable force mode or force mode'.

Non-contact Mode AFM

In non-contact mode of operation, the probe is kept at least one nanometer from the sample surface so that only long range interactions remain. In general, the relevant forces result from the van der Waals interactions or electrostatic/magnetostatic interactions. As van der Waals forces are relatively small and capillary forces can be avoided by either choosing a sufficiently large working distance or by working on clean surfaces, one can yield relatively strong forces from electrostatic/magnetostatic interactions. Thus the electrical or magnetic charge distribution in the near surface regime of the sample can be recorded.

Intermittent contact (Tapping mode) AFM

In this mode, the cantilever tip is oscillated at or near its resonant frequency. The oscillating probe is then scanned at a height where it barely touches or "taps" the specimen surface. The system records the probe position and vibrational amplitude to obtain topographical and other property information. Accurate topographical information can be obtained even for very delicate surfaces. Optimum resolution is about 50 Å lateral and <1 Å height. Images for phase detection mode, magnetic domains, and local electric fields are also obtained in this mode.

3.6.2 Magnetic Force Microscopy

Magnetic force microscopy (MFM) images the spatial variations in the magnetic forces at the sample's surface. The probe tip is coated with a thin film of

ferromagnetic material. This will react with the magnetic stray fields on the sample surface. The magnetic forces between the tip and the sample are measured by monitoring cantilever deflection when the probe is scanned at a constant height above the surface. The resonant frequency changes of the cantilever are noted.

$$\text{resonant frequency} = \frac{1}{2\pi}\sqrt{\frac{\text{spring constant}}{\text{mass}}} \qquad (3.9)$$

The strength of the local magnetostatic interaction determines the vertical motion of the tip as it scans across the sample. An image taken with a magnetic tip contains information about both, the topography and the magnetic properties of the sample surface. The distance between the tip and surface determines the dominant effect. If the tip is more close to the surface, the image will be predominantly topographic. If the separation between the tip and the sample is more, magnetic effects become apparent. Collecting a series of images at different tip heights is one way to separate magnetic and topographic effects.

3.7 Magnetic Measurements

3.7.1 Vibrating Sample Magnetometry

Vibrating sample magnetometer (VSM) is the most common instrument for the measurement of magnetization. After the invention of this instrument by S. Foner [20] there have been many modification and improvement of this instrument [21]. But the basic principle remains the same. A VSM operates on Faraday's Law of Induction, i.e., a changing magnetic field will produce an electric field. This electric field can be measured and provides us information about the changing magnetic field. The schematic of a vibrating sample magnetometer is given in figure 3.15.

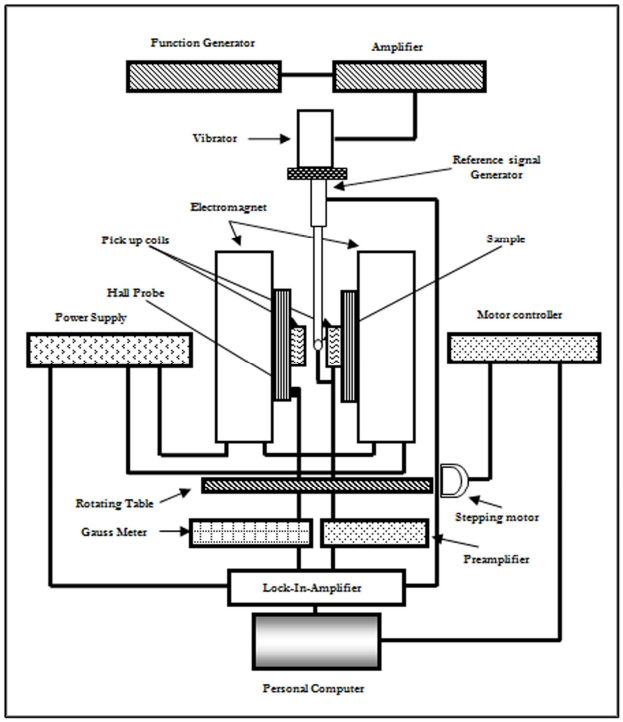

Fig. 3.15 Schematic of a Vibrating sample magnetometer

In a VSM, the magnetic specimen is placed in a constant magnetic field. This constant magnetic field will magnetize the magnetic specimen by aligning the magnetic domains or the individual magnetic spins with the field. Hence the magnetic dipole moment of the sample will create a magnetic field around the sample, called a magnetic stray field . This magnetic sample is vibrated with a certain frequency and amplitude employing a vibrator. The change of magnetic stray field as a function of time caused by the vibration of magnetized sample can be sensed by a set of pick-up coils. The changing magnetic flux will induce an electric field in the pick-up coil according to Faraday's law of induction and this

current will be proportional to the magnetization of the sample. This induced current is amplified by a trans-impedance amplifier and a lock-in-amplifier. These components are interfaced via a computer. Using controlling and monitoring software, the system provides us information on how much the sample is magnetized and how its magnetization depends on the strength of the constant magnetic field. When the constant field is varied over a range of values, a plot of magnetization versus magnetic field strength is generated.

Let a dipole moment be induced in the sample when it is placed in a uniform magnetic field M. Then the amount of magnetic flux linked with the coil placed in the vicinity of this magnetic field is given by

$$\phi = \mu_0 n \alpha M \tag{3.10}$$

where μ_0 is the permeability of free space, n is the number of turns per unit length of the coil and α represents the geometric moment decided by the position of moment with respect to coil as well as shape of coil.

Here an anharmonic oscillator of the type, $z = z_0 + Ae^{j\omega t}$ induces an emf in the stationary detection coil. The induced emf is given by

$$V = -\frac{d\phi}{dt} = -j\omega\mu_o nMA\left(\frac{\partial\alpha}{\partial z}\right)e^{j\omega t} \tag{3.11}$$

If the amplitude of vibration A, frequency ω and $\left(\frac{\partial\alpha}{\partial z}\right)$ are constant over the sample zone then induced voltage is proportional to the magnetic moment of the sample. This is the basic principle behind VSM [22, 23]. A cryogenic set up associated to the sample allows low temperature measurements.

3.7.2 Superconducting Quantum Interference Device

A superconducting quantum interference device (SQUID) is one of the most effective and sensitive ways of measuring magnetic properties. Using a device called a Josephson junction, a SQUID can detect a change of energy as much as 100 billion times weaker than the electromagnetic energy that moves a compass needle. The SQUID magnetometer consists of two superconductors separated by thin insulating layers to form two parallel Josephson junctions so that electrons can pass through in both directions. The sensitivity of the SQUID devices is associated with measuring changes in magnetic field associated with one flux quantum (h/2e). The basic principle of a SQUID magnetometer is that, if a constant biasing current is maintained in the SQUID device, the measured voltage oscillates with the changes in phase at the two junctions, which depends upon the change in the magnetic flux. By counting these oscillations we can evaluate the flux change that has occurred in the sample. Hence, when the sample is moved through the superconducting magnetic coils, a flux change is induced in the pick-up coils. Highly magnetic sample should be moved slowly through the coils in order not to exceed the maximum slewing rate of the electronic system [24]. SQUIDs have been used for a variety of applications that demand extreme sensitivity, including biomagnetism, susceptometers, geophysics scanning SQUID microscope, and nuclear magnetic resonance [25].

3.8 Ferroelectric Loop Tracer

Ferroelectricity is a property of certain materials in which they possess a spontaneous electric polarization that can be reversed by the application of an external electric field. A ferroelectric loop tracer or P-E loop tracer is used to

measure the ferroelectric behaviour of materials. From a P-E loop, parameters namely saturation polarization (P_s), remanence polarisation (P_r) and coercive electric field (E_c) can be derived.

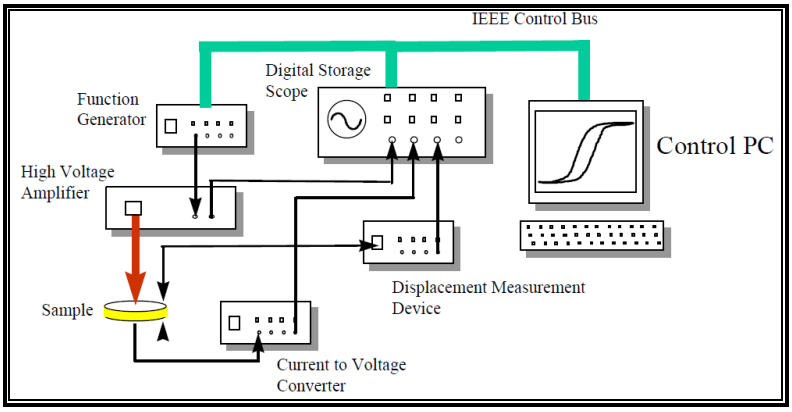

Fig. 3.16 Block diagram of a ferroelectric loop tracer

An experimental set up that can be used as a P-E loop tracer is shown in figure 3.16. Here an initial wave shape is formed by a function generator, which is then amplified by the high voltage amplifier. The amplified wave form is sent to the sample. The current passing through the sample is converted to a voltage via a current to voltage convertor. This signal is captured on a digital storage oscilloscope along with the monitor output from the high voltage amplifier and waveforms from a displacement measuring device connected. The captured waveforms are then sent to a computer for further analysis.

3.9 Magnetoelectric Coupling Measurement set up

Magnetoelectric materials possess two or more switchable states such as electric polarization, magnetization or strain. Hence they can change magnetization by electric field or electric polarization by a magnetic field. The

interplay between the magnetic and electric states is realized via the magnetoelectric (ME) effect which is defined as the coupling of electric field and magnetic field. The ME effect is usually described mathematically by the linear ME coupling coefficient (MECC). The exact knowledge of this MECC is essential for the design of devices and sensors based on ME materials. The measurement set up for magnetoelectric (ME) coupling studies is shown in figure 3.17.

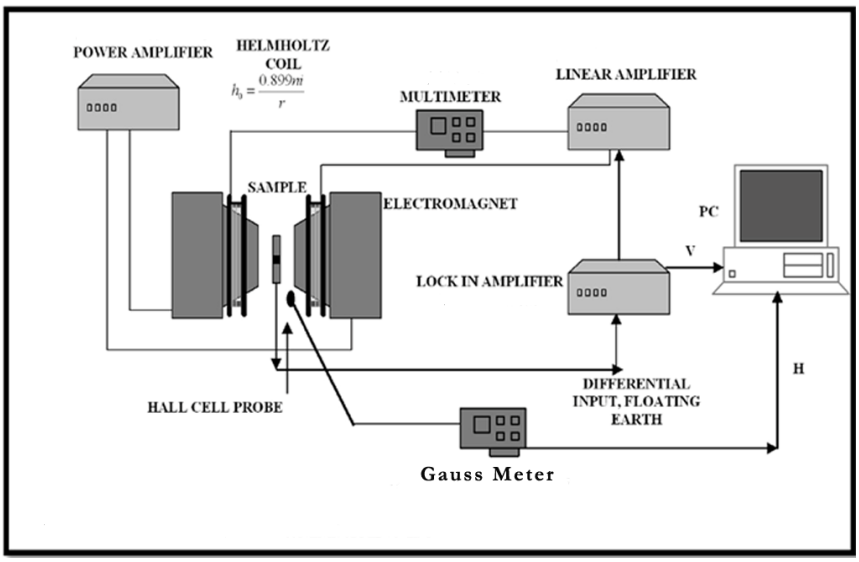

Fig. 3.17 Measurement set up for ME coupling studies

The setup consists of an electromagnet and a pair of Helmholtz coils that generate the dc bias field and the ac driving field, respectively. The angle between the two applied magnetic field vectors is critical. Various studies on the ME coefficient as a function of angle have proved that the maximum effect is obtained when the fields are parallel to each other, whereas the effect is zero when the fields are in transverse position [26]. Here, the off-resonant ME coupling coefficient was determined at room temperature as a function of the biasing dc

magnetic field by measuring the ME voltage developed when a low frequency magnetic field with a known amplitude was applied to the sample in the form of thin film cantilevers. A lock-in amplifier is employed to record the voltage developed across the sample. The signal from the linear amplifier is given to the lock-in amplifier as reference signal. DC magnetic field dependence can be studied both in longitudinal and transverse mode. Transverse measurement mode is defined as when the polarization and magnetic field vectors are perpendicular to each other (Magnetic field in plane to the sample, voltage measured perpendicular to the sample, so that polarization and magnetic field vectors are perpendicular). Longitudinal mode is defined as when the polarization and magnetic field vectors are parallel to each other (Magnetic field perpendicular, voltage measured perpendicular to the sample again, so that polarization and magnetic field vectors are parallel).

References:

1. Powell, C. F.; Oxley, J. H. and Blocher Jr, J. M. *Vapor Deposition*; Wiley, New York (1967)
2. Westwood, W. D. *Sputter Deposition; AVS Education Committee book series*, v. 2. New York: Education Committee (2003)
3. Scriven L.E *Physics and applications of dip coating and spin coating*, MRS proceedings, 121(1988)
4. Mirtat Bouroushian, Tatjana Kosanovic, *Characterization of Thin Films by Low Incidence X-Ray Diffraction, Crystal Structure Theory and Applications*, 1, (2012) 35-39
5. M. Nauer, K. Ernst, W. Kautek, M. Neumann-Spallart, *Thin Solid Films*, Vol. 489, No. 1-2, (2005) 86-93
6. K. Wang, C. Steimer, D. Wamwangi, S. Ziegler and M. Wuttig, *Applied Physics A: Materials Science & Processing*, Vol. 80, No. 8, (2005) 1611-1616
7. P. Colombi, P. Zanola, E. Bontempi, R. Roberti, M. Gelfi and L. E. Depero, *Journal of Applied Crystallography*, Vol. 39, Part 2, (2006) 176- 179
8. S. Debnath, P. Predecki and R. Suryanarayanan, *Pharmaceutical Research*, Vol. 21, No. 1, (2004) 149-159
9. A. A. Williams, J. M. C. Thornton, J. E. Macdonald, R. G. Vansilfhout, J. F. Vanderveen, M. S. Finney, A. D. John- son, C. Norris, *Physical Review B*, Vol. 43, No. 6, (1991) 5001-5011
10. O. C. Wells, *Scanning Electron Microscopy*, McGraw-Hill, New York (1974)
11. Weilie Zhou, Zhong Lin Wang, *Scanning Microscopy for Nanotechnology Techniques and Applications,* Springer (2006)

12. Egerton, R, *Physical principles of electron microscopy*. Springer. ISBN 0-387-25800-0 (2005)
13. Rose H H, *Optics of high-performance electron Microscopes, Science and Technology of Advanced Materials* 9: (2008) 014107
14. D.J. Smith, *Reports Prog. Phys*. (1997) 1513-1580
15. C. Richard Brundle, Charles k Evans, Jr., Shaun Wilson, *Encyclopedia of Materials Characterization, Surfaces, Interfaces, Thin Films,* Manning Publications Co., 1992
16. Joseph Goldstein, *Scanning Electron Microscopy and X-Ray Microanalysis*, Springer. ISBN 978-0-306-47292-3. (2003)
17. Lin. C. H, Kuo, P. C, Pan J. L, Huang D. R, *J. App. Phys.* 79, (1996) 6035
18. Xu. X, Freidman G, Humfield K. D, Majetich S. A, Acher, *Chem. Mater*. 14, (2002)1249
19. G.Binnig, C.F.Quate, Ch.Gerber, *Phys.Rev. Lett*. Vol.56, (1986) 9
20. S. Foner, *Rev. Sci. Instr*. 30, (1959) 548-558
21. R. V. Krishnan and A. Banerjee, *Rev. Sci. Instr*. 70, (1999) 85-91
22. Dormann J. L, Fiorani, *J. Magn. Magn. Mater.* 415 (1995) 140
23. BaIlIe X, Labarta, A, J. *Phys. D: Appl. Phys*. 35(2002) R 15
24. K. Gramm, L. Lundgren, Beckman, *Physica Scripta*,13, (1976) 93
25. J.C Denardin, A.L Brandl, M Knobel, A.B Pakhomov. H Lin, X.X Zhang, *Phys. Rev.B*. 65, (2002) 061122
26. Fetisov Y K, Bush A A, Kamentsev K E, Ostashchenko A Y, Srinivasan G *IEEE Sens. J*. 6 (2006) 935

CHAPTER 4

EVOLUTION OF STRUCTURAL AND MAGNETIC PROPERTIES OF Co–Fe BASED THIN FILMS WITH THERMAL ANNEALING AND SWIFT HEAVY ION IRRADIATION

G. Pookat et al., Surf.coat.technol. 236 (2013) 246–251

G.Pookat et al., Nucl. Instr. And Meth. In Phys. Res. B 310 (2013) 81-86

4.1 Introduction

Amorphous and nanocrystalline magnetic alloys are widely investigated owing to their excellent magnetic properties. Amorphous metallic alloys of transition metals and metalloids or glass former alloys are strongly magnetic at room temperature and offer several opportunities for engineering applications. They contain about 80% transition metals like Fe, Co and Ni, and about 20% metalloid or glass former elements like Si, B, C or P and are also known as metallic glasses. By subjecting the materials to mechanical or thermal processing methods or by the addition of alloying elements, their chemical, physical and mechanical properties can be altered. These alloys lack long range atomic ordering and hence exhibit no microstructural discontinuities like grain boundaries on which magnetic domain walls can be pinned. Hence such ferromagnetic metallic glasses based on 3d transition metals are excellent soft magnetic materials with low hysteresis loss and low eddy current dissipation. The excellent soft magnetic properties exhibited by amorphous and nanocrystalline magnetic alloys make them ideal for applications in diverse fields, ranging from magneto-optic storage, magnetic shielding, magnetic sensors etc [1-3]. Micro/Nano Electro Mechanical Systems (MEMS/NEMS) devices such as microactuators, sensors and micromotors can be realized with the use of both hard and soft magnetic materials. These electromagnetically actuated MEMS are more stable for large actuation gap and high force applications. The high magnetic moment of Co rich binary alloys makes it suitable for these applications [4,5]. Miniaturization of these materials are required for microelectronic applications, hence thin films of these alloys are of great importance [6]. Increase in the stress developed during the film growth accounts for the relatively high value of magnetostriction observed in Co-Fe thin films.

Generally, crystalline structures will be weakly magnetic with low magnetization and low Curie temperatures. They also exhibit high magnetocrystalline anisotropy and hence possess large coercive field. But, their amorphous counterparts display enhanced magnetization as a result of local disorder and lower density which tend to localize the 3d electrons. The random distribution of magnetic easy axes results in negligible macroscopic anisotropy in amorphous magnetic alloys [7]. With high magnetic moment, Co-Fe alloy thin films are known for their technological applications such as soft under layer for perpendicular recording and in modern recording heads [8-10]. Microstructure of these magnetic thin films plays an important role in deciding the magnetic properties which in turn depends on parameters like film thickness, crystallinity, surface/interface roughness, and composition. In particular, the variation in surface/interface roughness modifies the magnetic properties like magnetic anisotropy, coercivity and magnetic domain structure. Thermal annealing [11-12] and swift heavy ion irradiation [13-15] are two effective methods employed to alter the surface microstructure and morphology.

Research interest in metallic glasses is growing over the last few decades ever since the first discovery of amorphous alloys of Au-Si by Duwez et al. in 1959 [16]. The investigations on the improvement in soft magnetic properties of the nanocrystalline alloys of Fe-Si-B-M (M=Cr,V,Mo,Nb,Ta,W) by Yoshizawa et al. in 1988 [17] accelerated the growth of research in this area. Later, studies on the nanocrystalline family of NANOPERM^{TM} (Fe-Zr –B- Cu) [18] and HITPERM^{TM} (Fe-Co-Zr-B-Cu) [19], shed further light on the origin of soft magnetic properties [20] and the amorphous nanocrystalline transformation [21, 22]. Among them Co and Fe rich alloys are widely used in technological applications like sensors, actuators and magnetic recording heads [23,24] as they

exhibit excellent magnetic properties like high Curie temperature, high permeability, low magnetic loss, low coercivity and high saturation magnetization [25-30].

Annealing of amorphous alloy thin films enables the relaxation of amorphous structure and initiates formation of a composite amorphous microstructure with crystal of size of ~10 nm. Such a microstructure is expected to improve the soft magnetic properties. Several reports are there on thermally induced nanocrystallization in Co-based alloys [31-33]. Bordin et al. [34] reported the occurrence of superior soft magnetic properties with the evolution of nanocrystallites with heat treatment of $Co_{66}Fe_4Mo_2B_{11.5}Si_{16.5}$ amorphous ribbons well below their conventional crystallization temperature. Quintana et al. [31] reported nanocrystallite formation below the conventional crystallization temperature in $Co_{66}Fe_4Mo_2Si_{16}B_{12}$. Buttino et al. [35] also reported improvements in soft magnetic properties of an amorphous alloy of composition $Co_{66}Fe_4Ni_1B_{14}Si_{15}$. These improvements were obtained by isothermal treatments below conventional crystallization temperature.

Structural relaxation and crystallization during thermal annealing result in considerable changes in magnetic properties. For example, nanocrystalline cobalt based alloys display superior magnetic softness compared to their amorphous counterparts [36, 37]. The magnetic properties display a strong dependence on the nanocrystalline size and distribution [38]. If the amorphous matrix is nonmagnetic, the behavior of the magnetic nanocrystals is governed by a single domain particle model; whereas in the case of a magnetic matrix it is more complicated. Detailed investigations of such nanocrystalline magnetic systems have resulted in useful applications like soft under layers for ultrahigh density computer disk drives and magnetic sensors [39-41].

Gupta et al. reported that energy deposition by 120 MeV Au ions leads to changes in structural and magnetic behaviour of Co thin films [42]. Klaumuenzer et al. in 1986 reported on the plastic deformation of the surface of metallic glasses due to swift heavy ion irradiation [43]. Generally the incident energy of 1eV in the sample initiates a temperature rise of 10^4 K along the ion trajectory [44]. In ion beam irradiation, the surface topography of the sample is decided by the interplay between the dynamics of surface roughening due to sputtering and smoothing due to material transport during surface diffusion. The competition between these two processes results in the formation of different surface features. Gupta et al. demonstrated that the magnetic field assisted ion implantation is an effective method for the modification of extrinsic magnetic properties of Co-Fe thin films [45]. In short, SHI irradiation can be employed for the topographical modification of surfaces and interfaces in the nanometer scale.

Irradiation will result in loss of energy of the ions in the target material via elastic or inelastic collisions. The process through which the swift heavy ions lose their energy can be classified as follows. (i) electronic energy loss $[(dE/dx)_e]$ in which the interaction with target electrons occurs via inelastic collisions leading to excitation and ionization of target atoms (at energy above ~ 1MeV/nucleon), (ii) nuclear energy loss, $[(dE/dx)_n]$ in which direct screened Coulomb interaction with target atom nuclei is responsible for the energy loss and (iii) radiation loss such as Bremsstrahlung and Cerenkov radiation which is very small and can be neglected. The nuclear energy loss is dominant at ion energies below 10keV/nucleon [46-50]. While irradiating with swift heavy ions, large amount of energy will be deposited on the lattice via electron– phonon interactions. The mechanisms behind energy transfer are well explained using the Coulomb explosion [46, 51] and

thermal spike model [52-54]. Normally the term 'stopping power' or (dE/dx) is used to describe the energy deposition via the slowing down of ions in the material. However, (dE/dx) gives the energy loss per unit length along the particle trajectory, whereas the stopping power stand for the ability of the material to stop down the heavy ion and is represented by $(-1/\delta)(dE/dx)$, where δ is the density of the material. In the swift heavy ion- solid interactions, nuclear stopping power S_n is negligible compared to electronic stopping power S_e. The nuclear interactions result in lattice disorder by the displacement of atoms from their positions whereas, electronic collision leads to negligible deflection of ion trajectory and small energy loss per interaction. Theoretical calculation of the stopping power can be done using computer simulation methods employing the well developed simulation programme TRIM/SRIM (Transport of ions in matter, in more recent versions called Stopping and Range of Ions in Matter). SRIM is a group of programs which calculates the stopping and range of ions in matter using a binary approximation of ion–atom collisions [55]. In such programs the simulation of the ion collisions with nuclei in the medium is carried out to find the stopping power [44].

The material under study here is Co-Fe based thin films where $Co_{75}Fe_{14}Ni_4Si_5B_2$ is used as the target material. For fabrication of amorphous alloy thin films one can employ processes like physical vapor deposition (PVD), chemical vapor deposition (CVD) or atomic layer deposition [56]. Here we have employed thermal evaporation which is a physical vapor deposition technique for the growth of thin film and is cost effective and can be carried out in any common laboratory.

From a fundamental point of view investigation on the effects of thermal annealing assumes significance since the onset of nanocrystallisation is very

important and this determines its magnetic properties. Moreover, thermal annealing induces microstructural changes which in turn will have a bearing on the magnetic properties of the film. This is one of the objectives of the present investigation. The structural, magnetic and topographical properties can also be tailored by impinging swift heavy ions. The microstructural modifications induced by swift heavy ion irradiation lead to the modification of magnetic properties. A detailed investigation on this aspect is another objective of this study.

4.2 Experimental Techniques

4.2.1 Preparation of Co-Fe thin films

Thin films based on Co-Fe were deposited on naturally oxidized silicon (100) substrates by thermal evaporation, using a composite target having the composition $Co_{75}Fe_{14}Ni_4Si_5B_2$. Film deposition was carried out at room temperature at a pressure of $1x10^{-6}$ Torr with the source to substrate distance of 11 cm. A set of samples were also deposited simultaneously onto NaCl substrates for transmission electron microscopy (TEM) investigations.

The differential thermal analysis (DTA) of the target material was carried out to find out the crystallisation temperature of the material. On the basis of that study, as deposited thin films were annealed at different temperatures of 373 K, 473 K, 573 K and 673 K for 1 hour under high vacuum conditions ($1x10^{-6}$ Torr) to initiate nanocrystallisation in these films [57-61].

Also the changes on topographical and magnetic properties in Ag^{7+} ion irradiated $Co_{77}Fe_{23}$ alloy films are investigated. We have chosen amorphous Co-Fe thin films for irradiation studies in the light of the fact that the magnetic moment for this alloy is maximum among 3d ferromagnetic alloys according to the Slater-Pauling curve [62].

4.2.2 SHI irradiation

Thin film samples were mounted on an electrically insulated sample ladder and the ladder current was integrated to collect and count the charge pulses via a scalar counter along with the digital current integrator. 100MeV Ag^{7+} ions were used to irradiate the Co-Fe films at room temperature with fluences of 1×10^{11}ions/cm^2, 1×10^{12}ions/cm^2, 1×10^{13}ions/cm^2 and 3×10^{13}ions/cm^2 using a 15UD Pelletron accelerator at the Inter University Accelerator Centre, New Delhi, India. The beam current was maintained at 1.5 pnA (particle nanoampere). This is kept low in order to avoid the heating up of the sample during irradiation. The beam is raster scanned over an area of 1×1cm^2 using a magnetic scanner. The damage caused by the interaction between the ion beam and target material was calculated using the SRIM software. The electronic stopping power S_e, nuclear stopping power S_n and the residual range R_P of the 100MeV Ag^{7+} ions in Co-Fe was calculated using SRIM-2006. The typical values of S_e, S_n and R_p are estimated to be 18.16 eV/Å, 2.95×10^3eV/Å and 6.33μm respectively for Ag^{7+} ions having energy 100MeV in $Co_{77}Fe_{23}$ thin films. The film thickness is much less than the projected range, hence the chances of any ion implantation in the Co-Fe film is very remote. In this experiment the entire contribution of radiation effects due to the passage of ions is by electronic energy loss.

4.2.3 Characterization techniques

The thickness of the deposited film was measured using Dektak 6M thickness profiler. Glancing angle X-ray diffraction (GAXRD) study of the as prepared, annealed and irradiated films were performed using a Bruker Discover D-8 diffractometer with CuK_α (λ=1.54 Å) radiation. X-ray photoelectron spectroscopy (XPS) study of the as prepared thin films was carried out using an

Omicron Nanotechnology XPS system with a monochromatic Al K_α radiation ($h\nu$= 1486.6 eV), of source voltage 15 kV and emission current of 20 mA. All scans were carried out at a base pressure of 2 x 10^{-11} Torr. The wide scan was recorded with constant analyzer transmission energy of 50 eV, while the individual elemental peaks were recorded at analyzer pass energy of 20 eV. The obtained XPS spectra were deconvoluted using Casa XPS program (Casa Software Ltd, UK) [63] in which the background was simulated using Shirley function and the peaks were fitted using a Gaussian- Lorentzian function. The recorded spectra were corrected using the binding energy of aliphatic carbon at 285 eV and the accuracy of the measured binding energy values is estimated to be equal to ± 0.2 eV. The depth profile of the representative film was recorded via secondary ion mass spectroscopy (SIMS) to confirm the absence of silicon in the film composition. The SIMS analysis of the as prepared film was performed using Hiden Analytical SIMS Workstation using oxygen ion beam at 2keV, 100nA at a pressure of $8x10^{-8}$ Torr. The microstructural evolution of the annealed films was investigated by transmission electron microscopy (TEM) (Jeol JEM-2200 FS) operated at 200 kV. The surface morphology of the as deposited, annealed and irradiated Co-Fe films was imaged using atomic force microscopy (AFM) multimode instrument, having higher resolution magnetic force microscopy tips (MESP-HR) (Bruker) with resonant frequency of 475 kHz. The magnetic force microscopy (MFM) analysis was used to detect the surface magnetization present on the film via the interaction of the magnetic tip with the stray magnetic field on the sample surface. MFM imaging was carried out at a lift height of 10 nm, scan rate of 0.5 kHz and resolution of 512 pixels. The quantitative analysis of the AFM images were done with the help of surface analysis software Nanoscope 7.2 (Vecco Scientific Ltd) to obtain PSD, roughness and depth analysis [64]**.** The

MFM images of irradiated films were analyzed also using SPIP software (version 6.0.6, Image Metrology A/S, Horsholm, Denmark) to obtain the angular correlation and texture direction index. Room temperature magnetization measurements were carried out using a VSM (DMS 1660 VSM) with a magnetic field varying from −13 to +13 kOe.

4.3 Results and Discussion

4.3.1 Evolution of structural and magnetic properties of Co-Fe based thin films with thermal annealing

4.3.1.1 Composition analysis

.

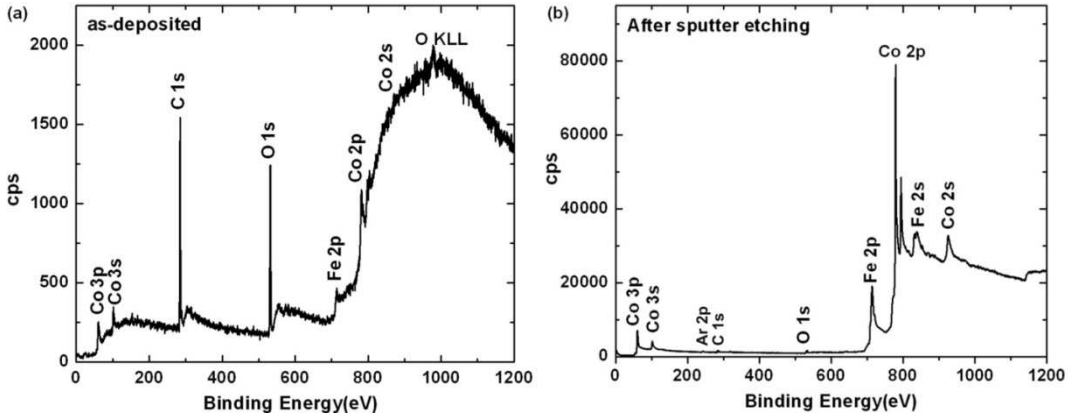

Fig. 4.1 XPS survey scans of (a) as-deposited film and (b) after sputter etching for 30 minutes using Ar^+

The nominal thickness of the deposited thin films, as determined using a stylus profiler was found to be 40 nm. The wide scan XPS spectrum of the as-deposited film (figure 4.1(a)) shows the presence of cobalt and iron along with unavoidable surface contaminants like carbon and oxygen. XPS spectrum was also recorded after removing the surface oxide layer by Ar+ sputtering (3 keV) for 30 minutes. The resultant spectrum shows that the film is rich in cobalt and iron

along with traces of oxygen, carbon and argon (figure 4.1(b)). Argon is expected to be implanted in the films during the sputter etching process

High resolution XPS spectra of elemental components, Co and Fe acquired after removing the surface contaminants is shown in figure 4.2. Curve fitting of the experimental data presented in figure 4.2(a) revealed different components at binding energies of 707.2 eV, 710.7 eV and 714.2 eV for Fe $2p_{3/2}$. These peaks represent Fe in different oxidation states, namely Fe^0, Fe^{2+} and Fe^{3+} [65]. The multiplet splitting of Fe 2p as well as a satellite peak of Fe $2p_{3/2}$ at around 717 eV [65] was also observed. Corresponding Co 2p high resolution spectra is shown in figure 4.2(b). Curve fitting to Co $2p_{3/2}$ line resulted in three components centered at 777, 778 and 780 eV, which corresponds to the presence of Co in the oxidation states Co^0, Co^{2+} and Co^{3+} respectively [66-68]. It is to be noted that the intensity of Fe $2p_{1/2}$ and Co $2p_{1/2}$ peak was small for resolving all the three components that was observed for their corresponding $2p_{3/2}$ peaks.

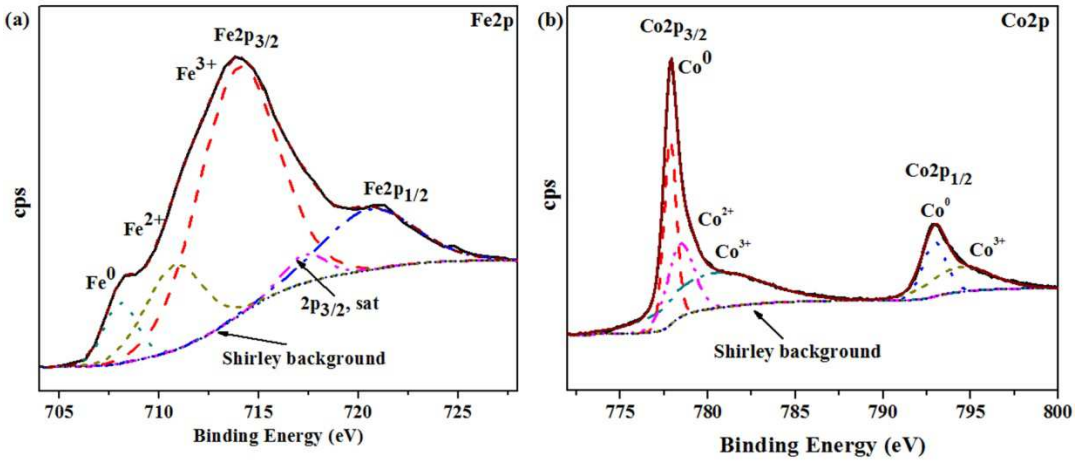

Fig.4.2 High resolution XPS spectrum of (a) Fe 2p and (b) Co2p

High resolution XPS spectrum was also acquired in the energy range of 94-110 eV. However it was difficult to deconvolute the Si 2p and Co 3s lines

because of their similar binding energies [69]. Quantification of the spectra in figure 4.1(b) yielded the composition of the film as 76.81 wt% of Co and 22.72 wt% of Fe, along with traces of oxygen.

The energy dispersive X-ray spectrometry (EDAX) pattern of the representative Co-Fe film is shown in figure 4.3. The peaks corresponding to carbon and oxygen indicates the unavoidable hydro carbon contamination on the top surface of the film (figure 4.3) which further confirmed the XPS results of the as deposited film shown in figure 4.1(a).

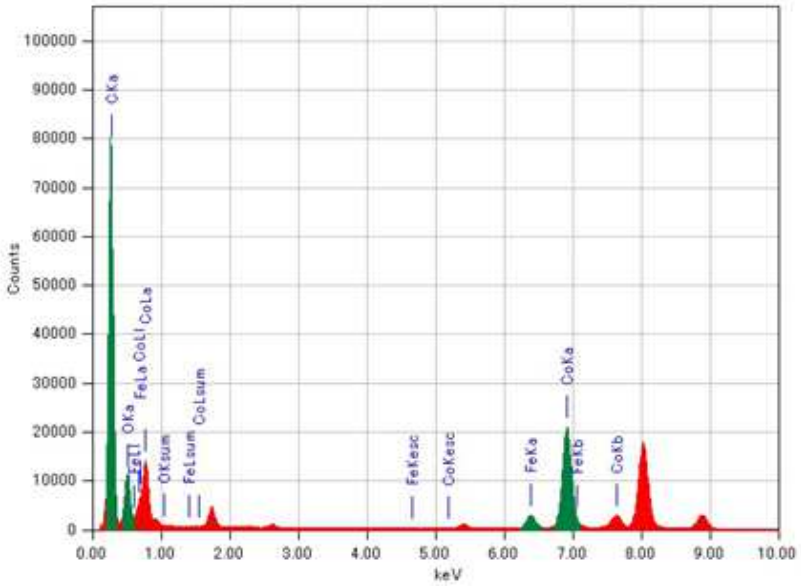

Fig. 4.3 EDAX Spectrum of representative film

The depth profiling of the composite elements in the film was obtained through the SIMS pattern of the representative Co-Fe film and is depicted in figure 4.4. The presence of silicon in the SIMS pattern was assigned to substrate contribution.

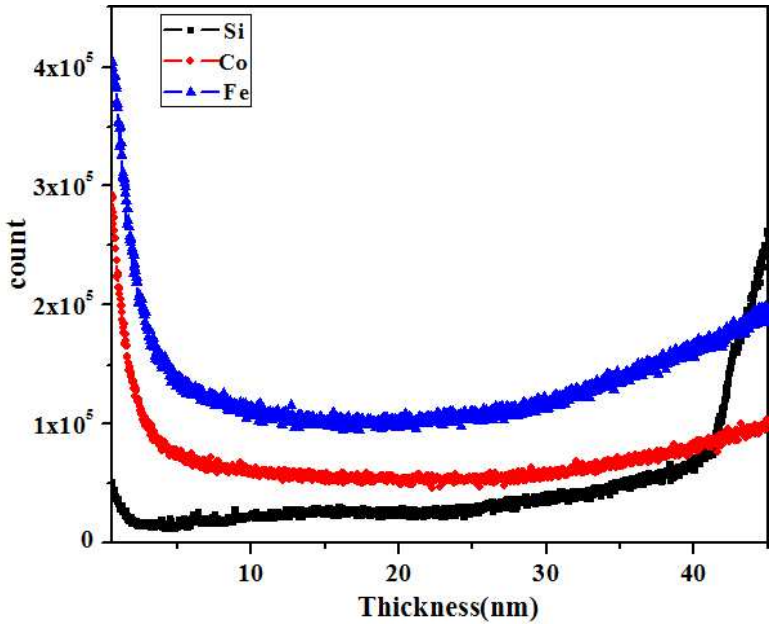

Fig. 4.4 SIMS pattern of the representative Co-Fe alloy thin film

4.3.1.2 Structural and microstructural analysis

The XRD pattern of as-deposited and annealed films recorded in grazing incidence geometry is shown in figure 4.5. It is evident that the as-deposited film is amorphous and crystallization of the films is initiated at 573 K and 673 K which resulted in a diffraction peak centered around 44°, which can be assigned to the bcc Co-Fe (110) phase (JCPDS 49-1567) [70-72]. The amorphous nature was further confirmed using selective area diffraction pattern of the films (figure 4.8). From the XPS analysis it is found that traces of oxygen are also present in the film along with Co and Fe. The presence of impurities like oxygen will increase the glass forming ability of metallic glasses which in turn can stabilize the amorphous phase in the as prepared film [56].

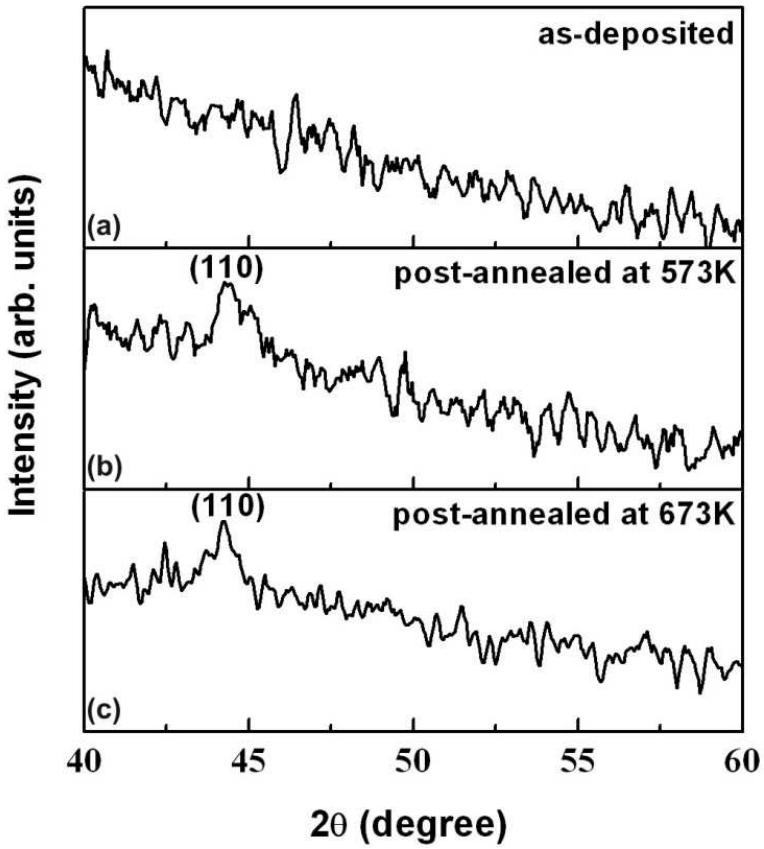

Fig. 4.5 GAXRD patterns of (a) as-deposited, (b) 573 K, and (c) 673 K annealed Co-Fe based films

The TEM images for samples annealed at 373 K, 473 K, 573 K and 673 K are shown in figure 4.6. Nanocrystallites with average grain size of ~ 6nm are clearly visible in the 473K annealed film (figure 4.6b). Upon further heat treatment the average crystallite size increases in the 673K annealed film (Figure 4.6d). It is noteworthy that a few crystallites of size ~ 19 nm were also observed in the bright field image of 673 K annealed samples along with crystallites of size~ 15 nm.

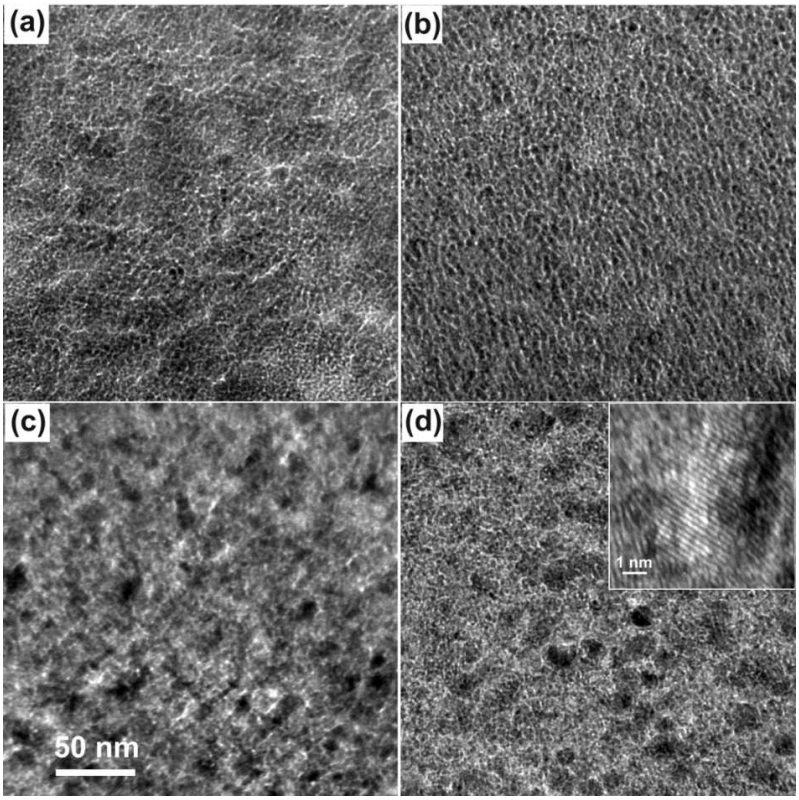

Fig. 4.6 TEM images of thin films deposited on NaCl substrates and post-annealed at (a) 373 K, (b) 473 K, (c) 573 K, and (d) 673 K. HRTEM of 673 K annealed film is shown in the inset of (d)

High resolution TEM (HRTEM) of the film annealed at 673 K is shown in the inset of figure 4.6(d). Well defined crystalline planes are visible in the micrograph. Planes observed in the HRTEM image have an average inter planar distance of 2.01 Å and the corresponding planes are identified as (110) planes of the crystalline Co-Fe phase [70-72], further supports the results of GAXRD measurements.The crystallite size distribution histograms of annealed samples are presented in figure 4.7. It is clear that as the annealing temperature increases, the grain size gradually increases. At higher annealing temperatures of 673K, the

crystallite size increases and is clearly visible in the TEM shown in figure 4.6(b). Nanocrystallites with an average grain size of (6± 0.01) nm are clearly visible in the 473K annealed film (figure 4.7(a)). Upon heat treatment the average crystallite size slowly increases and crystallites of average size (15±0.17) nm and (19±0.12) nm became clearly visible in the 673K annealed film (Figure 4.7(b)). The grain size distributions were obtained by counting the Co-Fe grains in the TEM images and are shown in figure 4.7. The histogram of size distribution shows that the number density of the nanocrystallites decreases as the annealing temperature increases which further indicates the grain growth upon thermal annealing.

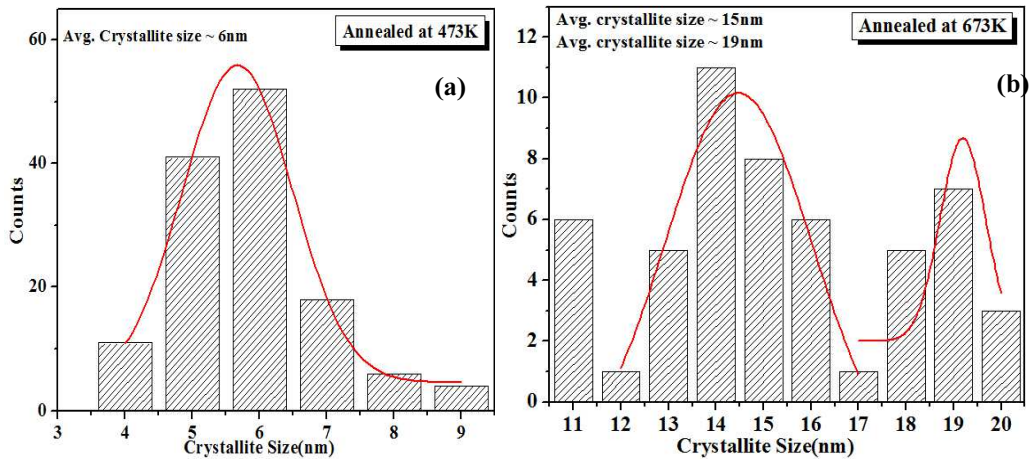

Fig.4.7 Crystallite size distribution histograms of Co- Fe thin films annealed at (a) 473K and (b) 673K

The diffused rings in the selected area diffraction pattern (figure 4.8) of the representative Co-Fe film indicate the amorphous nature of the as prepared film.

Fig. 4.8 Selected Area Electron Diffraction pattern of representative Co-Fe film

4.3.1.3 Topographical studies

AFM was used to investigate surface evolution with thermal annealing. Figure 4.9(a) shows 2x2 μm^2 AFM images acquired from the as deposited sample. Islands of lateral size around 500 nm with a height of about 40 nm are visible. Continuous and smooth morphology is observed in 573 K annealed samples with an rms roughness of about 1.2 nm (figure 4.9(d)). Statistical analysis of AFM images showed that the average roughness of the films decreased gradually from 6.6 nm for as-deposited films to 1.1 nm for films annealed at 673 K. Volume and/or surface diffusion leads to the smoothening on thermal annealing [73]. AFM line scan depicted in figure 4.9(c) and (d) clearly demonstrates the changes in film morphology on thermal annealing.

The magnetic force microscopy image of the as-deposited Co-Fe based film acquired from 2x2 μm^2 area is shown in figure 4.9(b). It can be seen that image is dominated by topographical contrast. The MFM imaging was conducted for different tip heights and in all the images no meaningful magnetic images

could be obtained. This is because of the absence of any stray magnetic fields along the out-of-plane direction. On the other hand, MFM images acquired from 573 K sample shows distinctive features of 'dark' and 'bright' contrast suggesting magnetic stray fields emanating out from the film surface (figure 4.9(e)). For magnetic thin films with an easy magnetic direction along the film plane, the stray fields are expected to be from domain boundaries.

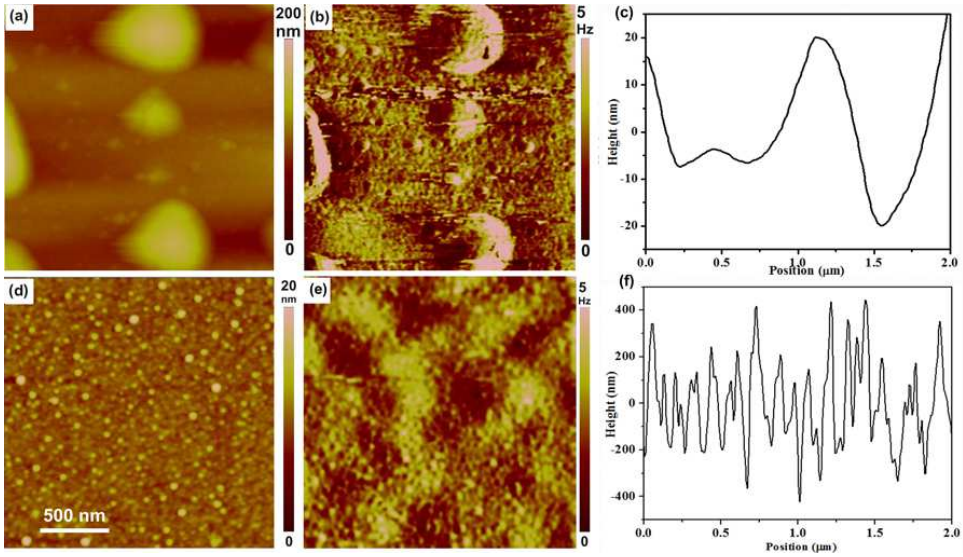

Fig. 4.9 (a) AFM & (b) MFM image and (c) line scan of as-deposited Co-Fe based thin films, (d) AFM & (e) MFM image and (f) line scan of 573 K annealed Co-Fe based thin films

Variation in the surface microstructure is clearly visible from the height profiling of the as deposited and annealed films. The thermal annealing process enhances the surface diffusion and hence makes the film surface structure more or less uniform. The surface structures present in the as deposited films get suppressed with thermal annealing.

Figure 4.10 depicts the rms roughness (R_q) variation with different annealing temperatures. The rms roughness varies in between 0.35nm to 0.57nm indicating that the thermal treatment alters the vertical features of the film. The

surface smoothening caused by the ad atom surface diffusion resulted in the decrease in surface roughness upon thermal annealing. Accordingly, the grain size estimated from TEM analysis was 15 nm after thermal annealing at 673K as compared to 6 nm in the sample heat treated at 473K.

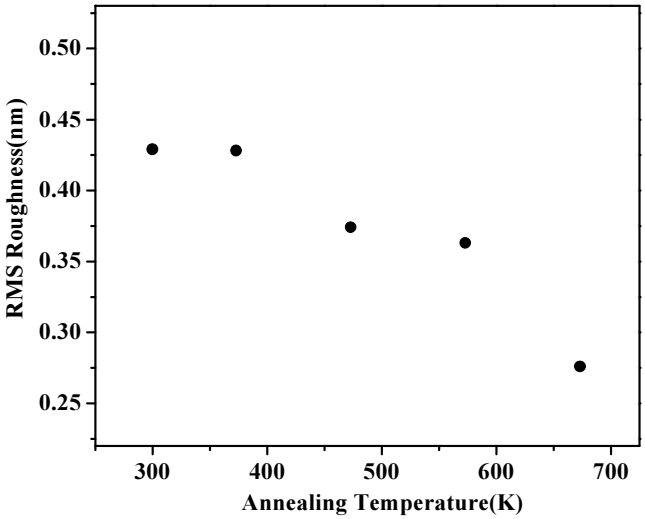

Fig. 4.10 The variation of rms roughness with annealing temperature

The information regarding the surface modifications cannot be completely extracted from the surface roughness data. Power spectral density (PSD) analysis can be used for evaluating the surface roughness both in the vertical and horizontal directions and also for determining the dominant process in surface evolution. Figure 4.11 represents the log-log plots of PSD calculated for as prepared thin film and those annealed at different temperatures. In power spectral density analysis of the Co-Fe thin films, the spatial frequency in the reciprocal space having the range 0.97 to 254 μm^{-1} was considered. The roughness of the as prepared film was higher compared to that of annealed films. In the case of as prepared films and the 373K annealed film, the PSD has two regions. The low

frequency part resembles the uncorrelated white noise, whereas the high frequency part to the correlated surface features.

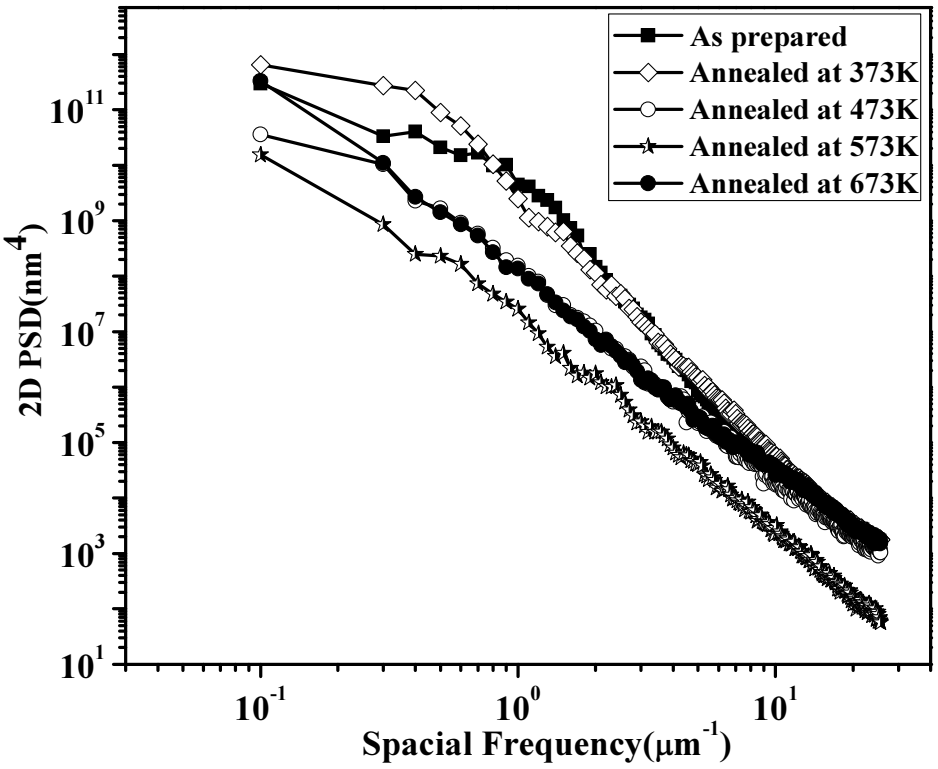

Fig. 4.11 2D PSD profiles of the as deposited and annealed Co-Fe thin films calculated from AFM measurements

The PSD curve of the as deposited film has a bump at spatial frequencies around $1\mu m^{-1}$ and this was getting shifted to the lower frequency side upon annealing at 373K. At higher annealing temperatures the curves became almost straight indicating the role of surface diffusion with annealing [73]. The linear decrease in roughness in the higher frequency region can be explained using the power law dependence (Equation 4.1).

$$PSD(k) \propto k^{-\gamma} \qquad (4.1)$$

where k represents the spatial frequency, the exponent γ is the slope of the linear part of the PSD curve which related to the growth exponent by the equation α=(γ-d)/2 [74]. Here the line scan dimension d=2 as the PSD curve is two dimensional.

The growth exponent has a value of 1.5, 1.3, 0.8, 0.95 and 0.7 respectively for the as prepared and films annealed at 373K, 473K, 573K and 673K. The lower growth exponent values points to the smoothening of surface due to surface diffusion upon thermal annealing.

4.3.1.4 Magnetization studies

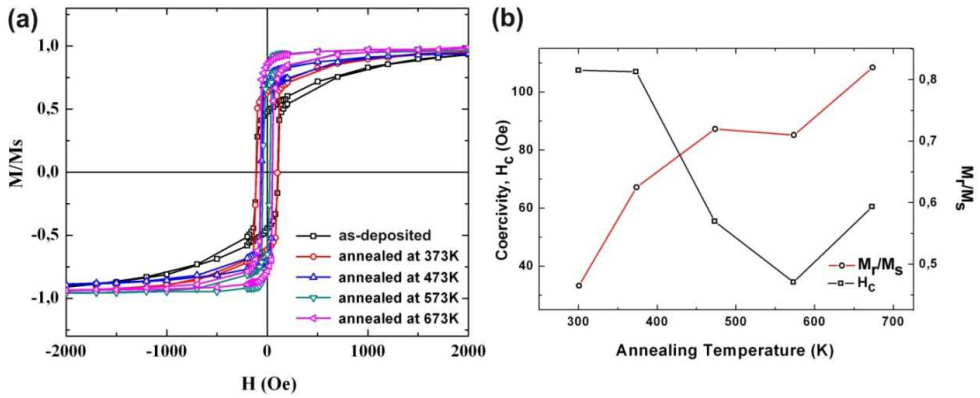

Fig.4.12 (a) Room temperature hysteresis loops of as-deposited and annealed thin film samples and (b) coercivity and remanence dependence on annealing temperature. [Solid line is a guide to the eye]

Figure 4.12(a) depicts the magnetic hysteresis loop of the as-deposited film and the films annealed at various temperatures. Saturation magnetization for the as deposited film was found to be 958emu/cc. There is a remarkable difference in the coercivity in the as-deposited and annealed thin films. The variation of coercivity and remanence (M_r/M_s) with annealing temperature is depicted in figure 4.12(b), it is evident that magnetic softening occurs at 573 K.

The gradual change in coercivity and remanence can be explained on the basis of microstructural and morphological changes in Co-Fe based thin films with thermal annealing. From TEM and AFM investigations it is seen that as-deposited films is island-like, where the magnetization reversal occurs by rotation. Coercivity of ~ 110 Oe is associated with the magneto-elastic anisotropies resulting from the rapid quenching of the films during film deposition [75]. Low remanence observed in the as deposited film indicates that the demagnetization along the in-plane direction is due to the shape of the islands. On annealing at higher temperatures, stress relaxation occurs in films, at the same time, crystallization and surface smoothening takes place. At 573 K, from the observed film morphology, it is expected that magnetization reversal is driven by a nucleation event followed by domain wall motion. This is a low energy process which is associated with low coercivity. At 673 K, the volume fraction of crystallites is expected to increase [76], which further impede domain wall motion, resulting in an increase in coercivity as well as remanence.

4.3.2 Magnetic and topographical modifications of amorphous Co- Fe thin films induced by swift heavy ion irradiation

4.3.2.1 SHI irradiation- SRIM 2006 simulation studies

The nuclear stopping power, electronic stopping power and projected range were calculated as a function of ion energy using SRIM -2006 and are shown in figure 4.13.

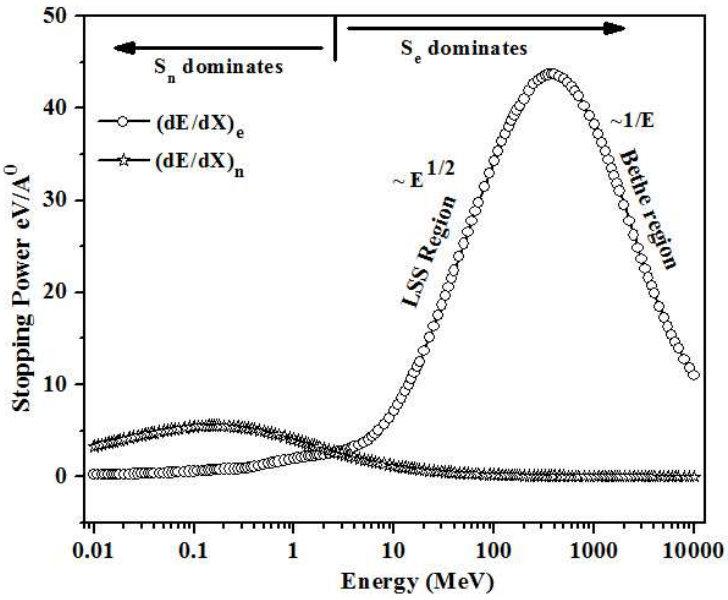

Fig. 4.13 SRIM simulation for calculating electronic and nuclear energy loss for 100 MeV Ag^{7+}ions in Co-Fe target

The simulation was done for the whole range of energies starting from 0.01MeV to 10GeV. Both S_e and S_n increase with increasing energy, reach a maximum value and then start to decrease. The peak in electronic energy loss is known as Bragg peak and the stopping power at energies below the Bragg peak is proportional to the square root of the velocity of ion (~E1/2). This is given by the LSS theory (Lindhard, Scharff and Schiøtt) [77]. At higher energies above the Bragg peak, the stopping power is proportional to (1/E) and Bethe Bloch relation [78] can be used to corroborate these results. It may be noted that the electronic energy transfer reaches its maximum values at energies higher by many orders than the nuclear stopping power maximum.

4.3.2.2 Structural and microstructural analysis

The XPS analysis of the as prepared sample confirmed that the films have a nominal composition of $Co_{77}Fe_{23}$. Figure 4.14 shows the GAXRD patterns

corresponding to pristine and irradiated films. The GAXRD analysis of the as prepared Co-Fe films shows amorphous nature. The absence of peaks in irradiated Co-Fe films points to the absence of short range order in the film after irradiation. The energy transfer to the film, with SHI irradiation locally rearranges the atomic structure of the film maintaining the amorphousity of the film. This is clearly visible from the GAXRD analysis of the irradiated film.

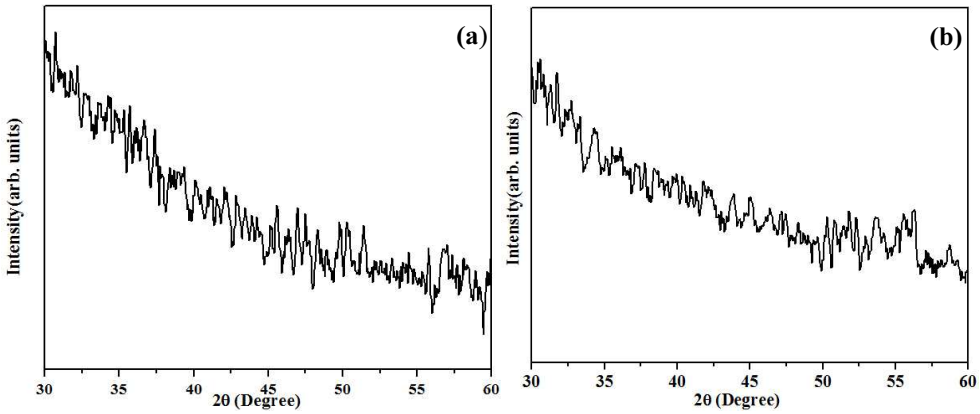

Fig. 4.14 GAXRD of Co-Fe thin film (a) pristine and (b) SHI irradiated at fluence 3×10^{13} ions/cm^2

4.3.2.3 Surface morphological studies

The surface evolution of pristine as well as irradiated Co-Fe thin film samples were visible in AFM images shown in Figure 4.15(a-e). From AFM images (figure 4.15(a)) it can be inferred that the pristine film surface contains mound-like structures which are considered to be the resultant of the island like growth involved in the vapour deposition process. Figure 4.15(b-e) shows the film surface after irradiation at ion fluences 1×10^{11}ions/cm^2, 1×10^{12}ions/cm^2, 1×10^{13}ions/cm^2 and 3×10^{13}ions/cm^2 respectively.

On close analysis of the AFM images it is clear that ion irradiation alters the surface structures found in the pristine sample. The irradiated films show damaged mounds and valleys. No track formation in the ion trajectory is visible in the surface analysis using AFM. As the irradiation dose reaches 3×10^{13}ions/cm^2, the surface shows a uniform distribution all over the scanned area. The root mean square (rms) roughness (R_{rms}) of the films can be calculated using the formula given in equation (4.2) using the standard deviation of the data obtained from AFM images.

$$R_{rms} = \sqrt{\frac{\sum_{n=1}^{N}\left(Z_n - \bar{Z}\right)^2}{N-1}} \qquad (4.2)$$

Here Z_n represents the height of the n^{th} data, Z is equal to the mean height of Z_n in AFM topography, and N is the number of the data points [79]. Dependence of ion fluence on surface roughness of pristine and SHI irradiated Co-Fe films obtained from AFM images is shown in figure 4.16(a). The rms roughness of irradiated film follows a rapid decrease followed by further decrease at still higher irradiation fluence of 3×10^{13}ions/cm^2. Surface roughness decreases with ion irradiation indicating the smoothening of the surface upon irradiation. There are many reports on surface smoothening with ion bombardment over a large range of ion energies ~keV to hundreds of MeV [80-85]. Hou *et al.* in 1990 reported that the electronic excitation and ionization due to irradiation induces rearrangement of atomic ordering and in turn plastic deformation in metallic glasses [86]. Hysen *et al.* also observed surface smoothing in ion irradiated Fe-Ni thin films [15]. They explained the surface smoothening process at lower fluences using volume diffusion mechanism. At higher fluences they observed surface roughening because of surface evaporation at elevated temperatures. Mayr and

Averback also reported similar nature of roughness with irradiation on glassy Zr-Al-Cu films [87] where radiation induced viscous flow was used to explain the dominant surface relaxation mechanism.

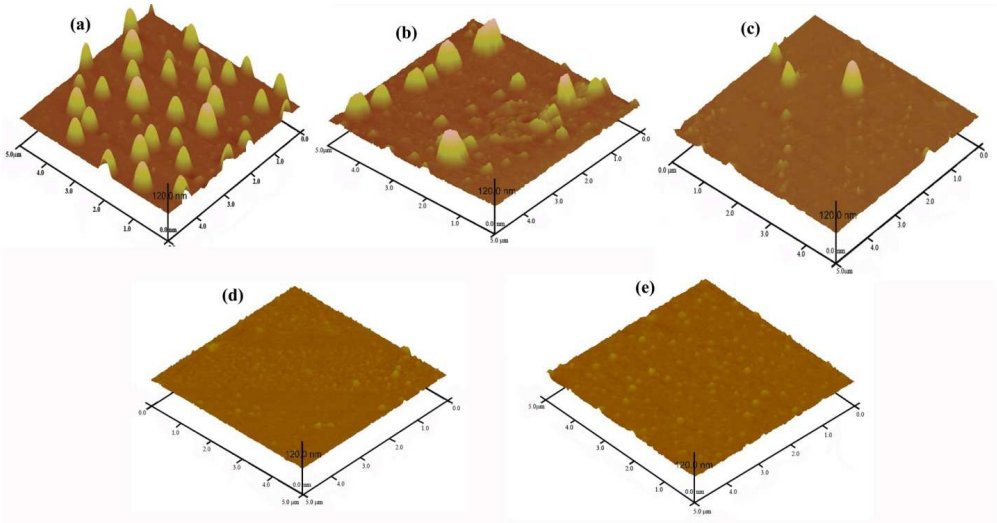

Fig. 4.15 AFM images of (a) Pristine and Irradiated Co-Fe thin films at fluence (b) 1×10^{11}ions/cm^2 (c) 1×10^{12}ions/cm^2 (d) 1×10^{13}ions/cm^2 (e) 3×10^{13}ions/cm^2

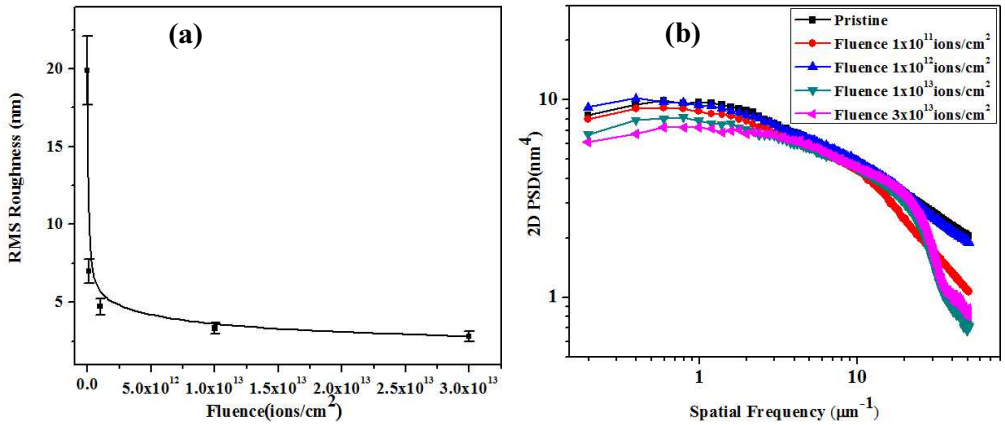

Fig. 4.16 (a) RMS roughness vs. ion fluence graph and (b) 2D PSD plot of pristine and irradiated films [Lines are guide to eye]

The interplay between the dynamics of surface roughening due to sputtering and smoothing due to material transport during surface diffusion plays an important role on the evolution of surface, during ion irradiation [81, 88-89].

Information regarding the surface modification mechanisms cannot be completely extracted from the rms surface roughness data, since it measures the roughness only in one direction. PSD analysis is an ideal tool for evaluating the surface roughness both in vertical and horizontal direction and also for determining the dominant process in surface evolution. Figure 4.16(b) represents the log-log plots of PSD calculated for pristine and irradiated thin films at various fluences.

The roughness of the pristine film was higher compared to that of irradiated films. In all cases the PSD has two regions, the low frequency part which resembles the uncorrelated white noise and the high frequency part corresponding to the surface evolution. The linear decrease in roughness in the higher frequency region can be modeled using a power law as shown in equation (4.1).

According to Herring [90], the γ values of 1, 2, 3, and 4 represents four modes of surface transport viz. viscous flow, evaporation–condensation, volume diffusion, and surface diffusion, respectively. The γ values obtained for the irradiated samples are between 0 and 2, hence the dominant surface transport mechanism seems to be a combination of viscous flow and evaporation re-condensation. The dominant surface transport mechanism for the film irradiated at fluence 1×10^{11} ions/cm^2 is irradiation induced viscous flow and that explains the rapid surface smoothening observed at that fluence. As the fluence increases to 1×10^{12}ions/cm^2 and at still higher fluences like 1×10^{13} ions/cm^2 and 3×10^{13} ions/cm^2 the dominant mechanism becomes evaporation-condensation due to the

sputtering occurring in the film during high energy ion irradiation. The roughness exponent has a value of 1.24, 1.45, 1.29, 1.92 and 1.88 respectively for the as prepared and films irradiated at fluences 1×10^{11}ions/cm^2, 1×10^{12}ions/cm^2, 1×10^{13}ions/cm^2 and 3×10^{13}ions/cm^2. The values of roughness exponent point towards the mechanism of surface evolution [84]. The calculated values of roughness exponent of the pristine and irradiated films clearly explain the surface evolution upon irradiation. Primary smoothening mechanism in the case of crystalline surfaces is found to be surface diffusion whereas that for amorphous surfaces viscous flow dominates [80]. The results obtained from surface roughness analysis are in agreement with the amorphous nature of Co-Fe films concluded from GAXRD analysis.

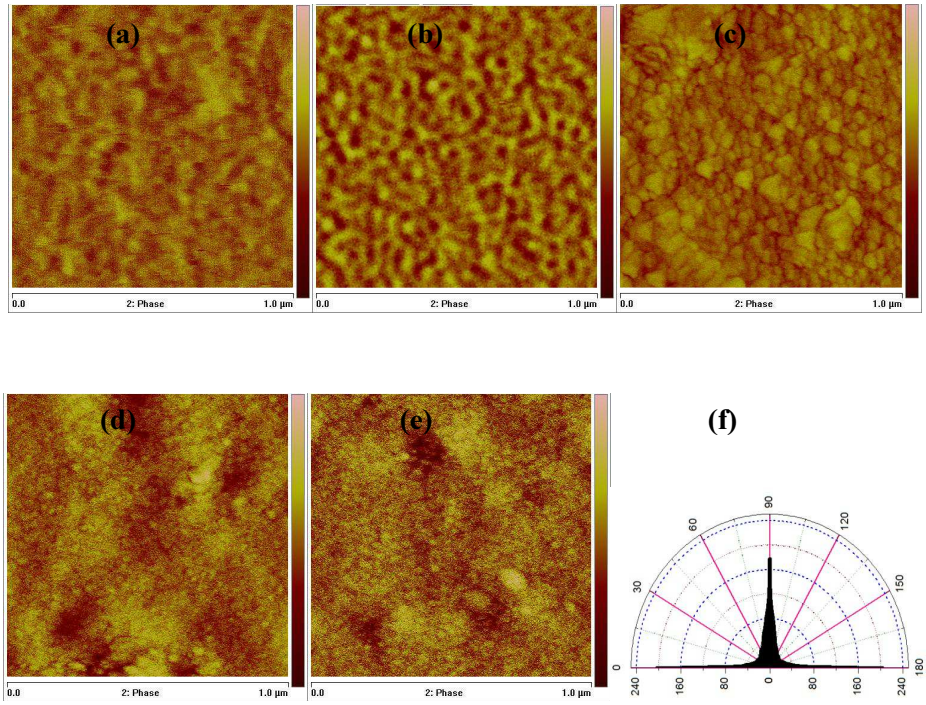

Fig. 4.17 MFM images of (a) Pristine and SHI irradiated CoFe thin films at fluence (b) 1×10^{11} ions/cm^2 (c) 1×10^{12} ions/cm^2 (d) 1×10^{13} ions/cm^2 (e) 3×10^{13} ions/cm^2 and (f) representative angular spectrum using SPIP software

Figure 4.17(a-e) shows the MFM images and corresponding angular spectrum of the pristine and irradiated (at various fluences 1×10^{11}, 1×10^{12}, 1×10^{13} and 3×10^{13} ions/cm^2) Co-Fe films with a scanning size of 1μm × 1μm. The colour contrast in the images suggests that the magnetization direction lies out of the plane of the film. Distinctive features of 'dark' and 'bright' stripe magnetic domain structure is observed in the pristine as well as irradiated samples but the contrast and domain pattern is clearly visible in the lowest irradiation dose (1×10^{11}ions/cm^2) compared to others.

By using scanning probe image processor (SPIP) (version 6.0.6) software the angular spectrum of the MFM images and the texture direction index (S_{tdi}) were calculated. Texture direction index is defined as the average amplitude sum divided by the amplitude sum of the dominating direction. It is a measure of how well the domains are aligned and the S_{tdi} value is always between 0 and 1. The arrangement of domains can be determined from the value of S_{tdi}. For well aligned domains S_{tdi} values are close to zero, while for a more or less isotropic arrangement, S_{tdi} is close to 1. For the pristine film the measured value of S_{tdi} was 0.202 and for the Ag^{7+} irradiated film, he value is 0.224. This difference reveals that the alignment of the magnetic domains was increased by the Ag-ion irradiation. This again confirms the results obtained from magnetization analysis.

4.3.2.4 Magnetization Studies

The in-plane hysteresis loops prior to and after irradiation are reported in figure 4.18. Saturation magnetization for the as deposited film was found to be 940emu/cc. Coercivity decreases at lower fluence and is maximum at a fluence of 3×10^{13}ions/cm^2. It is found that the coercive force of Co-Fe thin films are sensitive to Ag^{7+} ion irradiation and show variation with ion fluence (figure 4.19).

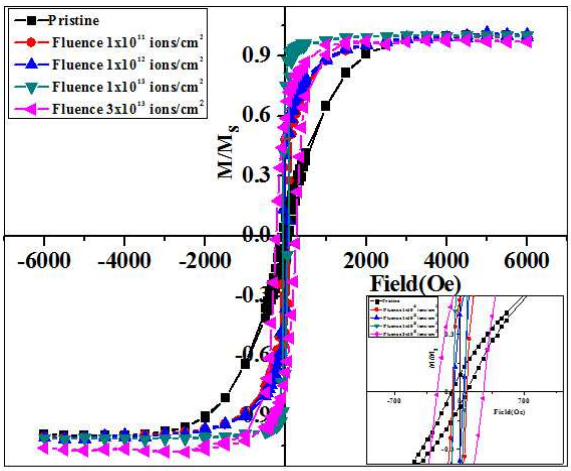

Fig. 4.18 In plane VSM hysteresis loops for the pristine and SHI irradiated Co-Fe films [Inset shows the magnified portion of the centre of hysteresis loop]

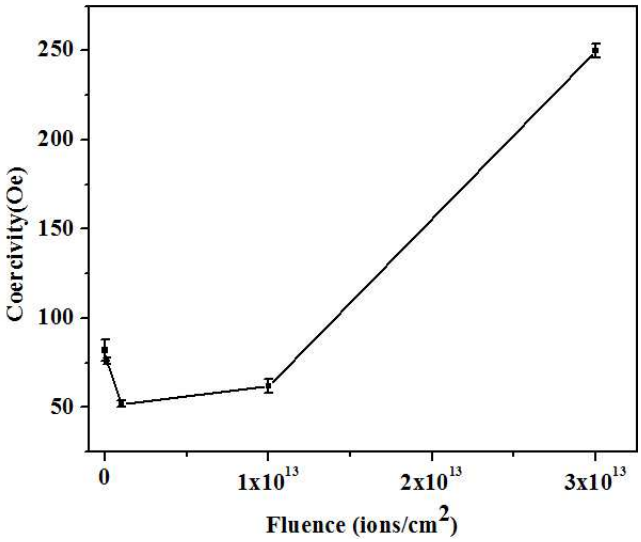

Fig. 4.19 Variation of coercivity with fluence [Lines are guide to eye]

The extrinsic magnetic properties like coercivity and remanence are sensitive to local structural properties of the films like strain, grain size, defects

etc. The modification of magnetic properties of the film after irradiation could be explained on the basis of stress and damage induced while irradiation. The coercivity obtained for different fluences decreases at lower fluences up to 1×10^{12} ions/cm^2 and afterwards increases drastically. Ion irradiation results in stress relaxation in the films, which in turn reduces the coercivity at low fluences. The energy transferred to the film during ion irradiation may alter the local atomic arrangement in the amorphous system. Along with this rearrangement there is a chance for increasing the density of the pinning centers for domains at higher fluences which might also be contributing to the observed increase in coercivity.

4.4 Conclusion

Thin films based on Co-Fe were prepared from a composite target employing thermal evaporation and subjected to thermal annealing and SHI irradiation. Post-annealing of these films resulted in nanocrystallites of Co-Fe in a residual amorphous matrix. The GAXRD and TEM investigations revealed that the onset of crystallization of Co-Fe is at around 373 K. HRTEM further confirmed this finding. Even after irradiation, the amorphous nature of the pristine film is preserved. Annealing induced modification of surface morphology of the alloy thin films were investigated by AFM. The magnetic softness of the films improved with thermal annealing but at higher annealing temperatures it was found to be deteriorating. Thermal annealing induced surface smoothening and the observed magnetic properties correlates well with surface modifications induced by thermal annealing. On annealing, crystallization together with surface smoothening influences the magnetization reversal. Magnetic measurements indicated that in as-deposited films, magnetization reversal is via coherent rotation and the demagnetizing field significantly influences the reversal processes,

whereas in films annealed at 573 K, the magnetization reversal is guided by a nucleation event followed by domain wall motion, resulting in low coercivity.

On SHI irradiation the surface roughness decreases with increase in irradiation fluence. The roughness exponent of the pristine and irradiated samples calculated from the PSD suggests that the mechanism behind the surface smoothening is viscous flow and evaporation-condensation. The VSM analysis of the pristine and irradiated samples indicated that SHI irradiation of Co-Fe samples resulted in modifications of magnetic properties. Ion irradiation results in stress relaxation in films, which in turn reduces the coercivity at low fluences. At a fluence of 3×10^{13} ions/cm^2, the density of pinning centers increases which results in enhanced coercivity. The texture direction index was used to explain the realignment of the magnetic domains upon irradiation.

References:

1 Alben R, Becker J J and Chi MC, *J. Appl. Phys*. 49 (1978) 1653

2 Nishibe Y, Yamadera H, Ohta N, Tsukada K, and Nonomura Y, *Sens. Actuators* A 82 (2000) 155

3 Hristoforou E, *Journal of Optoelectronics and Advanced Materials* Vol. 4 No. 2 (2002) 245

4 B.Y. Yoo, S.C. Hernandez, D.-Y. Park, N.V. Myung, *Electrochimica Acta* 51 (2006) `6346–6352

5 M R J Gibbs, E W Hill and P J Wright, *J. Phys. D: Appl. Phys*. 37 (2004) R237–R244

6 Hasegawa, Saito N, Saito M, Kataoka N and Fujimori H, *J. Mater. Eng. Per.*2 (1993) 181

7 J.P. Nozieres, M. Ghidini, N.M. Dempsey, B. Gervais, D. Givord, G. Suran, J.M.D. Coey; *Nucl. Instr. and Meth. In Phys. Res. B* 146 (1998) 250

8 Tetsuya Osaka, *Electr. Acta* 44, (1999) 3885

9 F. Lallemand, D. Comte, L. Ricq, P. Renaux, J. Pagetti, C. Dieppedale, P. Gaud, *Appl. Surf. Science* 225, (2004) 59

10 Andreas Moser, Kentaro Takano, David T Margulies,Manfred Albrecht, Yoshiaki Sonobe, Yoshihiro Ikeda, Shouheng Sun, Eric E Fullerton, *J. Phys. D: Appl. Phys*. 35 (2002) R157

11 D.Aurongzeb, M.Holtz, M.Daugherty, J.M.Berg, A.Chandolu, J. Yun, H. Temkin, *Appl. Phys. Lett*., 83, 26 (2003) 29

12 S. Thomas, S. H. Al-Harthi, D. Sakthikumar, I. A. Al-Omari, R. V. Ramanujan, Y. Yoshida, M. R. Anantharaman, *J. Phys. D* 41 (2008) 155009

13 Y.P.Zhao, R.M.Gamache, G.-C.Wang, T.-M.Lu, G. Palasantzas, and J. Hosson, *J. Appl. Phys.* 89 (2001) 1325

14 Senoy Thomas, Hysen Thomas, D. K. Avasthi, A. Tripathi, R. V. Ramanujan, M. R. Anantharaman, *J. Appl. Phys.*105, (2009) 033910

15 Hysen Thomas, Senoy Thomas, Raju V. Ramanujan, D.K. Avasthi, I.A. Al-Omari, Salim Al-Harthi, M.R. Anantharaman, *Nucl. Instr. and Meth. in Phys. Res. B* 287 (2012) 85

16 Clement W, Willens R H, and Duwez P, *Nature* 187 (1960) 869

17 Yoshizawa Y, Oguma S and Yamauchi K, *J. Appl. Phys.*64 (1988) 6044

18 Makino A, Suzuki K, InoueH A, Hirotsu Y and Masumoto T, *J. Magn. Magn. Mater.* 133 (1994) 329.

19 McHenry M E and Laughlin D E, *Acta. Mater.* 48 (2000) 223-238

20 Herzer G, *Physica Scripta* T 49 (1993) 307

21 Lecaude N, Perron J C, *Mater. Sci. Eng. A* 581-5 (1997) 226

22 Varga L K, Bakos E, Kisdi-Koszo E, Zsoldos E and Kiss L F, *J. Magn. Magn. Mater.* 133 (1994) 280.

23 Gupta R, Khandelwal A, Ansari R, Gupta A and Nair K G M, *Surf.coat.technol.*203 (2009) 2717

24 Mehrizi S, Sohi M H, Ebrahimi S A S, *Surf.coat.technol.* 205 (2011) 4757

25 Chen L H, Klemmer T J, Ellis K A, van Dover R B and S Jin, *J. Appl. Phys.* 87 (2000) 5858

26 Rieger G, Rupp G, Gieres G, Losehand R, Hartung W, Maass W and Ocker W, *J. Appl. Phys.* 91 (2002) 8447

27 Neudert A, McCord J, Schafer R, and Schultz L, *J. Appl. Phys.* 95 (2002) 6595

28 Fujimori H, Ohnuma S, Kobayashi N, and Masumoto T, *J. Magn.Magn. Mater.* 304 (2006) 32

29 Yu R H, Basu S, Zhang Y and Xiao J Q, *J. Appl. Phys.* 85 (1999) 6034

30 Lin Li, *J. Appl. Phys.* 79 (1996) 4578

31 Quintana P, Amano E, Valenzuela R and Irvine J T S, *J. Appl. Phys.* 75 (1994) 6940

32 O'Handley R C, Mengusar J, Sun S-W, Hara Y and Grant N J, *J. Appl. Phys.* 57 (1985) 3563

33 Betancourt I, Jim´enez M, Aburto S, Marquina V, G´omez R, Marquina M L, Ridaura R, Miki M and Valenzuela R, *J. Magn. Magn. Mater.* 140-144 (1995) 459-460

34 Bordin G, Buttino G, Cecchetti A and Poppi M, *J. Phys. D: Appl. Phys.* 30 (1997) 2163

35 Buttino G, Cecchetti A and Poppi M, *J. Magn. Magn. Mater.* 172 (1997) 147

36 Suryanarayana C, *Bull. Mater. Sci*. 17 (1994) 307

37 H.F. Li and R.V. Ramanujan, *Trans. Indian Inst. Met.* 58 (2005) 965

38 Yongmei M. J, Wang Y U, Kazaryan A, Wang Y, Laughlin D E, Khachaturyan A G, *J. Appl. Phys.* 92 No. 10 (2002) 6172

39 Sun S and Murray C B, *J. Appl. Phys.* 85 (1999) 4325

40 Puntes V F, Gorostiza P, Aruguete D M, Bastus N G, and Alivisatos A P, *Nat. Mater*. 3 (2004) 263

41 Sun S, Murray C B, Weller D, Folks L and Moser A, *Science* 287 (2000) 1989

42 Ratnesh Gupta, A Khandelwal, D K Avasthi, K G M Nair , A Gupta, *J. Appl. Phys.* 107, (2010) 033902

43 S. Klaumünzer, Hou Ming-Dong, G. Schumacher and Li Chang-Lin, *MRS Proceedings* 93 (1987)

44 D. K. Avasthi, G.K. Mehta, Springer Series in materials science, ISBN 978-94-007-1229-4 (e-book), (2011)

45 Ratnesh Gupta, G A Muller, P Schaaf, K Zhang, K P Lieb, *Nucl. Instr. And Meth. In Phys. Res. B* 216 (2004) 350

46 R L Fleischer, P B Brice, R M Walker, *J.Appl.Phys.* 36 (1965) 3645

47 E. Balanzat, J.C. Jousset, M. Toulemonde, *Nucl. Instr. And Meth. In Phys. Res. B* 32 (1988) 368

48 F Garrido, A Benyagoub, A Chamberod, J C Dran, A Dunlop, S Klaumunzer, L Thome, *Nucl. Instr. And Meth. In Phys. Res. B* 115 (1996) 430

49 Ajay Gupta, D K Avasthi, *Phys.Rev. B* 64 (2001) 155407

50 S Kavitha, V Raghavendra Reddy, Ajay Gupta, D K Avasthi, *Nucl. Instr. And Meth. In Phys. Res. B* 244 (2006) 19

51 R. L. Fleischer, P. B. Price, R. M. Walker, E L Hubbard, *Phys. Rev*. 156, (1967) 353

52 A. Iwase, S. Sasaki, T. Iwata, T. Nihira, *Phys. Rev. Lett*. 58 (1987) 2450

53 Z G Wang, C Dufour, E Paumier and M Toulemonde, *J. Phys.:Condens. Matter* 6, (1994) 6733

54 Z G Wang, C Dufour, E Paumier and M Toulemonde, *J. Phys.: Condens. Matter* 7 (1995) 2525

55 Ziegler J F, Biersack, J P, Littmark U, http://www.srim.org (1985)

56 Hua Yan, Raissa Nathania Santoso, Yueyue Jiang, Meng Heng Liang and Zhong Chen, *Thin Solid Films* 520 (2012) 2356

57 Hysen T, Deepa S, Saravanan S, Ramanujan R V, Avasthi D K, Joy P A, Kulkarni S D and Anantharaman M R, *J. Phys. D: Appl. Phys.* 39 (2006) 1993

58 Senoy Thomas, S. H. Al-Harthi, R. V. Ramanujan, Zhao Bangchuan, Liu Yan, Wang Lan, and M. R. Anantharaman, *Appl. Phys. Lett.* 94 (2009) 063110

59 Senoy Thomas, Hysen Thomas, D. K. Avasthi, A. Tripathi, R. V. Ramanujan, and M. R. Anantharaman, *J. Appl. Phys.* 105 (2009) 033910

60 Das V D and Lakshmi, *J Phys. Rev. B* 37 (1988) 720

61 Thomas S, Al-Harthi S H, Sakthikumar D, Al-Omari I A, Ramanujan R V, Yoshida Y, and Anantharaman M R, *J.Phys.D: Appl.Phys.* 41 (2008) 155009

62 T.Nishizawa, K Ishida, *Bull. Alloy Phase Diagr*. 5 (1984) 250

63 N. Fairley, http://www.casaxps.com, ©Casa software Ltd., 2005

64 Samy E O, Ayman M A, World Academy of Science, Engineering and Technology 70 (2010)

65 Moulder J F, Stickle W F, Sobol P E and Bomben K D Handbook of X-ray Photoelectron Spectroscopy ed J Chastain (MN: Perkin-Elmer Corporation) (1992) p 222

66 Shijing Wang, Boping Zhang, Cuihua Zhao, Songjie Li, Meixia Zhang, Liping Yan, *Applied Surface Science* 257 (2011) 3358-3362

67 Mark C. Biesinger, Brad P. Payne, Andrew P. Grosvenor, Leo W.M. Lau, Andrea R. Gerson, Roger St.C. Smart, *Applied Surface Science* 257 (2011) 2717

68 S. Valeri, A. Borghi, G.C. Gazzadi, A. di Bona, *Surface Science* 423 (1999) 346

69 M. Garcıa-Mendez, F.F. Castillon, G.A. Hirata, M.H. Farıas, G. Beamson, *Applied Surface Science* 161 (2000) 61

70 Ha N D, Park B C, Kim C G and Kim C O, *Phys.stat.sol.(a)* 201 No.8 (2004) 1905-1908

71 Wang X, Zheng F, Liu Z, Liu X, Wei D and Wei F, *J.Appl.Phys*.105 (2009) 07B714

72 Hua-Qiang W, Pin-Shi Y, Hong Y X, Dong M X, Bao Y G, Xian W W, *J Mater Sci* 41 (2006) 6889

73 Junhua X, Lihua Y, and Isao K, *J. Appl. Phys*. 94 (2003) 6827

74 E.A. Eklund, E.J. Snyder, R.S. Williams, *Surf. Sci*. 285 (1993) 157

75 Giselher H , *J. Magn. Magn. Mater* 112 (1992) 258

76 Tsai C S, Yang W J, Leu M S and Lin C S, *J. Appl. Phys*. 70 No. 10 (1991) 5846-5848

77 J. Lindhard, M. Scharff and H.E. Schiott, *Mat. Fys. Medd. Dan. Vid. Selsk.* 33 (1963) 14

78 F. Bloch, *Z. Phys*., 81 (1933) 363

79 Fuxiang Cheng, Zuoyan Peng, Zhigang Xu, Chunsheng Liao, Chunhua Yan, *Thin Solid Films* 339 (1999) 109

80 E. Chason, T.M. Mayer, B.K. Kellerman, D.T. McIlroy, A.J.Howard, *Phys. Rev. Lett*. 72 (1994) 3040

81 G. Carter and V. Vishnayakov, *Phys. Rev. B* 54 (1996) 17647

82 K. Wittmaack, Practical Surface Analysis, Vol. 2 *Ion and Neutral Spectroscopy*, edited by D. Briggs and M. P. Seah ,Wiley, Chichester, (1992), Chap. 3, p. 122

83 E.A. Eklund, R. Bruinsma, J. Rudnick, R.S. Williams, *Phys. Rev. Lett*. 67 (1991) 1759

84 J. Krim, I. Heyvart, D.V. Haesendonck, Y. Bruynseraede, *Phys. Rev. Lett*. 70 (1993) 57

85 A. Gutzmann, S. Klaumunzer, P. Meier, *Phys. Rev. Lett*. 74 (1995) 2256

86 Ming-dong Hou, S. Klaumunzer, G Schumacher, *Phys. Rev. B* 41 (1990) 1144

87 S.G. Mayr, R.S. Averback, *Phys. Rev. Lett.* 87(2001) 196106

88 S. Jay Chey, J.E. Van Nostrand, D.G. Cahill, *Phys. Rev.* B 52 (1995) 16696

89 D. K. Goswami, B. N. Dev, *Phys. Rev. B* 68 (2003) 033401

90 C. Herring, *J. Appl. Phys*. 21 (1950) 301

CHAPTER 5

LEAD FREE HETEROGENEOUS MULTILAYERS BASED ON Co–Fe WITH GIANT MAGNETO ELECTRIC COUPLING FOR MICROELECTRONICS/MEMS APPLICATIONS

Geetha Pookat et al., J. Appl. Phys. 114, 064309 (2013)

5.1 Introduction

Multiferroic materials which display both ferroelectric and ferro/ferrimagnetic characteristics are currently a hot topic of research owing to their tremendous application potential in functional devices [1, 2]. However, single-phase compounds that exhibit ferroelectric as well as ferro/ferrimagnetic properties, known as multiferroic materials, are very rare, and their magneto-electric response is very weak at room temperature, which renders them useless from a device point of view [3]. New composite structures were proposed for the engineering of materials with improved magnetoelectric coupling properties. Magneto electric coupling in such composite structures is an independent phenomenon. Research on this product property [4-10] of magneto-electric materials mainly focuses in optimizing the piezoelectric and magnetostrictive components for enhancement in the ME coupling values. Nan et al. reported the magneto-electric effect occurring in different configurations like T-T (transverse magnetization and polarization), L-L (longitudinal magnetization and polarization), L-T and other combinations {like L-L (push-pull) longitudinal vibrations; L-T unimorph and bimorph bending and C-C (circumferential magnetization and circumferential polarization)vibration modes} of lead zirconate titanate (PZT) and lead magnesium niobate-lead titanate (PMN-PT) as the piezoelectric phase and terfenol-D as the magnetostrictive phase [5]. These laminates show giant magneto-electric voltage coefficients in the range of 5.9 to 30.8V/cm.Oe [6-10]. It was shown that this ME output can be increased by usually one or two orders of magnitude if the laminates are driven in mechanical resonance with frequency in several tens of kilohertz range [10, 11]. A general drawback of such laminates is that terfenol-D requires quite large magnetic bias

fields of around 400–500Oe for operation in the maximum of the magnetostrictive susceptibility for very high ME coefficients. To overcome this drawback a material with saturation magnetostriction in low applied dc magnetic fields is ideal for applications. A magneto electric composite with a magnetic material having low saturation magnetic field can deliver high magnetoelectric outputs at low dc applied magnetic fields which makes them cost effective and efficient. Also investigations on lead free ME composites with a strong ME response is important from an application point of view.

Recently much more interest was drawn towards the ME composites involving Metglas as the magnetic component. There are reports on an extremely high ME voltage coefficient of 22 V/cm.Oe at 1Hz and about 500 V/cm Oe at resonance at 22 kHz for a 2–1 Metglas/PZT-fiber composite [12]. A giant ME coupling of 7.2 V/cm.Oe at 1 kHz and of 310 V/cm.Oe at resonance of around 50 kHz was reported in a composite with highly permeable Metglas ribbon that was glued on a polyvinylidene fluoride foil with a high piezoelectric voltage coefficient [13]. Intermetallic magnetic alloys having soft magnetic properties are another important class of materials that can be used in ME composites. They possess square loop characteristics (M_r/M_s~1) with high permeability and also their saturation magnetization and coercivity can be tuned by alloy composition, annealing process etc in such materials [14-16].

Giant values of ME coupling was reported in bulk composites fabricated either by mixing the magnetic material to a piezoelectric matrix or by gluing the individual components. In spite of the fascinating properties exhibited by these bulk composites, they could not be used in applications like magnetoencephalography and magnetocardiography which require spatial

resolution by sensor arrays and detection of low frequency signals below 1 KHz. For fabricating such ME sensor arrays with higher resolution, small, identical and low frequency resonant ME sensors are required which can only be achieved through microelectromechanical (MEMS) systems techniques [17]. Thin films on substrates are often thought inferior due to their large in-plane clamping with the substrate. However, Greve et.al reported a remarkably giant magneto-electric coupling in thin film magnetoelectric 2-2 structures consisting of AlN (aluminum nitride) and amorphous $(Fe_{90}Co_{10})_{78}Si_{12}B_{10}$ layers with thickness more than several micrometers. In that particular thin film heterostructures, ME coupling obtained was as high as 3.1V/cm.Oe out of resonance (100 Hz) and 700 V/cm.Oe at resonance (753 Hz). However, there was a substantial drop in the ME coupling coefficient at biasing magnetic fields above 20 Oe [17]. Such multilayer structures are easier to fabricate compared to 3-1 bulk composites and is expected to be far superior to bulk composites in terms of magneto-electric coupling since the P-E layer can easily be poled electrically to enhance the piezoelectricity and the ME effect. The 2-2 type configuration overcomes the leakage problem as the ferroelectric layers shut off the circuit and this could lead to a visible ME effect [18].

In this investigation we have fabricated magneto-electric 2-2 layers based on Barium Titanate (BTO) – CoFe (Alloy) - Barium Titanate [BTO-CoFe-BTO] multilayer structures on silicon substrates. Barium titanate being a room temperature ferroelectric material exhibits good ferroelectric and piezoelectric properties along with excellent mechanical and chemical stabilities [19]. Intermetallic magnetic alloys of cobalt and iron are an important class of materials from a technological stand point as they have high initial permeability, and the magnetic field needed for saturation of magnetostriction is much lower than that

in ferrites and other ferromagnetic metals. High magnetostriction is a preferred parameter of a magnetic material to be chosen in magneto electric systems as it will bring an appreciable hike in MECC values. Hence we have adopted a soft magnetic alloy of Co-Fe in this particular multilayer structure. The multilayer structure opted here reduce the substrate clamping effect for the CoFe-BTO layer due to another BTO layer deposited close to the substrate. For device applications, miniaturization of thin films and integration with silicon technology is essential and are often preferred to their thick films/layered counterparts. Here we have employed a $Si/SiO_2/Ti/Pt$ substrate, such a material is a common selection, as far as integration with ferroelectrics is concerned [20].

5.2 Experimental Techniques

5.2.1 Fabrication of BTO-CoFe-BTO Multilayers

Sol-gel spin coating technique was adopted for the preparation of BTO layers by employing barium acetate ($Ba(C_2H_3O_2)_2$), and titanium isopropoxide ($Ti\{OCH(CH_3)_2\}_4$) dissolved in 2-methoxy ethanol ($C_3H_8O_2$) as precursor material. The sol derived from the reaction was homogenized by thorough stirring for 6 hours and subjected to subsequent ultrasonication and ageing for 72 hours. A programmable spin coater was used to deposit the sol on chemically and ultrasonically cleaned substrates at a speed of 6000 rpm. The prepared films were pyrolyzed at 250°C for 30 minutes and finally annealed at 700°C for 1 hour under an oxygen atmosphere. Physical vapour deposition technique was employed for deposition of Co-Fe layer on the prepared BTO layer. Commercially available Co-Fe alloy ribbon (Cobalt rich) was used for film deposition at room temperature at a pressure of 10^{-6} Torr. Another BTO layer was deposited on the top of the Co-Fe film to passivate the Co-Fe alloy layer from oxidation. 2-2 heterostructures of BTO-CoFe-BTO were coated on a $Si/SiO_2/Ti/Pt$ substrate. These thin films were

etched at the corner with 5%HCl+HF solution so as to open the Pt electrode for taking electrical contacts. For ME coupling studies, gold was sputtered on top of the surface BTO layer and lead contacts were soldered. Figure 5.1 shows the concept of a sandwich structure prepared for ME coupling measurement.

Fig. 5.1 Schematic of the prepared multilayer structure for ME coupling studies

5.2.2 Characterization Techniques

The structural, microstructural, surface and elemental characterizations of the fabricated samples were carried out by employing X-Ray diffraction (XRD) along with transmission electron microscopy (TEM), atomic force microscopy (AFM), scanning electron microscopy (SEM) and energy dispersive X-ray spectrometry (EDAX). The microstructural evolution of the films was investigated by means of TEM and experiments were carried out in a Jeol JEM-2200 FS electron microscope operated at 200 kV. Morphology and cross section of the films were profiled by using scanning electron microscope (HR-SEM marca Hitachi, model SU-70). The elemental analysis was done using an EDAX (marca Bruker, model QUANTAX 400). For elemental analysis of the alloy composition, thin films were simultaneously coated over glass and silicon substrates (bare substrates without a layer of BTO). The surface morphology of the as prepared and annealed CoFe films was imaged using AFM. All imaging were carried out at

the following conditions: AFM multimode instrument, using higher resolution magnetic force microscopy tips (MESP-HR) purchased from Bruker at resonant frequency of 475 Khz, MFM at a lift height of 10 nm and scan rate of 0.5 kHz and resolution of 512 pixel. The AFM images were further investigated using NanoScope v7.0 software. Magnetic measurements were carried out in a Quantum Design MPMS 5XL SQUID Magnetometer. Magnetic hysteresis loops were recorded and the loop parameters like coercivity, remanence and saturation magnetisation were evaluated. Ferroelectric hysteresis loops were used for analyzing ferroelectric properties. The ferroelectric properties of the prepared multilayers were studied using ferroelectric test system (TF analyzer 1000). Magneto electric coupling measurements were used to determine the ME coupling coefficient.

5.3 Results and Discussion

5.3.1 Structural and Microstructural Analysis

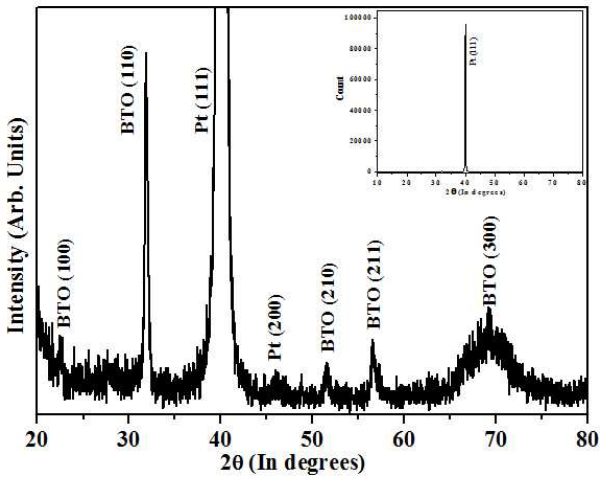

Fig. 5.2 X-ray diffraction pattern of the BTO thin film on platinum substrate

The XRD pattern of the as prepared BTO sol deposited Pt substrate is shown in figure 5.2. The XRD pattern indicates that BTO corresponds to a perovskite structure.

The broad diffraction peaks point towards the formation of small crystallites in the film upon annealing at 700^0C. An average crystallite size of ~39 nm was obtained using Scherrer formula by taking account of the peak broadening at (110) diffraction line [21].

The microstructure of the middle Co-Fe layer was examined by TEM and is depicted in figure 5.3. TEM of the magnetic alloy layer shows the formation of a homogeneous layer consisting of nanosized magnetic grains with very low surface roughness. Annealing of multilayer initiates the formation of nanocrystallites in the middle CoFe layer and the grain size of the nanocrystallites are very small, of the order of 4-5 nm. Inset of figure 5.3 shows the HRTEM of the post annealed CoFe alloy (recorded before the deposition of the surface BTO layer). (110) plane of CoFe is clearly visible in the HRTEM. Here the grain size evaluation of CoFe alloy becomes more relevant as it is important in understanding the magnetic and magnetostrictive properties of this alloy. Also magnetostriction is often observed to be higher for nanoparticles than their micron sized counterparts [22].

Figure 5.4 depicts the SEM of the BTO-CoFe-BTO multilayer structure. Figure 5.4(a) depicts the top view of the annealed BTO film. Uniform grain growth with low surface roughness is clearly visible. Even though we have used an inexpensive technique of sol gel spin coating, it has not deteriorated the surface quality of these thin films.

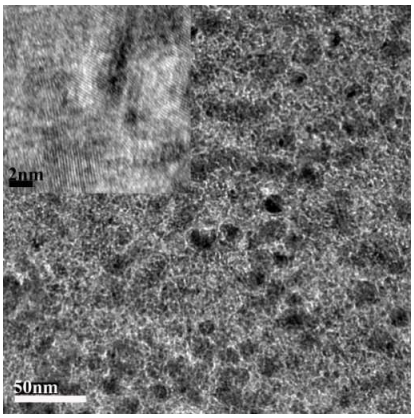

Fig. 5.3 TEM of CoFe thin films (HRTEM image of annealed film is shown in the inset)

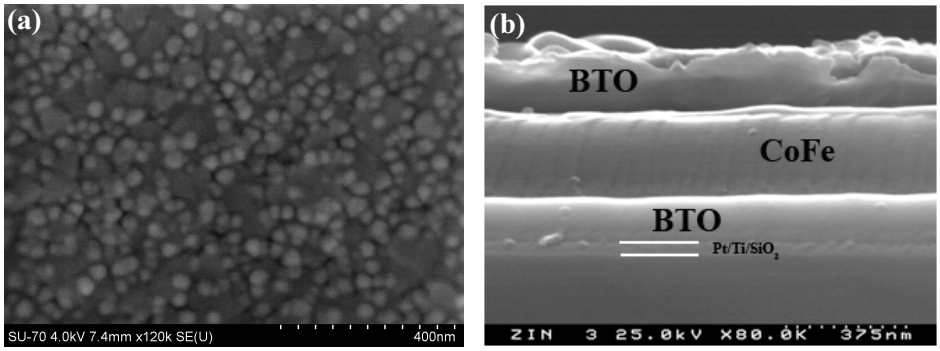

Fig. 5.4 SEM images of BTO-CoFe-BTO multilayer films on Pt/Ti/SiO_2/Si substrate (a) top-view and (b) cross-section view

The grain size calculated from SEM images is around 35-40 nm, which is in agreement with the grain size obtained from XRD. Also we have probed these multilayer structures through SEM to observe the cross- sectional view in order to determine the thickness of the sandwiched structure as well as the individual layers. Cross sectional SEM images of the BTO-CoFe-BTO layers are provided in Fig.5.4 (b). Individual layer thickness calculated from the micrograph are ~ 150, 260, 150 nm, respectively for the BTO, CoFe, BTO layers. Here we have kept the thickness of the BTO layer high in order to avoid any possible electrical short circuit on the evaporation of middle (CoFe layer) and top (Au top electrode) metal layer.

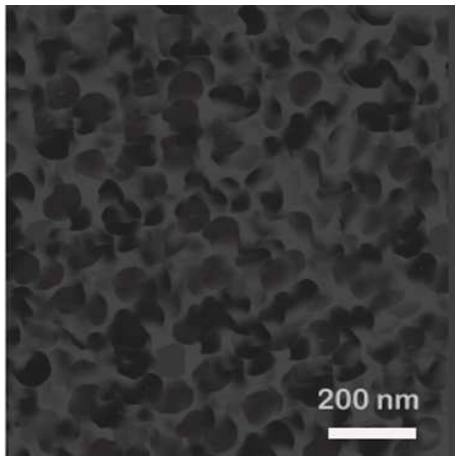

Fig. 5.5 TEM image from the top BTO-CoFe-BTO layer

Figure 5.5 shows the top view TEM of the BTO-CoFe-BTO multilayer. This image again confirms that the average grain size of barium titanate formed is around 40 nm.

5.3.2 Topographical Analysis

Middle CoFe layer was analyzed through atomic force microscopy (AFM) and the topography and line profile is provided in figure 5.6. The statistical analysis of the AFM image shows that the roughness of the film is ~ 1.2nm. The smoothness of the film is evident from the line scan too.

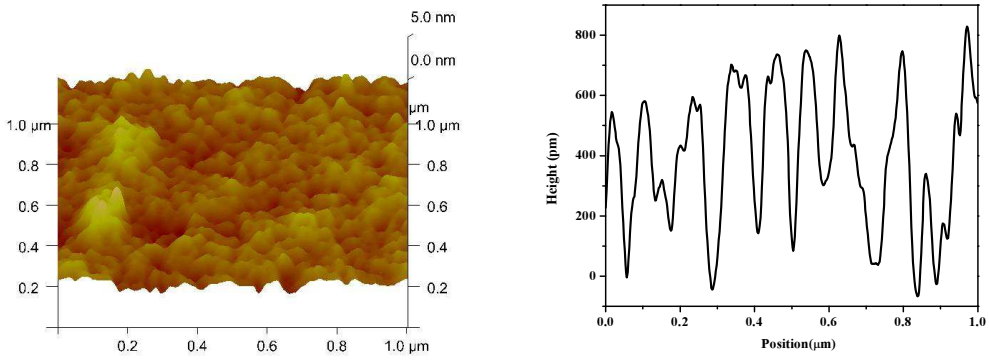

Fig. 5.6 Topography of the CoFe layer (AFM micrograph) and the line profile

5.3.3 Elemental Analysis

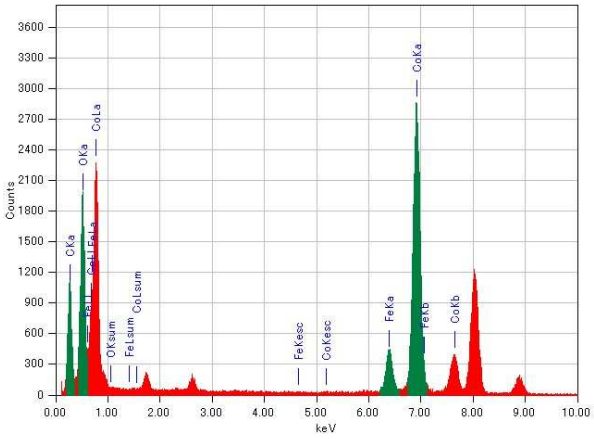

Fig. 5.7 EDAX Spectrum of the CoFe (magnetic alloy) thin film

In order to obtain the elemental composition of the magnetic alloy, the alloy films were simultaneously deposited over chemically and ultrasonically cleaned silicon substrates. Figure 5.7 depicts the elemental analysis and semi quantification of the CoFe alloy layer coated over NaCl substrates using EDS. It shows that the middle CoFe layer has a composition of Co 77% and Fe 23%. It may be noted here that the elemental composition determines the magnetic and magnetostrictive properties that influences the magneto electric coupling.

5.3.4 Magnetization Studies

The magnetic measurements were carried out by employing a SQUID magnetometer. The results show that the films exhibit saturation magnetisation of 1175emu/cc (Fig. 5.8) which is quite substantial. A very high squareness ratio (M_r/M_s = 0.9) and low coercivity (~ 88Oe) is retained in the CoFe alloy deposited by thermal evaporation technique.

The magnetic structure of the CoFe alloy layer is also examined by magnetic force microscopy (MFM). The magnetic force microscopic image of the annealed CoFe films having scan size 2μm x 2μm is shown in figure 5.9.

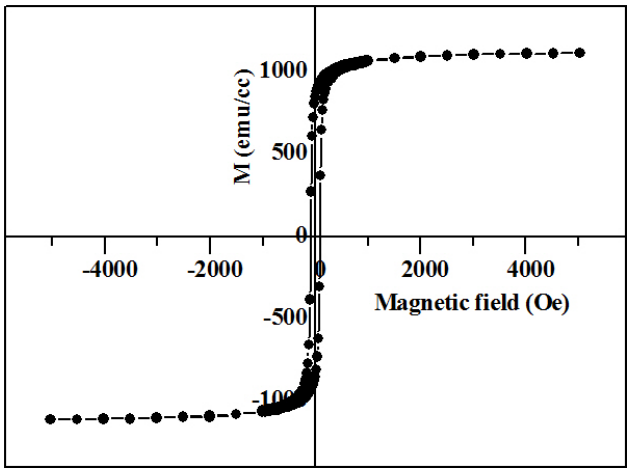

Fig. 5.8 Magnetic hysteresis loop for a BTO-CoFe-BTO multilayer

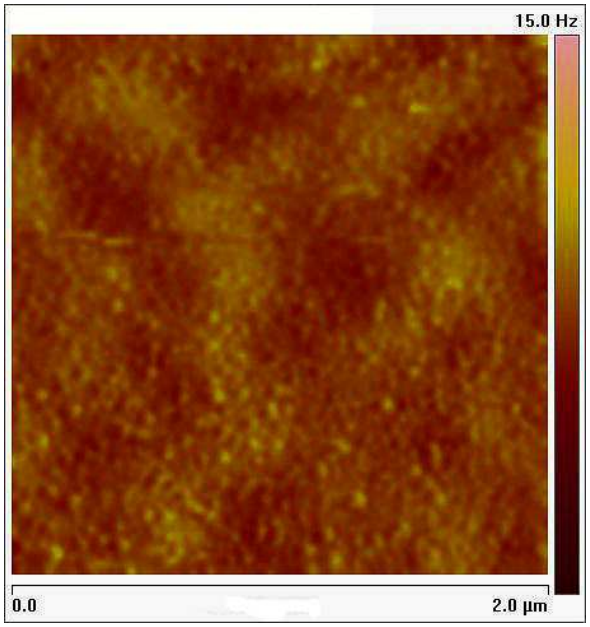

Fig. 5.9 MFM image of post annealed CoFe middle layer

It shows that the individual alloy nanograins deposited are magnetic in nature. Distinctive features of 'dark' and 'bright' contrast suggesting magnetic stray fields emanating out of the film surface can be noticed.

5.3.5 Ferroelectric Characterization

Figure 5.10 shows a well defined ferroelectric hysteresis loop, with a saturation polarization, PS≈6.7μC/cm^2, and a remnant polarization Pr≈3.3μC/cm^2. Here the electric coercive field was 6.1kV/cm. The reported P_S value for a single crystal is around 25μC/cm^2 and for ceramics it is 19μC/cm^2 [23, 24]. Size of the grains or crystallites in the films could be playing a vital role in determining the polarizations of these structures. [25].

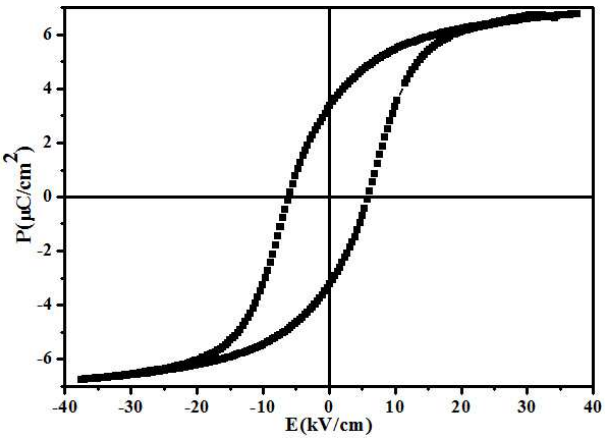

Fig. 5.10 Room temperature P-E Hysteresis loop of BTO-CoFe-BTO multilayer

5.3.6 Magnetoelectric Coupling Studies

We have adopted magnetoelectric coupling measurements in the passive mode in order to avoid the erroneous contributions from magneto resistance and interfacial polarizations (magneto capacitance measurements is the direct method). However, in this indirect method, there can be contributions from the generated induced EMF. The real magneto electric coupling signal is a sinusoidal

function of frequency, and hence is almost linear in low frequency regime, but goes to static at high frequencies, while the induced EMF signal grows more rapidly. Similarly other stray signals can arise which could overestimate the measured ME coupling constant [20].

ME coupling studies were first performed over plane $Si/SiO_2/Ti/Pt$ substrates followed by the BTO coated $Si/SiO_2/Ti/Pt$ substrates to avoid the contributions from other static and stray signals. The obtained signal was set as the reference signal for subtraction. Dc magnetic field dependence was studied both in the longitudinal and transverse mode. Transverse measurement mode is the one where the polarization and magnetic field vectors are perpendicular to each other (Magnetic field in plane to the sample, voltage measured perpendicular to the sample, so that polarization and magnetic field vectors are perpendicular). Similarly, in the longitudinal mode, polarization and magnetic field vectors are parallel to each other (Magnetic field perpendicular, voltage measured perpendicular to the sample again, so that polarization and magnetic field vectors are parallel).

Figure 5.11 shows that a maximum ME coupling of 5.503 V/(cm.Oe) (transverse) and 3.115 V/(cm.Oe) longitudinal) was recorded for the BTO-CoFe-BTO (single layer each) at a dc biasing field of 18 Oe at 500 Hz. A sharp resonance is observed at a frequency of 975 Hz with a giant ME coupling coefficient of 944 V/(cm.Oe) (transverse) (figure 5.12) and 478 V/(cm.Oe) (longitudinal) in the frequency dependence study of the ME coupling at a dc magnetic field of 18 Oe.

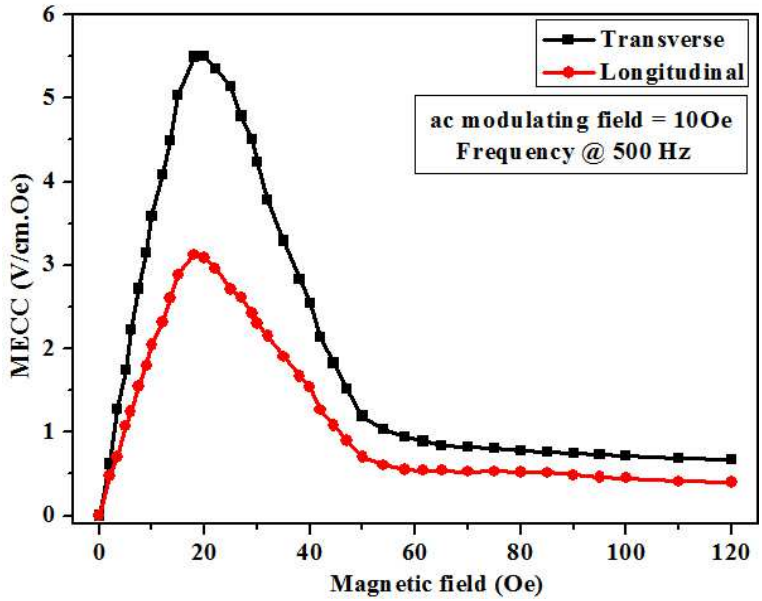

Fig. 5.11 DC biasing field dependence of the MECC measured @ 500 Hz (Peak coupling @ H_{dc}=18Oe)

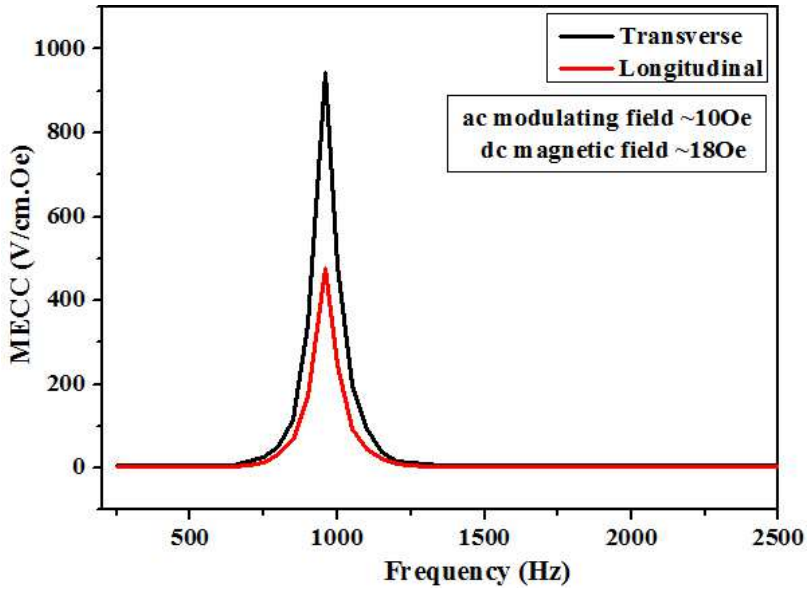

Fig. 5.12 Low-frequency resonance in the transverse and longitudinal mode

The obtained value is a bit higher than 746 V/(cm.Oe) reported for Metglas-AlN multilayers [17]. The resonance frequency of a cantilever with different resonance modes n can be determined using equation 5.1 [26].

$$f_n = \frac{1}{4\pi}\frac{\lambda_n^2}{L_1^2}\sqrt{\frac{\hat{E}_1 h_1^3}{3\left(\sum_n \rho_n h_n\right)}} \tag{5.1}$$

Here n is the mode order, L and h are the length and thickness of the cantilever, λ_n is a dimensionless parameter, ρ is the density of the material. n=1 for the substrate material and for the films on the cantilever n=2, 3,…. $\hat{E}$ is the effective Young's modulus. The calculated value for the first order resonance using above equation was 1045Hz which is closer to the obtained experimental value of resonant frequency 975Hz. Frequency dependent studies show that the transverse MECC is 5.503, 5.681, 7.664, 9.932 and 53.354 V/(cm.Oe) for 500 Hz, 2.5kHz, 5kHz, 10kHz and 100kHz respectively. These measurements were done at a relatively low dc applied field of 18Oe with an ac modulating field of ~10Oe. The off resonance values obtained were nearly close to the highest reported values of MECC in 2-2, 2-1 and 3-0 ME heterostructures. In this multilayer structure, the generated voltages are in millivolts range while it is less than 1 microvolt in all other samples employed for comparison.

According to magnetoelectric equivalent circuit [27] the ME voltage coefficient can be written as (equation 5.2)

$$\alpha_{ME} = \frac{n d_{33,m} d_{31,p}}{n\varepsilon_{33}^S s_{11}^E + (1-n)s_{33}^H\left(\varepsilon_{33}^S + d_{31,p}^2 / s_{11}^E\right)} \tag{5.2}$$

where n is the magnetic phase thickness ratio, s_{11}^{E} and s_{33}^{H} are the elastic compliances of the piezoelectric and magnetostrictive layers, respectively, ε_{33}^{S} is the dielectric constant of the piezoelectric material at constant strain, and $d_{33,m}$ and $d_{31,p}$ are the longitudinal piezomagnetic and transverse piezoelectric coefficients respectively. From this equation, it is clear that, a middle magnetic layer with a higher magnetostriction can result in a high strain in the nearby piezoelectric layers which will result in an enhanced magneto electric coupling. Hence, a very high magnetostriction becomes the primary requirement for the selection of the magnetic material for magneto electric applications. Recently, Hunter et.al reported that a cobalt rich alloy with Fe having a particular composition (or rather within a range of varying cobalt composition) attains giant magnetostriction upon annealing [28]. In this particular report, the giant magnetostriction was recorded when the percentage of cobalt in CoFe alloy was maintained in between 60 to 75%. The alloy composition employed in the present study closely matches with the above mentioned one. The high initial permeability and the high magnetostriction developed in the CoFe layer upon annealing is believed to contribute to the giant MECC observed in the system consisting of BTO- CoFe –BTO multilayers. Further investigations like measurement of magnetostriction and permeability before and after annealing, frequency dependence of permeability, frequency dependence of the dielectric constant etc. are necessary to understand in detail the underlying physics and model the ME effects for such alloy based ME systems.

The grain sizes of magnetic alloys are another parameter that plays an important role in the giant magneto electric coupling exhibited by these multilayer

structures. Here the particle size ratio of ferroelectric to magnetic component is about 10 (comparing TEM, HRTEM and SEM).

Let us explain the physical scenario as follows. Each ferroelectric grain corresponds to almost 10 magnetic grains. Owing to the large surface to volume ratio of the magnetic grains, magnetic dipole dominance occurs at the layer boundaries. This surface effect contributes to the giant magneto electric coupling in such multilayer structures [29]. The charge redistribution induced by the interfacial boundaries of the ferroelectric layer may induce changes in ferromagnetic ordering as per the polarization direction and thereby contributing to giant magnetoelectric coefficient [30].

5.4 Conclusion

The magnetoelectric properties of the BTO-CoFe-BTO multilayer structures were investigated. The giant MECC values obtained were explained on the basis of high magnetostriction of the middle CoFe layer which in turn increases the strain developed over upper and lower BTO layers. Also the large surface to volume ratio of ferromagnetic and ferroelectric layers contributes to the giant ME coupling. The charge redistribution induced in the interfacial boundaries of the ferroelectric layer also would be enhancing the MECC values.

References:

1. H. Schmid, *Ferroelectrics* 162, (1994) 317
2. W. Eerenstein, N. D. Mathur, J. F. Scott, *Nature* (London) 442, (2006) 759
3. W. Prellier, M. P. Singh, and P., Murugavel, *J. Phys.: Condens. Matter* 17, (2005) R803
4. C. W. Nan, *Phys. Rev. B* 50, (1994) 6082
5. C. W. Nan, M. I. Bichurin, S. Dong, D. Viehland, G. Srinivasan, *J. Appl. Phys.* 103, (2008) 031101
6. J. Ryu, S. Priya, A. V. Carazo, K. Uchino, H. E. Kim, *J. Am. Ceram. Soc*. 84, (2001) 2905
7. S. X. Dong, J. F. Li, D. Viehland, *J. Appl. Phys*. 95, (2004) 2625
8. J. Y. Zhai, Z. Xing, S. X. Dong, J. F. Li, D. Viehland, *Appl. Phys. Lett*. 88, (2006) 062510
9. S. X. Dong, J. F. Li, D. Viehland, *IEEE Trans. Ultrason. Ferroelectr. Freq. Control*. 51, (2004) 794
10. S. X. Dong, J. Y. Zhai, F. Bai, J. F. Li, D. Viehland, *Appl. Phys. Lett*. 87, (2005) 062502
11. S. X. Dong, J. Y. Zhai, N. G. Wang, F. M. Bai, J. F. Li, D. Viehland, T. A. Lograsso, *Appl. Phys. Lett.* 87, (2005) 222504

12. S. X. Dong, J. Y. Zhai, J. F. Li, D. Viehland, *Appl. Phys. Lett*. 89, (2006) 252904

13. J. Zhai, S. Dong, Z. Xing, J. Li, D. Viehland, *Appl. Phys. Lett*. 89, (2006) 083507

14. S. Thomas, H. Thomas, D. K. Avasthi, A. Tripathi, R. V. Ramanujan, M. R. Anantharaman, *J. Appl. Phys.* 105, (2009) 033910

15. S. Thomas, S. H. Al-Harthi, R. V. Ramanujan, B. Zhao, Y. Liu, L. Wang, M. R. Anantharaman, *Appl. Phys. Lett*. 94, (2009) 063110

16. G. Pookat, H. Thomas, S. Thomas, S.H. Al-Harthi, L. Raghavan, I.A. Al-Omari, D. Sakthikumar, R.V. Ramanujan, M.R. Anantharaman, *Surface & Coatings Technology* 236 (2013) 246

17. H. Greve, E. Woltermann, H. J. Quenzer, B. Wagner, E. Quandt, *Appl. Phys. Lett*. 96, (2010) 182501

18. G. Srinivasan, E. T. Rasmussen, J. Gallegos, R. Srinivasan, Yu. I. Bokhan,V. M. Laletin, *Phys. Rev. B* 64, (2001) 214408

19. F. Jona, G. Shirane, *Ferroelectric Crystals*, Dover Publications Inc.,New York, 1993

20. G. R. Fox, S. Trolier-McKinstry, S. B. Krupanidhi, L. M. Casas, *J. Mater. Res.* 10(6), (1995) 1508

21. M. C. Wang, F. Y. Hsiao, C. S. Hsi, N. C. Wu, *J. Cryst. Growth* 246, (2002) 78

22. G. Balaji, R. A. Narayanan, A. Weber, F. Mohammad, C. S. S. R. Kumar, *Mater. Sci. Eng., B* 177, (2012) 14

23. C. A. Samara, *Phys. Rev*. 151, (1966) 378

24. H. B. Sharma, A. Mansingh, *IEEE Proceedings of ISAF* (1994) 457

25. L. Huang, Z. Chen, J. D. Wilson, S. Banerjee, R. D. Robinson, I. P. Herman, R. Leibowitz, S. O'Brien, *J. Appl. Phys.* 100, (2006) 034316

26. F. Lochon, I. Dufour, D. Rebière, *Sens. Actuators B* 108, (2005) 979

27. J. Zhai, S. Dong, Z. P. Xing, J. Li, D. Viehland, *Appl. Phys. Lett*. 89, 083507 (2006)

28. D. Hunter, W. Osborn, K. Wang, N. Kazantseva, J. H. Simpers, R. Suchoski, R. Takahashi, M. L. Young, A. Mehta, L. A. Bendersky, S. E. Lofland, M. Wuttig, I. Takeuchi, *Nat. Commun*. 2, (2011) 518

29. G. V. Duong, R. Groessinger, *J. Magn. Magn. Mater.* 316, (2007) 624

30. T. N. Narayanan, B. P. Mandal, A. K. Tyagi, A. Kumarasiri, X. Zhan, M. G. Hahm, M. R. Anantharaman, G. Lawes, P. M. Ajayan, *Nano Lett.* 12, (2012) 3025

CHAPTER 6

ROOM TEMPERATURE MAGNETO ELECTRIC COUPLING IN $SrTiO_3$–CoFe– $SrTiO_3$ MULTILAYERED THIN FILMS

Geetha Pookat et al., (submitted to Euro Physics Letters)

6.1 Introduction

Research interest on magnetoelectric materials increased dramatically in recent years on account of the additional degree of freedom in device designing. The ability to control magnetic properties by an electric field and vice versa raises exciting possibilities for potential technological applications in various fields such as in microelectromechanical systems (MEMS) industry, magnetic field assisted energy harvesters, switching devices and storage applications etc [1,2]. Magnetoelectrics gives rise to an easy method for transduction from magnetic to electrical signals. Various configurations of ferro or piezoelectric and ferromagnetic materials are thoroughly investigated for possible magnetoelectric coupling properties [3-8]. The strong mechanical coupling between the ferromagnetic/ ferroelectric layer causes change in piezoelectric/ferromagnetic properties of the ferro/piezoelectric layer [9]. In the present investigation we have adopted CoFe as the ferromagnetic component and the $SrTiO_3$ (STO) as the ferroelectric component.

$SrTiO_3$ is well known for its incipient ferroelectric nature when synthesized in its pure unstressed form [10]. It retains its paraelectric properties down to 0K and also exhibit large permittivity values at very low temperatures. This ferroelectric stability gets destroyed in STO generally due to antiferrodistortion and quantum fluctuations [11-12]. Investigations on STO indicates that this delicate balance between paraelectricity and ferroelectricity can be easily destroyed by external parameters like doping with specific cations [13], substituting oxygen isotopes [14], applying electric fields [15] or using strain engineering techniques [10,16-18]. There are certain reports on room temperature ferroelectricity in epitaxial STO films subjected to a compressive or tensile strain [9-10, 19]. Recently, room temperature ferroelectricity was observed in STO films

grown on STO (001) substrates [11]. Zhong et.al reported that vacancy-type defects could induce room temperature ferroelectricity in tetragonal STO thin films [12]. Haeni et.al showed that the epitaxial strain originating from the substrate material can cause an enhancement in T_c and can produce room temperature ferroelectricity in $SrTiO_3$ [10]. Kim et al. in 2010 reported room temperature ferroelectricity in tensile strained STO thin films grown on $GdScO_3$(110) substrates. Their findings point towards the fact that both defects and strain could lead to room temperature ferroelectricity in STO thin films [20]. There are many reports with Terfenol-D as the magnetostrictive phase and ferroelectric materials like lead zirconate titanate (PZT) or lead magnesium niobate- lead titanate (PMN-PT) as the piezoelectric phase [3]. However, the lead component in such structures is undesirable and hence alternative nontoxic ferroelectric materials such as $BaTiO_3$ and $SrTiO_3$ have been receiving considerable importance [21, 22]. But $SrTiO_3$ thin films have smaller remnant polarizations than those of PZT materials [23]. Patil *et al.* reported a large ME voltage coefficient of about 560μV/cm.Oe for $NiFe_2O_4$-$Ba_{0.7}Sr_{0.3}TiO_3$ composite [24]. There are many other reports of magneto electric coupling in BSTO based ceramics and composites [25-26].

In this work, we fabricate a STO-CoFe-STO multilayer thin film structure consisting of sol-gel derived $SrTiO_3$ and thermal evaporated Co-Fe layers on $Si/SiO_2/Ti/Pt$ substrate. Here the incipient ferroelectric nature of STO was explored by mechanically coupling it with ferromagnetic CoFe thin films. The high initial permeability and giant magnetostriction makes CoFe as an ideal candidate for the ferromagnetic phase in such heterogeneous magnetoelectric systems. Also for Intermetallic magnetic alloys like Co-Fe, the magnetic field

needed for the saturation of magnetostriction is much lower than that in ferrites and other ferromagnetic metals.

6.2 Experimental Techniques

6.2.1 Preparation of STO-CoFe-STO multilayers

STO sol was prepared via sol gel synthesis using precursors consisting of strontium nitrate ($Sr(NO_3)_2$), titanium isopropoxide ($Ti\{OCH(CH_3)_2\}_4$) and 2-methoxy ethanol ($C_3H_8O_2$). The prepared sol was homogenized after thorough stirring for 6 hours and ultrasonicated and kept for ageing for 72 hours. A programmable spin coater was used to deposit the homogenized sol on ultrasonically and chemically cleaned Pt coated Si substrates at a speed of 6000 rpm. As-prepared STO film was pyrolyzed under oxygen atmosphere at 250°C for 30 minutes and later annealed at 700°C for 1 hour. Thermal evaporation technique (at room temperature) was used to deposit commercially available CoFe alloy ribbon (Cobalt rich) onto a STO layer at a pressure of 10^{-6} Torr. Spin coating technique was again employed to deposit a STO layer on top of the CoFe films. Different layers of multilayer films were etched out at the corner with 5%HCl+HF solution so as to open the Pt electrode. Gold was sputtered on top of the surface STO layer as the second electrode, and lead contacts were soldered for the ME coupling studies. The schematic of the multilayer thin film structure along with top Au electrode coated for ferroelectric/ magnetoelectric measurements is shown in figure 6.1. Bottom STO layer reduces the possibility of substrate clamping of ferromagnetic CoFe layer substantially thereby results in maximum magnetostriction in ferromagnetic layer and strain in top STO layer.

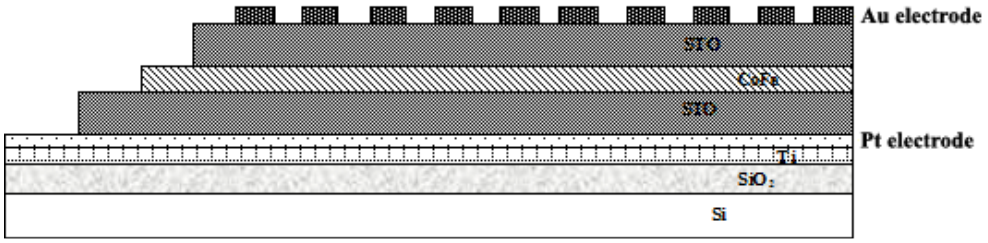

Fig. 6.1 Schematic of multilayer structure with top electrode

6.2.2 Characterization techniques

The multilayer structures were characterized using X-ray diffraction, scanning electron microscopy (HR-SEM marca Hitachi, model SU-70), transmission electron microscopy (Joel JEM-2200 FS), quantum design MPMS 5XL SQUID magnetometery and ferroelectric loop tracer technique (TF analyzer 1000). The magneto electric coupling were evaluated by a homemade setup that consists of an electromagnet and a pair of Helmholtz coils that generate the dc bias field and the ac driving field, respectively, extended with a lock-in amplifier (Model: DSP 7270). The frequency dependence was studied at 28 Oe dc magnetic field, ~10Oe ac modulating field (from 500Hz to 1.5kHz). LabVIEW automated system was used for data acquisition. The off-resonant ME coupling coefficient was determined at room temperature as a function of the biasing dc magnetic field by measuring the ME voltage developed when a low frequency (500 Hz) magnetic field with an amplitude of ~10 Oe was applied to the thin film cantilevers. The low modulation frequency of 500 Hz was chosen as the starting frequency to avoid contributions from resonance effects. Frequencies less than 500 Hz were not applied in order to avoid the interfacial polarization effects and high losses usually present at very low frequencies. Frequency dependence was studied from 500 Hz to 1.5kHz range.

6.3 Results and Discussion

6.3.1 Structural and microstructural analysis

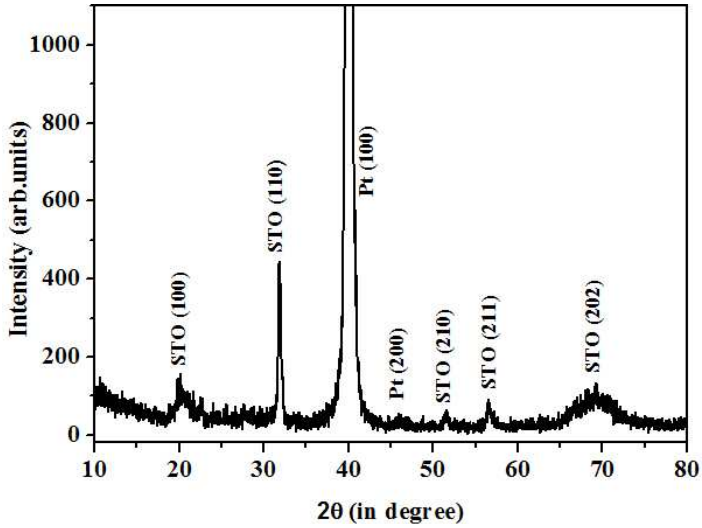

Fig. 6.2 XRD pattern of the STO-CoFe-STO multilayer structure on platinum substrate

Figure 6.2 represents the XRD pattern of STO-CoFe-STO multilayers structure. Peaks corresponding to cubic $SrTiO_3$ were indexed in the figure 6.2 (JCPDS 35-0734). Along with the $SrTiO_3$ phase substrate peaks corresponding to Pt were also present in the pattern. Broad diffraction peaks are indicative of the nanophasic structure of $SrTiO_3$. Lattice constant determined using XRD data was found to be 3.906Å which is in agreement with the reported value in ICDD (International Centre for Diffraction Data). Average crystallite size was calculated to be ~22nm using Scherrer formula by taking the broad peak at (110) diffraction line.

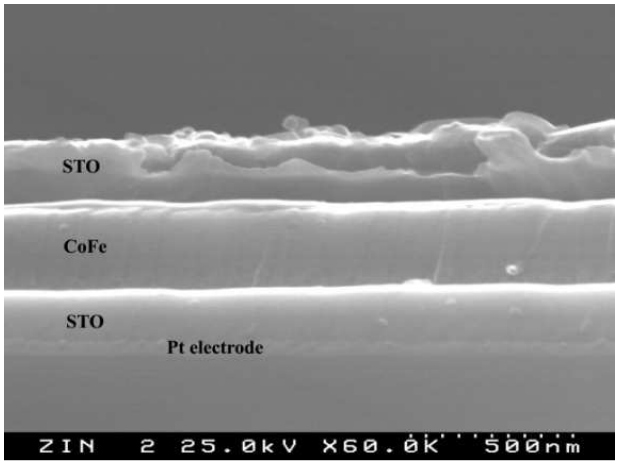

Fig. 6.3 Cross-section SEM image of STO-CoFe-STO multilayer films on Pt/Ti/SiO2/Si substrate

Figure 6.3 depicts the cross sectional SEM of the multilayer structure. Thickness of the individual layers in the heterogeneous multilayer structure can be found out by analyzing this image. The thickness of each layers in the multilayer structure were found to be 180nm, 240nm, 180nm for the top STO, CoFe and bottom STO layers respectively.

Determination of the elemental composition assumes importance as they determine the magnetic and magnetostrictive. They also influence the magnetoelectric coupling. We have adopted X-ray photoelectron spectroscopic (XPS) analysis to confirm the composition obtained from EDS analysis and it was found to be 77%Co and 23%Fe.

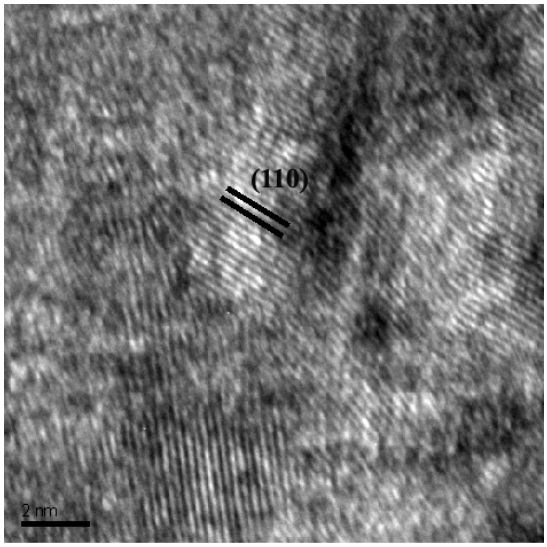

Fig. 6.4 HRTEM image of CoFe middle layer in the STO-CoFe-STO multilayer structure

The high resolution transmission electron microscopic (HRTEM) images (recorded before the deposition of the top surface STO layer) were used to determine the phase formation occurred during annealing of multilayer structure. (110) planes of CoFe were identified from the HRTEM which acts as the magnetic phase in the multilayer structure. The HRTEM image of the middle Co-Fe layer is shown in figure 6.4.

6.3.2 Magnetization studies

Magnetic hysteresis loop for the STO-CoFe-STO multilayer is shown in figure 6.5 from which the coercivity is found to be 69Oe and saturation magnetization as 832 emu/cc. High saturation magnetization and low coercivity of Co-Fe soft magnetic alloy is maintained in the multilayer with a high squareness ratio (0.82).

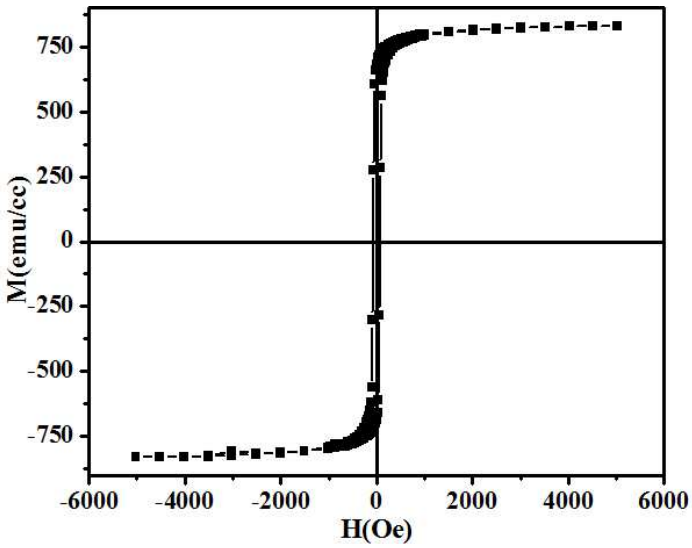

Fig. 6.5 Magnetic hysteresis loop for a STO-CoFe-STO multilayer

6.3.3 Ferroelectric measurements

Figure 6.6 shows the ferroelectric (P-E) hysteresis loop recorded for STO-CoFe-STO multilayer at room temperature. The P-E loop shows that the films are mildly ferroelectric exhibiting closed loops at room temperature [27]. For an electric field of 12kV/cm, a polarization of around 1.5μC/cm^2 is observed. The banana-like shape of the polarization hysteresis loop indicates a strongly resistive contribution [28]. This may be attributed to the overall incipient ferroelectric like contribution from the larger grains. The remanent polarization ($2P_r$) and the coercive electric field ($2E_c$) obtained from the ferroelectric hysteresis loops are about 1.14μC/cm^2 and 7kV/cm respectively. The lower values of P_r and E_c can be explained on the basis of intrinsic size effect in low dimensional ferroelectric materials [29].

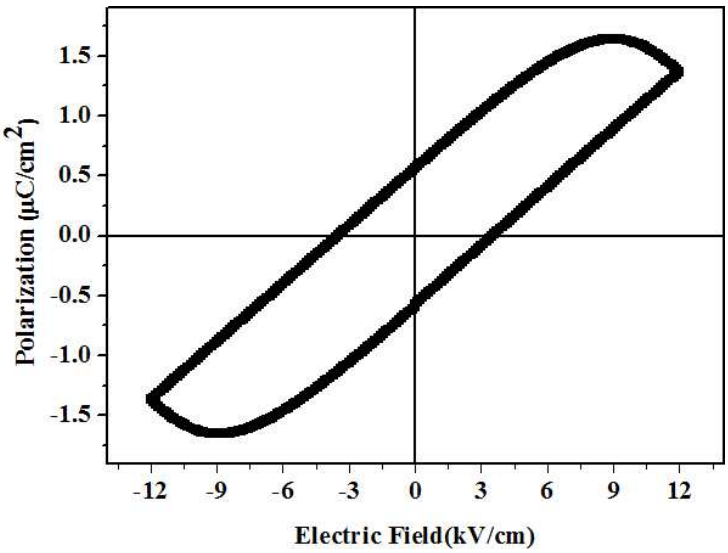

Fig. 6.6 Room temperature P-E loop of STO-CoFe-STO multilayer structure

6.3.4 Magneto electric characterization

Dc magnetic field dependence of MECC was studied in the multilayer structure. A maximum MECC of 806mV/cm.Oe was recorded at a dc biasing field of 28Oe as shown in figure 6.7(a). MECC values were recorded for different frequencies in the ME coupling set up and are shown in figure 6.7(b). The frequency dependence of the ME coupling at a dc magnetic field of 28Oe shows a sharp resonance peak at 753Hz with a MECC of 20V/cm.Oe.

According to the magnetoelectric equivalent model proposed by Zhai et al.,[30]

$$\alpha_{ME} = \frac{n d_{33,m} d_{31,p}}{n\varepsilon_{33}^{s} s_{11}^{E} + (1-n) s_{33}^{H} \left(\varepsilon_{33}^{S} + {d_{31,p}^{2}}/{s_{11}^{E}} \right)} \qquad (6.1)$$

where n is the magnetic phase thickness ratio, s_{11}^{E} and s_{33}^{H} are the elastic compliances of the piezoelectric and magnetostrictive layers, respectively, ε_{33}^{S} is the dielectric constant of the piezoelectric material at constant strain, and $d_{33,m}$ and $d_{31,p}$ are the longitudinal piezomagnetic and transverse piezoelectric coefficients respectively.

This equation clearly points out that the high magnetostriction of the middle magnetic layer result in a large strain in the upper and lower piezoelectric layers which in turn enhances the magnetoelectric coupling in the multilayer structure. The ferromagnetic layer composition used in this multilayer structure is with composition $Co_{77}Fe_{23}$ which is close to the composition reported recently by Hunter et al. as the one with giant magnetostriction [31].

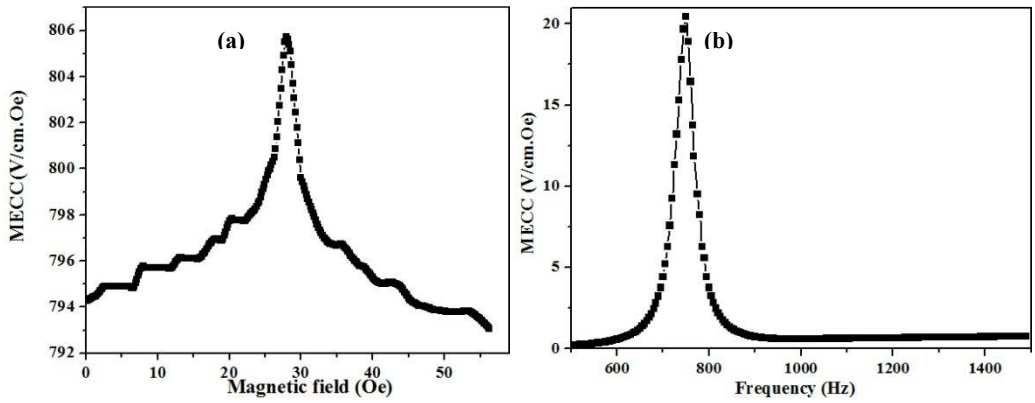

Fig. 6.7 (a) MECC variation with magnetic field and (b) MECC vs. frequency graph for STO-CoFe-STO multilayer

6.4 Conclusion

In summary, the employment of $Co_{77}Fe_{23}$ composition with giant magnetostriction in combination with incipient ferroelectric material strontium titanate (STO) resulted in the achievement of a ME coupling of 20V/(cm.Oe) at 753Hz. The STO-CoFe-STO multilayers with a total layer thickness of ~ 600nm

were deposited on silicon-based substrates, which is ideal from the miniaturization and silicon integrated device point of view. The high initial permeability of CoFe made the ME coupling so high despite of substrate clamping. The easy and cost effective synthesis techniques (sol-gel/spin coating and physical vapour deposition by thermal evaporation) make these multilayers industrially favourable.

References:

1. H. Schmid, *Ferroelectrics,* 162 (1994) 317
2. W. Eerenstein, N. D. Mathur, J. F. Scott, *Nature,* 442 (2006) 759
3. C. W. Nan, M. I. Bichurin, S. Dong, D. Viehland, G. Srinivasan, *J. Appl. Phys.* 103 (2008) 031101
4. J. Ryu, S. Priya, A. V. Carazo, K. Uchino, H. E. Kim, *J. Am. Ceram. Soc*. 84 (2001) 2905
5. S. X. Dong, J. F. Li, D. Viehland, *J. Appl. Phys*. 95 (2004) 2625
6. J. Y. Zhai, Z. Xing, S. X. Dong, J. F. Li, D. Viehland, *Appl. Phys. Lett*. 88, (2006) 062510
7. S. X. Dong, J. F. Li, D. Viehland, *IEEE Trans. Ultrason. Ferroelectr. Freq. Control*. 51 (2004) 794
8. S. X. Dong, J. Y. Zhai, F. Bai, J. F. Li, D. Viehland, *Appl. Phys. Lett.* 87, (2005) 062502
9. G.A. Smolenski, I.E. Chupis, *Sovt. Phys. Usp*. 25 (1982) 475
10. J. H. Haeni, P. Irvin, W. Chang, R. Uecker, P. Reiche, Y. L. Li, S. Choudhury, W. Tian, M. E. Hawley, B. Craigo, A. K. Tagantsev, X. Q. Pan, S. K. Streiffer, L. Q. Chen, S. W. Kirchoefer, J. Levy, D. G. Schlom, *Nature* 430, (2004)7 58
11. H. Unoki, T. Sakudo, *J. Phys. Soc. Jpn*. 23, (1967) 546
12. W. Zhong, D. Vanderbilt, *Phys. Rev. Lett.* 74, (1995) 2587
13. T. Mitsui, W. B. Westphal, *Phys. Rev*. 124, (1961) 1354
14. M. Itoh, R. Wang, Y. Inaguma, T. Yamaguchi, Y. J. Shan, T. Nakamura, *Phys. Rev. Lett*. 82, (1999) 3540
15. P. A. Fleury, J. M. Worlock, *Phys. Rev*. 174, (1968) 613

16. N. A. Pertsev, A. K. Tagantsev, N. Setter, *Phys. Rev. B* 61, (2000) R825
17. K. J. Choi, M. Biegalski, Y. L. Li, A. Sharan, J. Schubert, R. Uecker, P. Reiche, Y. B. Chen, X. Q. Pan, V. Gopalan, L. Q. Chen, D. G. Schlom, C. B. Eom, *Science* 306, (2004) 1005
18. Y. S. Kim, D. H. Kim, J. D. Kim, Y. J. Chang, T. W. Noh, J. H. Kong, K. Char, Y. D. Park, S. D. Bu, J. G. Yoon, J. S. Chung, *Appl. Phys. Lett.*86, (2005) 102907
19. M P Warusawithana, C Cen, C R Sleasman, J C Woicik, Y Li, L F Kourkoutis, J A Klug, H Li, P Ryan, L P Wang, M Bedzyk, D A Muller, L Q Chen, J levy, D G Schlom, *Science* 324/5925 (2009) 367
20. Y S Kim, J. S. Choi, J. Kim, S. J. Moon, B. H. Park, J. Yu, J.-H. Kwon, M. Kim, J.S. Chung, T. W. Noh, J.G. Yoon, *Appl. Phys. Lett.* 97, (2010) 242907
21. Swapna S. Nair, Geetha Pookat, Venkata Saravanan, M. R. Anantharaman, *J. Appl. Phys*. 114, (2013) 064309
22. W J Maeng, I Jung, J Y Son, *Solid State Communications* 152 (2012) 1256-1258
23. Y S Kim, D J Kim, T H Kim, T W Noh, J S Choi, B H Park, J G Yoon, *Appl. Phys.Lett*.91/4 (2007) 042908
24. D. R. Patil, B. K. Chougule, *J Mater Sci: Mater Electron*., 20 398 (2009)
25. T. Bonaedy, K.M. Song, K.D. Sung, N. Hur, J.H. Jung, *Solid State Communications* 148 (2008) 424-427
26. J. E. Mancilla, , J. N. Rivera, C. A. Hernández, M. G. Zapata, *J. Aus. Cer. Soc.* 48, (2012) 223
27. H H Nwe, Y M Maung, T T Win, *Universities Research Journal*, Vol. 4, No. 4 (2011)

28. V. V. Lazenka, M. Lorenz, H. Modarresi, K Brachwitz, P Schwinkendorf, T B¨ontgen, J Vanacken, M Ziese, M Grundmann, V V Moshchalkov, *J. Phys. D: Appl. Phys.* 46, (2013) 175006
29. D. Zhou, H. Gu, Y. Hu, H. Tian, Z. Wang, Z. Qian, Y.Wang, *J. Appl. Phys.* 109, (2011) 114104
30. J. Zhai, S. Dong, Z. P. Xing, J. Li, D. Viehland, *Appl. Phys. Lett*. 89, (2006) 083507
31. D. Hunter, W. Osborn, K. Wang, N. Kazantseva, J. H. Simpers, R. Suchoski, R. Takahashi, M. L. Young, A. Mehta, L. A. Bendersky, S.E. Lofland, M. Wuttig, I.Takeuchi, *Nature Comm.,* 2, (2011) 1529

CHAPTER 7

CONCLUSION AND SCOPE FOR FUTURE WORK

There was a time when magnetism and magnetic materials were synonymous with transition metal elements like Iron, Cobalt and Nickel. All useful applications emanating out of magnetism were based on this class of ferromagnetic materials. It was believed that crystallinity was an essential criterion for exhibition of useful magnetism meant for applications. Though ferrites existed in nature in the form of magnetite and maghemite, the successful synthesis of these materials in the laboratory with different cations slowly shifted the focus on to these classes of ferrimagnetic materials and their derivatives. Ferrites were an attractive proposition for inexpensiveness and found innumerable applications in the form of transformer cores, magnetic recording media, storage devices, microwave devices and microwave isolators. However the myth that crystallinity is an essential criterion for ferromagnetism exploded with the discovery of magnetic amorphous alloys in the early 1960's. This genre of materials became available in the form of ribbons under various trade names like FINEMET^{TM}, NANOPERM^{TM} and METGLAS^{TM}. Thus amorphous magnetic alloys slowly found their way in to the multibillion market of transformer cores, recording heads, shielding elements and sensors. However the underlying physics was not well developed and it took a while to establish and correlate various magnetic properties of these alloys with grain size, microstructure and morphology. The exchange correlation length is related to the grain size and hence tailoring magnetic properties necessarily aims at tailoring grain size. Various theories was also invoked/ proposed to correlate their properties. In this context, Herzer model, modified Herzer model and Stoner- Wohlfarth model deserve special mention.

With the advent of nanoscience and nanotechnology, controlling grain size and tailoring grain sizes to tailor exchange correlation length assumed importance. Inducing nanocrystallisation, in an otherwise amorphous material, became a hot topic of research. Thin film forms of these alloys also became important from an application perceptive for magnetic MEMS. Fabrication of films on to conventional substrates like silicon and glass also gained momentum.

There are various ways to induce nanocrystallisation. One such method is to go for thermal annealing and yet another alternative is to use techniques like swift heavy ion (SHI) irradiation. In SHI irradiation, depending on the energy and fluence, they can induce crystallisation and can tailor grains. In short, films are to be prepared using inexpensive techniques like vacuum evaporation on to silicon substrates using available targets. Metallic glasses based on CoFeNiSiB and FeNiMoB were immediately available as targets in the form of melt-spun ribbons. One of the major drawbacks of employing techniques like vacuum evaporation is the difficulty in retaining the parent composition of the target in the film as well. This is a challenge as well an opportunity. It is well known that magnetism in these types of alloys is predominantly decided by the presence of a Co-Fe rich phase along with a non-magnetic matrix formed by the glass former elements like Si, B and Mo. It is an opportunity because formation of Co-Fe structures devoid of B or Mo offers a new platform for tailoring the magnetic properties by thermal annealing and other techniques like SHI.

The first phase of this investigation was thus on the fabrication of thin film structures of Co-Fe by inexpensive techniques like vacuum evaporation using

$Co_{75}Fe_{14}Ni_4Si_5B_2$ (METGLAS 2714A) ribbons. Thermal annealing induced surface modification to tailor magnetic properties was one of the motives of this study. SHI irradiation is a versatile technique which can also induce morphological/ microstructural changes which in turn induce magnetic transformations. This was another motivation of the present study.

Magnetoelectric materials are nowadays hotly pursued and composites consisting of different combinations of ferroelectric and ferromagnetic materials are tried. It was thought that low coercivity films like Co-Fe could be a good ferromagnetic component in a multilayer structure of $BaTiO_3$-CoFe- $BaTiO_3$ (BTO-CoFe-BTO). The ME coupling usually dictates the usefulness of such structures and measurement of ME coupling was another task of this investigation. This is phase II of the present investigation. Two different structures based on BTO-CoFe-BTO and another on $SrTiO_3$-CoFe- $SrTiO_3$ (STO-CoFe-STO) was fabricated. ME coupling and related properties were measured along with a detailed study to elucidate the mechanism of giant ME coupling coefficient.

In a nutshell, these were the broad objectives of the present study. As in any investigation there are positives as well as negatives. This chapter looks at the brighter side of this study and also will shed light on the darker side. Few suggestions as well as some initial experiments conducted will also be presented as a proof of the concept for extending this investigation.

From the Slater-Pauling curve it is evident that alloys of Co-Fe exhibit high magnetic moments and hence suitable for applications like soft under layers in

perpendicular recording media and also for magneto electro mechanical sensor applications. Amorphous alloy thin films of Co-Fe were prepared from a composite target having a composition of $Co_{75}Fe_{14}Ni_4Si_5B_2$ by employing thermal evaporation under a high vacuum of $\approx 10^{-6}$Torr. As prepared thin film samples were annealed at various temperatures ranging from 373- 673K based on the crystallisation studies on the target material to check for microstructure modification. Annealing temperatures were pre-determined based on the thermal analysis of ribbon samples by using differential thermal analysis (DTA). Post-annealing of these films resulted in nanocrystallites of CoFe in a residual amorphous matrix. The glancing angle X-ray diffraction (GAXRD) and transmission electron microscopy (TEM) investigations on the annealed films indicated that the onset of nanocrystallization of CoFe is at around 373 K. GAXRD of the films annealed at 573K and 673K showed signatures of crystalline bcc Co-Fe (110) phases. High resolution transmission electron microscopy (HRTEM) studies substantiated this finding. Atomic force microscopic (AFM) images reveal surface smoothening with thermal annealing. On annealing, crystallization together with surface smoothening influences the magnetization reversal. The magnetic softness of the films greatly enhanced with thermal annealing. It was found that thermal annealing at 573K produced superlative films with appropriate magnetic characteristics. The magnetization reversal observed in these films was attributed to the coherent rotation with contribution from the demagnetizing field. Further increase in annealing temperature resulted in the magnetization reversal guided by a nucleation event followed by domain wall motion which in turn resulted in low coercivity.

A systematic experiment involving higher annealing temperatures would have been an ideal proposition for establishing the effects of grain size vis-a-vis the soft magnetic properties of these films. This could not be carried out because thermal annealing experiments were carried under vacuum in a glass dome. Though earlier investigations carried out on Fe-Ni could establish the validity of modified Herzer model on ultra thin films, such an inference could not be drawn out of this investigation on Co-Fe ultra thin films. This is one of the grey areas of this study. An appropriate model was not forthcoming based on this investigation. This is an area where more systematic experiments are to be conducted and the results are to be correlated.

It was known that impingement of swift heavy ions on targets modifies the material properties by depositing energy at high energies and high fluences. The deposition of energy is in the electronic energy loss regime leaving tracks, breaking bonds and formation of clusters on the target material. It was thought that irradiation of these samples with Ag ions could lead to nanocrystallisation or modification of the existing amorphous structures with latent tracks. This would modify magnetic properties.

Co-Fe thin films of thickness 44nm were subjected to SHI irradiation at various fluences of 1×10^{11}ions/cm^2, 1×10^{12}ions/cm^2, 1×10^{13}ions/cm^2 and 3×10^{13}ions/cm^2. It was found that the amorphous nature of the pristine film was preserved even after irradiation. The surface roughness decreased with increase in irradiation fluence. Power spectral density (PSD) analysis was employed to calculate the roughness exponent of pristine and irradiated samples. From PSD analysis it was

concluded that the mechanism behind the surface smoothening is viscous flow followed by evaporation-condensation. Ion irradiation results in stress relaxation in the films, which in turn reduces the coercivity at low fluences. At a higher fluence of 3×10^{13} ions/cm^2, the density of pinning centers increased which manifested in the form of increased coercivity. The high point of this experiment is that magnetic domains could be created in these films at a fluence of $1x10^{11}$ions/cm^2. However the disappearance of these domains at higher fluences is intriguing and warrants further investigation.

Multiferroic orders are easily achievable in composite structures and it is with this motive a multi-component structure consisting of BTO-CoFe-BTO was fabricated. The stress was on utilizing simple and inexpensive techniques like sol-gel process, spin coating and vacuum evaporation. A multilayer structure of BTO-CoFe-BTO was fabricated for evaluating the magnetoelectric coupling and also for determining the resonance frequencies both under dc and ac fields. Giant magnetoelectric coupling coefficients (MECC) values were obtained for the multilayer structure along with appropriate ferroelectric and soft ferromagnetic properties. The giant ME coupling obtained was explained on the basis of high magnetostriction of the middle Co-Fe layer. The large surface to volume ratio of ferromagnetic to and ferroelectric layers contributes to the giant MECC value. These experiments can be further extended for the fabrication of magneto-electric cantilevers for applications in the microelectronics/ MEMS industry. They can be mass produced and tested as magMEMS for energy harvesting applications or for sensing.

$SrTiO_3$ (STO) is a cousin of $BaTiO_3$ and an incipient ferroelectric material. They are widely used in FERAMs and hence occupy an important portfolio under the class of ferroelectric materials. In the unstressed form STO is paraelectric at room temperature. However, it can be transformed to ferroelectric by adding impurities or by strain engineering. A STO-CoFe-STO multilayer was fabricated using a similar experimental technique that was employed to fabricate BTO-CoFe-BTO structures. This configuration was chosen to investigate the effect of strain on the induced ferroelectric properties on STO and its effect on the MECC. The employment of $Co_{77}Fe_{23}$ composition with high magnetostriction values resulted in the achievement of a ME coupling of 20V/ (cm.Oe) at 753Hz. The high initial permeability of CoFe again resulted in a large ME coupling despite substrate clamping. The easy and cost effective synthesis techniques like sol-gel/spin coating and physical vapour deposition by thermal evaporation make these multilayers industrially favourable.

The evaluation of magnetostriction of these structures is of importance as far as applications are concerned. A systematic study on the effect of thickness of CoFe layers on the magnetostriction of these films is an attractive proposition. The magnetostriction of such structures can be estimated by Laser Doppler Vibrometry (LDV). With the expertise gained out of these investigations it was thought fit to extend these studies. Initial experiments were conducted as a proof of concept and the initial results are presented here. For this a bottom up approach was adopted for fabrication of multilayer structures. A schematic of the same is shown in figure 7.1.

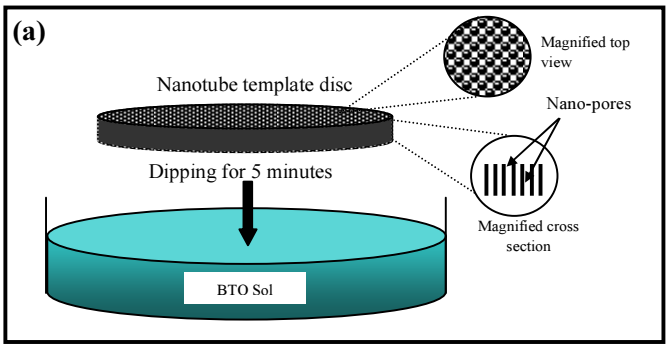

Fig. 7.1 (a) Template assisted growth process

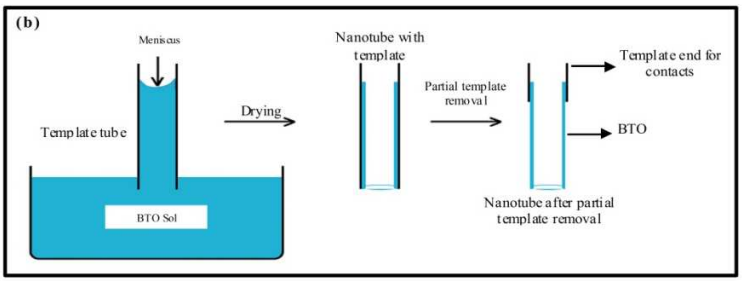

Fig. 7.1(b) Schematics of the Sol-gel capillary rise technique (bottom up process)

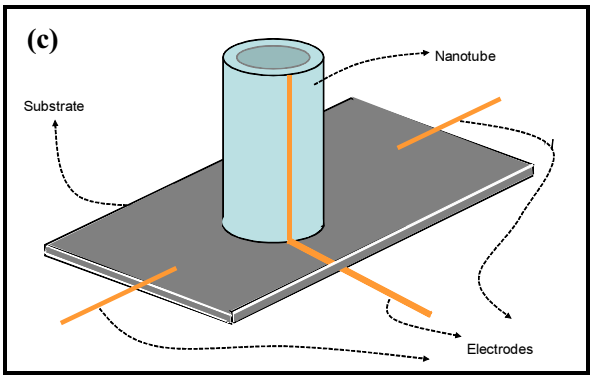

Fig. 7.1(c) Schematic of a magneto-electric cantilever that can be drawn out of this nanotube

It is to be noted here that a core shell structure was envisaged having a core of $BaTiO_3$ and a shell of magnetic material. Such a structure could be fabricated on templates of alumina or appropriate membranes or vice versa by appropriately depositing the required layer. Yet another geometry for such hybrid structures can be a vertical $BaTiO_3$ tube with CoFe on both ends. However, fabricating such hybrid nanostructures requires thorough optimization of process parameters and appropriate precursors.

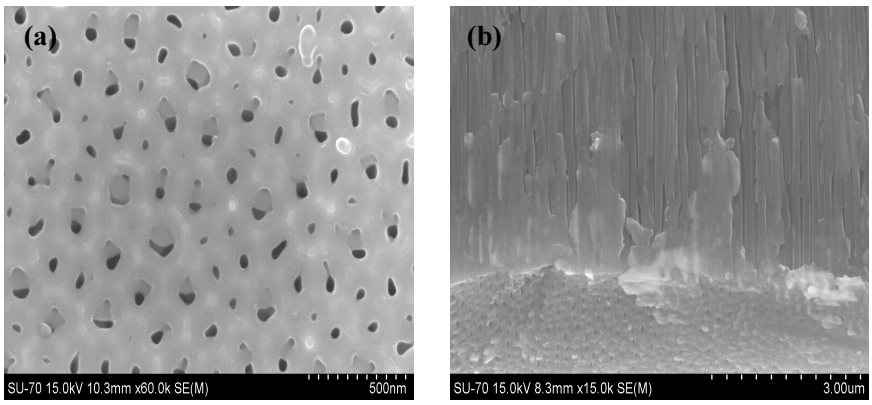

Fig. 7.2 SEM images of (a) alumina template and (b) BTO nanotubes formed

The scanning electron microscopic (SEM) images of the alumina template is shownin figure 7.2(a). BTO nanowires grown on the pores are shown in figure 7.2(b). A ferromagnetic layer of Ni or Co could be grown along with BTO wheremin BTO can be a nanotube and such hybrid structures are expected to produce enhanced ME coupling. Such an array of magneto-electric core shell nanotubes could also be used as the major active element in high density mass storage devices. As each single active element is of the order of a few nanometers, the possibility of fabrication of

several components like field sensors, transducers and switches in less than a micrometer square is promising and futuristic.

A series of magnetoelectric cantilevers can be fabricated by employing a multilayer structure of BTO-CoFe-BTO. The schematic is shown below (figure 7.3).

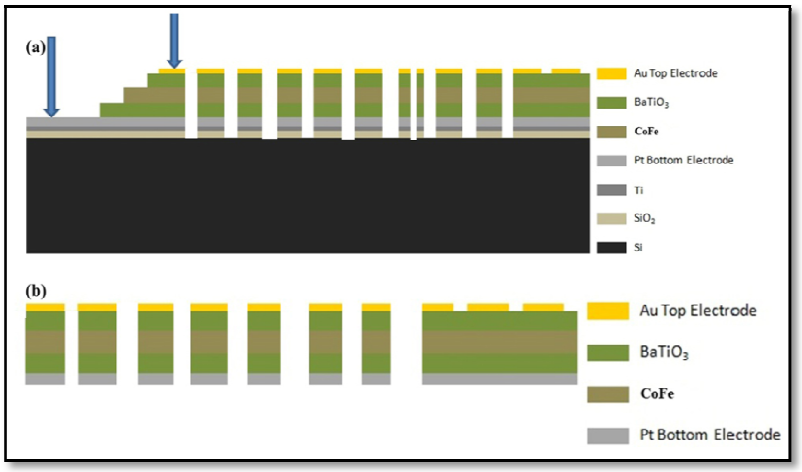

Fig. 7.3 Fabrication of magnetoelectric cantilevers and microwire sensors through micromachining (a) Dissolving the thin film and substrates to obtain desired size and shapes.(assisted by pre designed masks) (b) Complete dissolution of the substrate to release the micro/nano magneto electric arrays (heterogeneous)

The fabrication of such cantilevers on a silicon substrate is limited by the masks employed and is restricted to a few micrometers (~1micrometer). Here, a 5 step deposition is needed (lower contact electrode, BTO, CoFe, BTO, upper contact electrode) which is to be deposited over a pre fabricated mask with ordered channels or pores. As the voltage is developed across the sample, the top surface area can be limited to the point contact electrode size. For any high frequency applications, the voltage developed will be appreciably high so that no external amplifier is required.

An initial experiment was conducted based on the above geometry and the preliminary results are presented here. The initial voltage generated on a 500 micrometer wide microcantilever at an ac modulating field of 10 Oe, with a modulation frequency of 1kHz and a dc biasing magnetic field of 18 Oe for a total thickness of 225 nm was around 2.6mV. It is to be noted that the magnetic to piezoelectric volume was kept at around 1:2. A systematic study on various other configurations can be conducted later and is futuristic. Such devices can also be fabricated by adopting bottom up approaches on a silicon wafer with properly designed masks. An immediate application of such structure can be a switch which can be controlled by electric or magnetic fields. Such configurations can also serve as devices without the necessity of an external amplifier.

The motto of the European commission and many other international agencies "NO LEAD in microelectronics/MEMS" can be achieved soon by suitably employing other materials for applications. Employment of other piezoelectric systems (in place of BTO) with a higher longitudinal and transverse piezoelectric d_{31} and d_{33} coefficients (like BZT, BZT-BCT, KNN) will hopefully enhance this effect to another order thereby opening up a possibility of obtaining appreciable ME signal without any external amplifier which can in turn reduce the volume of the integrated devices like sensors and transducers, involving ME materials form the major active element.

Magnetism is always associated with a north pole and a south pole. The lines of forces are flux and they are supposed to be flowing from north to south. As long as

there is a magnetic material, there will be lines of forces and these lines of forces can be intercepted. A parallel can be drawn out of this phenomenon.

Knowledge is also like lines of forces and research is a provider of free knowledge. This knowledge resulting out of research are lines of forces and when they are intercepted, knowledge is assimilated. Assimilation alone does not mean anything. To put this in to practical use is the next logical step and this is innovation. Innovation is a major link in the knowledge economy and creation of wealth. Creation of wealth leads to enhancement of quality of life.

So this thesis is also an attempt in realizing these objectives. The phase I of this investigation is the generation of knowledge in the form of constructing simple models to arrive at the exact mechanism of soft magnetic materials based on Co-Fe. Phase II is the adaption of these knowledge base to demonstrate devices. This is innovation. Any research which does not look at the economy is folly. Hence this stduy also emphasized in developing cost effective techniques to fabricate model magMEMS. The demonstration of a working cantilever based magMEMS is a prelude in developing energy harvesters. This is futuristic and is bound to touch the lives of human beings. A day is not far away when magMEMS based devices could be used for antiterrorist activities. Thus the philosophy of this piece of work is also the philosophy of magnetism. Be attractive and useful !!!